Simulation, experiments, and modeling of cloud cavitation
with application to burst wave lithotripsy

Thesis by
Kazuki Maeda

In Partial Fulfillment of the Requirements for the
Degree of
Doctor of Philosophy

Caltech

CALIFORNIA INSTITUTE OF TECHNOLOGY
Pasadena, California

2018
Defended May 3, 2018

ACKNOWLEDGEMENTS

First and foremost, I truly thank my advisor Tim Colonius for his continuous support throughout the thesis project. I would not have completed this thesis not for his patience and trust in my work. I have learned from Tim not only computational fluid dynamics, but also various skills and techniques to run and manage scientific research projects, all of which are valuable in my continuing career. I thank John Brady, Guillaume Blanquart, and Michael Shapiro for serving as thesis committee members and providing valuable suggestions and comments on the thesis.

I acknowledge the members of the PPG research project for collaborations and for providing valuable suggestions on my work at the semi-annual project meetings and other occasions. I especially thank Adam Maxwell, Wayne Kreider, and Michael Bailey in the Applied Physics Laboratory at University of Washington for hosting my visits to conduct laboratory experiments.

I thank Daniel Fuster for hosting my visit to the Institut Jean Le Rond D'Alembert at Pierre and Marie Curie University.

I cannot thank too much the past and present fellow students of the computational flow physics group, including Vedran Coralic, Sebastian Liska, Jomela Meng, Aaron Towne, Chen Tsai, Jeesoon Choi, Andres Goza, Phillipe Tosi, Andre da Silva, Marcus Lee, Ke Yu, and Ethan Pickering for countless discussions. I acknowledge Jean-Christophe Veilleux and Mathis Bode for research collaborations. I also thank all other members of the group and the multiphase flow research meeting, including Gerry Della Rocca, Oliver Schmidt, Georgious Rigas, Gianmarco Mengaldo, Kevin Schmidtmier, and Erick Salcedo.

Finally, I truly thank my wife Nadia, our son Eugene and all our family members for their continuous support and encouragement.

I acknowledge the Funai Foundation for Information Technology, for the Overseas Scholarship. This work was supported by the National Institutes of Health under grants P01-DK043881. Many simulations presented in this thesis utilized the Extreme Science and Engineering Discovery Environment, which was supported by the National Science Foundation grant number CTS120005.

ABSTRACT

Modeling, numerical simulations, and experiments are used to investigate the dynamics of cavitation bubble clouds induced by strong ultrasound waves.

A major application of this work is burst wave lithotripsy (BWL), recently proposed method of lithotripsy that uses pulses (typically 10 wavelengths each) of high-intensity, focused ultrasound at a frequency of $O(100)$ kHz and an amplitude of $O(1)$ MPa to break kidney stones. BWL is an alternative to standard shockwave lithotripsy (SWL), which uses much higher amplitude shock waves delivered at a typically much lower rate. In both SWL and BWL, the tensile component of the pressure can nucleate cavitation bubbles in the human body. For SWL, cavitation is a significant mechanism in stone communition, but also causes tissue injury. By contrast, little is yet known about cavitation in BWL.

To investigate cloud cavitation in BWL, two numerical tools are developed: a model of ultrasound generation from a medical transducer, and a method of simulating clouds of cavitation bubbles in the focal region of the ultrasound. The numerical tools enable simulation of the cavitation growth and collapse of individual bubbles, their mutual interactions, and the resulting bubble-scattered acoustics. The numerics are implemented in a massively parallel framework to enable large-scale, three-dimensional simulations. Next, the numerical tools are applied to bubble clouds associated with BWL. Additionally, laboratory experiments are conducted *in vitro* in order to calibrate and validate the simulations. A major feature of the resulting bubble clouds is that the cloud size is similar to the ultrasound wavelength. This results in an anisotropic structure where the bubbles closest to the wave source grow to larger size and oscillate more rapidly. A new scaling parameter is introduced to characterize the nonlinear bubble cloud dynamics that generalizes the cloud interaction parameter of d'Agostino and Brennen (1989) defined for weak (linearized), bubble cloud dynamics excited uniformly by long-wavelength pressure waves. The mechanisms leading to the observed bubble dynamics are identified. The results further show that bubble clouds can scatter a large portion of incident ultrasound and consequently shield distal regions, including kidney stones, from irradiation. This energy shielding is quantified, and the simulations show that even a thin layer of bubbles can scatter up to 90% of the incident wave energy. A strong correlation is identified between the magnitude of energy shielding and the amplitude of the bubble-scattered acoustics. The correlation may be of use to control cavitation in

the human body in real time by ultrasound monitoring for better outcomes of BWL.

PUBLISHED CONTENT AND CONTRIBUTIONS

Maeda, K. and T. Colonius. “Bubble cloud dynamics in an ultrasound field”. In: *arXiv:1805.00129*.
K.M conducted simulation and experiment, prepared the data, and wrote the manuscript.

Maeda, K., A.D. Maxwell, W. Kreider, T. Colonius, and M.R. Bailey. “Quantification of the energy shielding of kidney stones by cavitation bubble clouds during Burst Wave Lithotripsy”. In: *In preparation*.
K.M conducted modeling, simulation, and experiment, prepared the data, and wrote the manuscript.

Bode, M., S. Satcunanathan, K. Maeda, T. Colonius, and H. Pitsch (2018). “An equation-of-state tabulation approach for injectors with non-condensable gases: Development and analysis”. In: *The 10th International Symposium on Cavitation (CAV2018)*.
K.M conceptualized the numerical model and helped prepare the manuscript.

Maeda, K. and T. Colonius (2018a). “Eulerian-Lagrangian method for simulation of cloud cavitation”. In: *Journal of Computational Physics*. DOI: `http://doi.org/10.1016/j.jcp.2018.05.029`.
K.M conducted modeling, simulation and experiment, prepared the data, and wrote the manuscript.

– (2018b). “Numerical simulation of the bubble cloud dynamics in an ultrasound field”. In: *The 10th International Symposium on Cavitation (CAV2018)*.
K.M conducted simulation, prepared the data, and wrote the manuscript.

Maeda, K., Kreider, A.D. W. Maxwell, T. Colonius, and M.R. Bailey (2018). “Combined numerical and experimental analysis of cloud cavitation for burst wave lithotripsy”. In: *The ASME 5th Joint US-European Fluids Engineering Summer Conference (FEDSM2018)*.
K.M conducted modeling, simulation, and experiment, prepared the data, and wrote the manuscript.

Maeda, K., A.D. Maxwell, W. Kreider, T. Colonius, and M.R. Bailey (2018). “Investigation of the energy shielding of kidney stones by cavitation bubble clouds during burst wave lithotripsy”. In: *The 10th International Symposium on Cavitation (CAV2018)*.
K.M conducted modeling, simulation, and experiment, prepared the data, and wrote the manuscript.

Pishchalnikov, Y.A, W. Behnke-Parks, M. Mellema, M. Hopcroft, A. Luong, D. Laser, K. Morrison, T. Colonius, and K. Maeda (2018). “Urinary stone erosion and fragmentation under low-intensity quasi-collimated ultrasound using gas-filled microbubbles with stone-targeting lipid shells”. In: *Journal of the Acoustical*

Society of America. Vol. 143. 3. ASA, pp. 1861–1861. doi: `https://doi.org/10.1121/1.5036106`.
K.M conducted numerical simulation.

Veilleux, J-C., K. Maeda, T. Colonius, and J.E. Shephered (2018). "Transient cavitation in pre-filled syringes during autoinjector actuation". In: *The 10th International Symposium on Cavitation (CAV2018)*.
K.M provided the numerical setup and helped preparing the manuscript.

Maeda, K. and T. Colonius (2017). "A Source Term Approach for Generation of One-way Acoustic Waves in the Euler and Navier-Stokes equations". In: *Wave Motion* 75, pp. 36–49. doi: `http://doi.org/10.1016/j.wavemoti.2017.08.004`.
K.M conducted modeling and simulation, prepared the data, and wrote the manuscript.

Maeda, K., T. Colonius, W. Kreider, A. D. Maxwell, and M. Bailey (2017). "Quantification of the shielding of kidney stones by bubble clouds during burst wave lithotripsy". In: *Journal of the Acoustical Society of America*. Vol. 141. 5. ASA, pp. 3673–3673. doi: `http://doi.org/10.1121/1.4987968`.
K.M conducted modeling, simulation and experiment, prepared the data, and wrote the manuscript.

Maeda, K., T. Colonius, W. Kreider, A. Maxwell, and M. Bailey (2016). "Modeling and experimental analysis of acoustic cavitation bubble clouds for burst-wave lithotripsy". In: *Journal of the Acoustical Society of America*. Vol. 140, pp. 3307–3307. doi: `http://doi.org/10.1121/1.4970532`.
K.M conducted modeling, simulation, and experiment, prepared the data, and wrote the manuscript.

Maeda, K., W. Kreider, A. Maxwell, B. Cunitz, T. Colonius, and M. Bailey (2015). "Modeling and experimental analysis of acoustic cavitation bubbles for Burst Wave Lithotripsy". In: *Journal of Physics: Conference Series* 656.1, p. 012027. doi: `http://doi.org/10.1088/1742-6596/656/1/012027`.
K.M conducted modeling, simulation, and experiment, prepared the data, and wrote the manuscript.

TABLE OF CONTENTS

LIST OF ILLUSTRATIONS

LIST OF TABLES

NOMENCLATURE

BWL. Burst Wave Lithotripsy.

CFD. Computational Fluid Dynamics.

DNS. Direct Numerical Simulation.

ESWL. Extracorporeal ShockWave Lithotripsy.

FV-WENO. Finite Volume Weighted Essentially Non-Oscillatory Scheme.

HIFU. High Intensity Focused Ultrasound.

KZK. Khokhlov-Zabolotskaya-Kuznetsov Equation.

LES. Large Eddy Simulation.

ODE. Ordinary Differential Equation.

PDE. Partial Differential Equation.

PDF. Probability Density Function.

Chapter 1

INTRODUCTION

1.1 Cloud cavitation in lithotripsy - historical perspective

When tensile stress is applied to a liquid and the local pressure falls below the vapor pressure, clouds of bubbles are nucleated and rapidly collapse on recovery of the pressure. This phenomenon is denoted as cavitation, or cloud cavitation, and is of critical importance in various applications. Cloud cavitation occurs mainly in two scenarios: decrease in the hydrodynamic pressure in a liquid flow, typically on the surface of an immersed body, and propagation of tensile components of a pressure wave including acoustic and shockwaves. The two regimes of cavitation are heuristically distinguished as inertial (hydrodynamic)- and acoustic cavitation.

The study of cloud cavitation finds its roots in industrial needs of understanding the physical process of inertial cavitation for better designing hydraulic machines (Plesset and Ellis, 1955; Acosta, 1958; Kato, 1975). Inertial cavitation has a critical impact on the performance of hydrofoils, ship propellers, turbo-machineries and pumps: continuous cavitation on a hydrofoil/propeller largely complicates the surrounding flow structures to affect the drag and lift forces/thrust; violent collapse of caviation bubble clouds results in material damage (cavitation erosion) and noise emission. A vast amount of literatures has addressed cavitation in this context since early 20th century to date (Knapp, 1954; Brennen, 2013).

Acoustic cavitation has gained great interest in the last three decades for improved outcomes of ultrasound medical therapies. The therapies aim to noninvasively ablate a target by causing mechanical stress and/or thermal coagulations by pulses of high-intensity focused ultrasound (HIFU) or shockwaves that are delivered from outside the body. During the passage of tensile components of pulses, cavitation bubbles can be formed in the human body. This cloud cavitation is especially critical for outcomes of the treatment of extra-corporeal shockwave lithotripsy (ESWL), a method of lithotripsy currently used in clinics. Typical ESWL aims to mechanically comminute kidney stones by causing spallation with normal and/or shear stress (Lokhandwalla and Sturtevant, 2000; Cleveland and Sapozhnikov, 2005). The mechanical stress is induced by propagation of focused pulses of shockwaves with a peak positive amplitude of $O(10 - 100)$ MPa, followed by a long tensile tail with

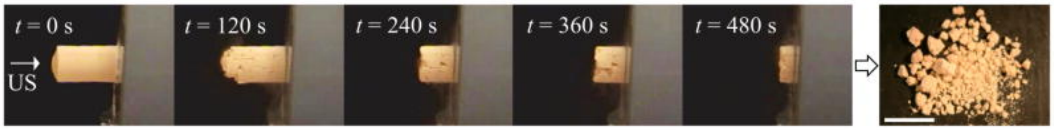

Figure 1.1: Fragmentation of a model stone during BWL *in vitro*. The scale bar denotes 1 cm. Reprinted from Maxwell et al. (2015) with the permission of Elsevier. © 2015 by Elsevier.

a negative amplitude of $O(1-10)$ MPa. Meanwhile, in the actual treatment, due to the high amplitude of the negative pressure, bubble clusters are nucleated in the tensile tail and then violently collapse in the human body. The collapse of the bubble clusters on/near kidney stones can enhance stone comminution by erosion, while those occurring in the surrounding tissues result in severe injuries (Coleman et al., 1987; Pishchalnikov et al., 2003; McAteer et al., 2005; Bailey et al., 2006). Precise control of the nucleation sites of bubble-clusters has remained a challenge and the injury is thought to be unavoidable, and this has been seen as a major disadvantage of ESWL.

1.2 Burst wave lithtoripsy

Burst wave lithotripsy (BWL) has been recently proposed as a noninvasive alternative to ESWL (Maxwell et al., 2015; Thoma, 2014). BWL is a HIFU-based lithotripsy that uses a sinusoidal form of a focused pressure wave, burst wave, with a peak maximum amplitude of $O(1-10)$ MPa and a frequency of $O(100)$ kHz for kidney stone comminution. Figure 1.1 shows fragmentation of a model stone using BWL *in vitro*. It has been empirically found that, compared to SWL, BWL can comminute stones into smaller fragments. Figure 1.2 shows comparisons of the representative focal waveforms of ESWL and BWL. Due to the lower peak pressure than SWL, BWL expects less violent cavitation collapse and thus lower risk of potential injury. The demonstration of stone comminution was made *in vitro* in highly degassed water with approximately 20% O_2 saturation, such that cavitation was not observed. Later in water with 65% O_2 saturation, however, $O(1)$ mm size of cavitation bubble clouds are identified around the focal region without stone model during a passage of the burst wave with a frequency of 335 kHz and a peak maximum amplitude of 6 MPa (Maeda, Kreider, et al., 2015).

Figure 1.3 shows a representative bubble cloud excited in BWL. The dynamics of cloud cavitation excited by this particular regime of ultrasound has not been well explored and their potential effects on BWL are unknown, despite their critical

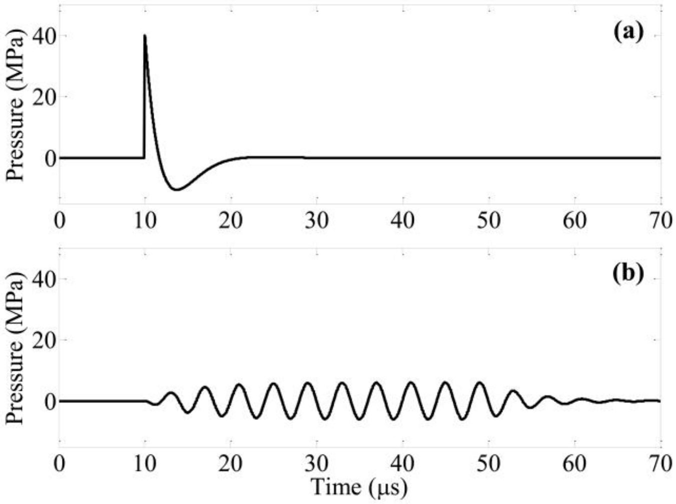

Figure 1.2: Comparison of representative focal waveforms of (a)SWL and (b)BWL. Reprinted from Maxwell et al. (2015) with the permission of Elsevier. © 2015 by Elsevier.

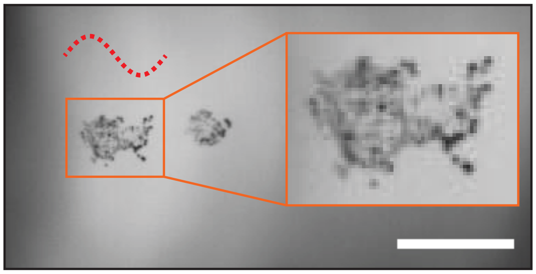

Figure 1.3: Cavitation bubble cloud observed in an experimental high-speed imaging during a passage of focused ultrasound in water. The dotted line indicates the wavelength of the burst wave. The scale bar denotes 5 mm.

importance on the safety and efficacy for clinical applications.

1.3 Method of modeling the dynamics of cloud cavitation

Although experiment provides critical insights into cloud cavitation phenomena, precise measurement of individual bubbles has been a challenging task due to the fast dynamics of bubble oscillations at the small spatial scale. Modeling and numerical simulations have been therefore central tools for quantification of the dynamics.

The basis of the modeling the bubble dynamics dates back to Rayleigh (1917), who formulated the collapse of a spherical, isolated gas bubble in the inviscid incompressible potential flow of an unbounded liquid. He obtained an ordinary differential equation (ODE) in terms of the radius and the radial velocity of the bubble. Plesset (1949) generalized the Rayleigh's equation to model cavitation growth of a bubble by considering fluctuations in the far-field pressure of the liquid. The generalized equation is denoted as the Rayleigh-Plesset equation and has been extended to many forms to include the effects of damping mechanisms of liquid viscosity, acoustic radiation, and heat and mass transfer (Gilmore, 1952; Plesset and Prosperetti, 1977; Keller and Miksis, 1980; Preston et al., 2007; Bergamasco and Fuster, 2017), non-spherical deformation, viscoelasticity of surrounding liquid (Church, 1995; Freund, 2008; Gaudron et al., 2015), to name but a few. The equation predicts the complex, nonlinear response of bubble oscillations under harmonic far-field pressure excitation with a large amplitude, including bifurcation and chaos, and resulting acoustic emission rich in harmonics (Lauterborn and Cramer, 1981; Prosperetti et al., 1988; Brenner et al., 2002).

A major difficulty in modeling cloud cavitation stems from multiple length-scales of the problem, ranging from the size of a bubble, inter-bubble distance, and the size of a bubble cloud, to the pressure wavelength. Existing methods of modeling can be categorized into two major approaches, both of which impose certain assumptions on separations of the scales: (1) tracking the dynamics of individual bubbles under mutual-interactions, which we denote as Lagrangian point-bubble approach[1] and (2) considering the dynamics of macroscopic bubbly-mixture then modeling the averaged effect of the bubble dynamics at the small scales on the mixture without tracking individual bubbles, which we denote as the mixture-averaging approach.

In the Lagrangian point-bubble approach, the Rayleigh-Plesset equation (or one of its many generalizations) is extended to a system of multiple bubbles by formulating the potential flow induced by each bubble as a monopole (or poles represented by certain set of harmonic functions that defines the bubble-shape when non-spherical deformation is considered), and expressing their interactions using a multi-pole expansion (Takahira et al., 1994; Doinikov, 2004; Ilinskii et al., 2007). The dynamical equation becomes a non-autonomous, implicit, linear system of ODEs in terms of the radius and radial velocity of each bubble. The typical modeling assumption made here is that the liquid is incompressible at a scale of bubble cloud; the characteristic wavelength of the pressure field is much larger than the size of the cloud. The solution of an N-body problem limits to a relatively small number of bubbles

---

[1] *Lagrangian point-particle approach* generally covers wide variety of numerical methods for simulation of dispersed multi-phase flows (Balachandar and Eaton, 2010). Such other methods are distinguished from the particular approach for the system of dispersed bubbles addressed in this thesis.

(Chahine and H. Liu, 1985; Bremond et al., 2006; Zeravcic et al., 2011).

The mixture-averaging approach was pioneered by vanWijngaarden (L. vanWijngaarden, 1966; L vanWijngaarden, 1968). In the approach, bubbly-liquid is modeled as a continuous mixture. The volume of dispersed bubbles is converted to a continuous void fraction field in a control volume that contains a sufficiently large number of bubbles. Here, critical modeling assumption is that the length-scale of the control volume (averaging length-scale) is larger than the characteristic inter-bubble distance. The dynamics of the mixture are formulated as conservation equations about the volume-averaged mass, momentum and energy of the mixture as partial differential equations (PDEs), and they are denoted as volume-averaged equations. The volumetric change in the gas-phase is closed by considering the averaged contributions of the oscillations of bubbles in response to pressure fluctuations in the mixture. Bubbles are typically modeled as spherical cavities, of which dynamics are described by the Rayleigh-Plesset-type of equation. The radius and coordinate of the bubbles are treated as statistically averaged quantities in the field of mixture, rather than deterministic variables defined at each single bubble. Inter-bubble interactions can be modeled by an effective pressure in the mixture that forces the oscillations of bubbles, enabling the methods to avoid explicitly solving for the interactions. Caflisch et al. (1985) later showed that the volume-averaged equations formulated by vanWijngaarden can be derived by an adaptation of an ensemble-averaged equation for multiple-scattering of waves in a random media introduced by Foldy (1945). The family of volume- and ensemble-averaged equations is generally denoted as mixture-averaged equations, and has been applied to great many problems including acoustic/shock propagation in bubbly liquid and other regimes of bubbly flows.

A critical challenge in modeling the dynamics of cloud cavitation in HIFU is the absence of scale separation assumed in the aforementioned approaches. High-frequency ultrasound can have a small wavelength close to the size of the bubble cloud, thus the assumption of liquid incompressibility made in the Lagrangian point-bubble approach may be invalid. A large amplitude of the pressure excitation results in nonlinear bubble oscillations with a large amplitude. The bubble-scattered pressure waves may have structures as fine as the characteristic inter-bubble distance, and an appropriate averaging length-scale may not exist within that a sufficiently large number of bubbles are present, thus validity of the mixture-averaging approach becomes ambiguous. The dynamics of cavitation bubbles in such a regime cannot

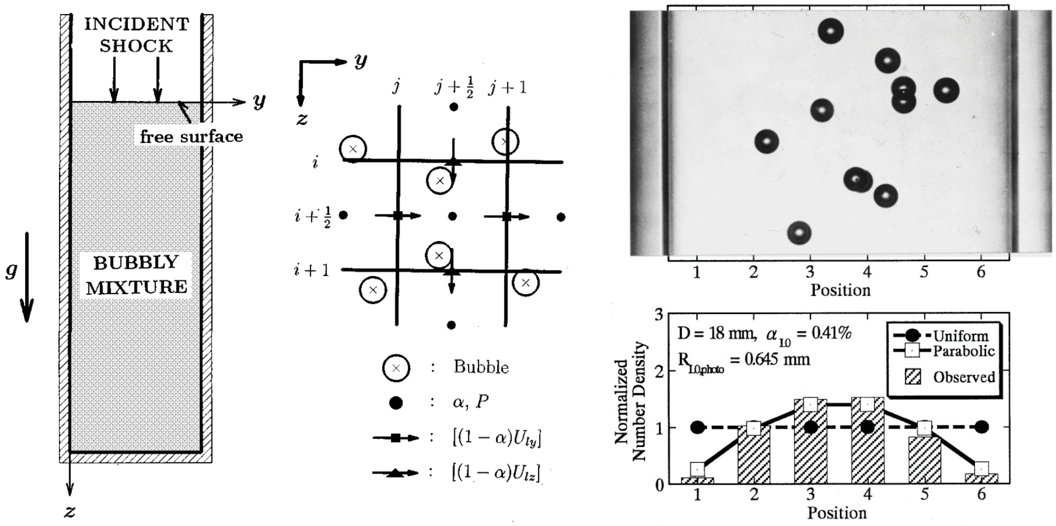

(a) (b)

Figure 1.4: Schematic of an Eulerian-Lagrangian method employed by Kameda and Matsumoto (1996). Reprinted from Kameda and Matsumoto (1996) with the permission of AIP Publishing. © 1996 by AIP Publishing.

be modeled by existing methods of simulation with reasonable accuracy, and the effects of cloud cavitation in HIFU have thus been elusive.

1.4 Numerical approaches

Eulerian-Lagrangian method

With the growth in computational power, various numerical methods have been developed to solve the mixture-averaged equations at fine spatial scales. An Eulerian-Lagrangian method has been explored as one of such methods.

The method was employed by Kameda and Matsumoto (1996) in the context of simulating the shock-propagation in a bubbly-mixture with a relatively small number of bubbles in a cylindrical pipe (figure 1.4 (a)). In the method, the mixture-averaged equation is discretized on a two-dimensional computational grid defined on an Eulerian frame of reference, while the dynamics of individual bubbles are explicitly tracked as Lagrangian points unlike the classical mixture-averaging approach. The volume of bubbles is converted onto the void fraction field on the grid. The pressure at the coordinate of each bubble is interpolated from the pressure of the mixture defined on the grid and used to force the bubble oscillations in the Rayleigh-Plesset equation. The purpose of using the Eulerian-Lagrangian method was that the method is capable of accounting for the effect of non-uniform spatial distribution of bubbles on the shock propagation as well as mimicking the experimental condition of bubbles in simulation, shown in figure 1.4 (b), such that direct comparisons can be made. Those were not possible with one-dimensional classical mixture-averaging approaches that assume statistical, spatial homogeneity of the bubble distribution in the span-wise (pipe-normal) direction. The capabilities of the method are also beneficial for combined numerical and experimental analysis of cloud cavitation as demonstrated in Chapter 4 and 5.

Subgrid modeling

An important property of numerical methods of CFD is grid convergence of solutions, meaning that numerical solutions converge to analytical solutions, if they exist, with a refinement of temporal and spatial discretization. This property is, for instance, important for Large-Eddy-Simulation (LES); the solution of LES with proper sub-grid modeling of turbulent eddies predicts the correct turbulent statistics without explicitly resolving the eddies, while it recovers the solution of direct numerical simulation (DNS) with grid refinement (Leonard, 1975; Meneveau and Katz, 2000).

Fuster and Colonius (2011) attempted to develop an Eulerian-Lagrangian method for modeling bubble clusters that allows grid convergence, in that the model recovers the analytical solution of the Keller-Miksis equation, a variation of the Rayleigh-Plesset equation, for a single bubble with grid refinement. This was done by modeling the pressure field at a sub-grid scale within computational cells that contain bubbles. The pressure field around a oscillating bubble is a superposition of the far-field pressure generated by an external source, that forces the bubble oscillations, and the pressure field induced by the bubble. The bubble-induced pressure field radially decays with distance from the bubble surface and thus tends to become negligible in the far-field, while it is significant in the near field. When the size of grid becomes close to the size of the bubble, the pressure of the cell (cell-averaged pressure) deviates from the true component of the far-field pressure that forces the bubble oscillations due to the contribution of the bubble-induced pressure. Therefore, using the pressure of the cell to force the bubble oscillations results in incorrect simulations of the bubble dynamics. A sub-grid model corrects this error by properly modeling the far-field component of the pressure that forces the bubble oscillations to recover the solution of the Keller-Miksis equation. The bubble-induced pressure field can be also modeled as an acoustic wave propagating outward and resolved on the surrounding grids. Fuster and Colonius (2011) focused on validating the sub-grid modeling using idealized, two-dimensional problems of bubble clouds excited by a weak pressure wave. The numerical scheme used to integrate the Eulerian field (background flow solver) is non-dissipative and is restricted to a linear pressure wave that could not support pressure waves with a strong amplitude in a practical range of cloud cavitation considered in BWL. Nevertheless, the Eulerian-Lagrangian method can be potentially extended for three-dimensional problems and generalized to support strong pressure waves by combining with an appropriate background flow solver that can support strong, nonlinear pressure waves. Such extension and generalization of the method may enable accurate computation of cloud cavitation in HIFU.

Finite volume WENO scheme

A shock- and interface-capturing method is popularly used to simulate the dynamics of compressible fluid with discontinuities such as shockwave and material interfaces on an Eulerian grid. In the method, the discontinuity is treated as a continuous but large gradient in the flow variables. By doing so, the (region of) discontinuity is advected on a grid, and thus effectively captured, without being explicitly tracked. Meanwhile, such simulations tend to suffer from the following drawbacks: loss of accuracy due to smearing of the interface region, resulting from numerical diffusion; numerical instabilities due to the high pressure and density gradient in the interface-region. Finite Volume Weighted Essentially Non-Oscillatory (FV-WENO) scheme is a numerical scheme to spatially integrate the flow field on a grid. By introducing an optimal dissipation near discontinuities, the scheme is able to achieve high-order accuracy of solution, thus low dissipation, in smooth region, while avoid oscillations at the discontinuities (X.-D. Liu et al., 1994; Johnsen and Colonius, 2006; Coralic and Colonius, 2014; Shu, 2016). The scheme has been applied to simulation of various challenging problems with shocks and interfaces (Tanguay, 2004; Johnsen and Colonius, 2009; Coralic and Colonius, 2013; Meng and Colonius, 2018). Owing to its robustness, high-order accuracy and reasonable spectral properties, variations of FV-WENO (or in some cases finite-difference WENO) have also been applied to simulate complex, multi-scale problems of compressible flows, including shock- boundary layer interaction and shock-turbulence interaction (Pirozzoli, 2002; Hill and Pullin, 2004; Lele and Larsson, 2009; Johnsen, Larsson, et al., 2010). Considering these performances, FV-WENO can be potentially used as a background flow solver to resolve incident ultrasound waves and strong bubble-induced pressure waves in simulation of cloud cavitation, combined with the strategy of sub-grid modeling. This is the focus of Chapter 3.

1.5 Motivation and objectives

The motivation for the present thesis is the realization that the state-of-the-art techniques of CFD may further advance the existing framework of modeling the bubble cloud dynamics, and combined numerical and experimental analysis using the advanced model may provide detailed insights into the dynamics of cavitation bubble clouds in an ultrasound field and enable quantification of the potential effects of cavitation on outcomes of BWL.

The overall objective of the present thesis is three-fold. The first is to develop numerical tools for simulation of cloud cavitation in intense ultrasound fields. The second is to use the tools to investigate and gain the knowledge on the bubble cloud dynamics for understanding the dynamics of bubble clouds in combination with laboratory experiment. The third is to apply the numerical tools and the knowledge to quantify the effects of cavitation on the outcomes of BWL.

To enable direct comparisons of numerical simulation and experiment, numerical models and methods are designed to mimic the physical process of experimental setups as explicitly as possible (i.e., modeling and visualizing individual bubbles). For problems that require a prohibitively large amount of computational resource, model reduction techniques are carefully introduced to reduce the cost of computations. This is to maximize the amount of information extracted from a given resource, compromising between increase in the total number of simulation runs and loss of accuracy due to the model reduction. For simulations of cloud cavitation, the population and the size distribution of pre-existing bubble nuclei are not known a-priori. For the best quality of engineering prediction, experiments were used not only to validate the numerical methods, but also to provide an approximate range of initial conditions of bubble nuclei as an input parameter of numerical simulations.

It should be stated that, the present thesis focuses on cloud cavitation in water in the laboratory *in vitro*. The actual clinical treatment of BWL will involve complex dynamics of ultarsound propagation through the human body and their interactions with various shapes and compositions of kidney stones. Modeling such effects is, however, beyond the focus of the present objectives of quantifying the effects of cloud cavitation on the prototype-BWL. The philosophy of this thesis is that the numerical tools developed for idealized problems can be used as building blocks to study more complex problems, and that analysis of the idealized problems may help and motivate designing future experiments and simulations that model the environments *in vivo*.

1.6 Summary of contributions

In this section the contributions of the thesis that meet the objectives are summarized.

- A mathematical model of an acoustic source is developed that can generate uni-directional (one-way) pressure waves from an arbitrary surface immersed in a three-dimensional computational domain. The model is implemented in the Euler equation. FV-WENO is used to simulate generation of focused ultrasound by piezo-ceramic medial transducers. Results were validated by comparing with experimental measurements (Chapter 2).
- A numerical method is developed for simulation of cloud cavitation excited by a strong ultrasound wave. It is an Eulerian-Lagrangian method with a subgrid model and a FV-WENO scheme, and implemented in a massively parallel framework for simulations of three-dimensional problems. Reduced models are introduced for simulation of bubble clouds that possess translational or axi-symmetry. The reduced model averages the Eulerian field in the direction of symmetry to reduce the total number of grid cells from $O(N^3)$ to $O(N^2)$, where N is the number of grid per dimension. The missing component of the pressure in the direction of symmetry is modeled as a stochastic noise at a subgrid scale. The method is verified using problems of acoustic cavitation of a single bubble, bubble screen, and a bubble cloud. An anisotropic structure is newly identified in the bubble cloud during the passage of a focused ultrasound wave, in that proximal bubbles grow to larger radius than the distal bubbles. (Chapter 3).
- In order to elucidate the anisotropic structure and underlying physics, the dynamics of bubble clouds in intense ultrasound fields are further investigated through experimental high-speed imaging and numerical simulations. Volumetric evolutions of bubble cloud obtained in the simulation agree with the high-speed images. A scaling parameter, namely dynamic cloud interaction parameter, is introduced to characterize the nonlinear bubble cloud dynamics that generalizes the cloud interaction parameter introduced by d'Agostino and Brennen (1989) for linearized bubble cloud dynamics. It is found that the proposed parameter scales the energy localization in the cloud; the kinetic

energy of liquid induced by bubbles becomes larger in the proximal side of the cloud than in the distal side, with the increase of the parameter. Under pressure excitation with a high amplitude, the proximal, energetic bubbles can be locally cavitated, and this results in the anisotropic structure. Moreover, it is shown that the amplitude of the far-field, bubble-scattered acoustics is likewise scaled by the proposed parameter, and thus is correlated with the energy-localization in the cloud. The numerical results indicated that bubble clouds scatter a large portion of incoming ultrasound waves, implying that cloud cavitation cause energy shielding of nearby kidney stones. (Chapter 4).

- The magnitude of the energy shielding of a kidney stone by a layer of bubble clouds nucleated on the surface of a stone model are quantified through a combined experimental and numerical study. In the experiment, bubble-scattered acoustics are measured, and the evolution of bubbles are captured by high-speed imaging. Results of the simulation show favorable agreement with the experimental measurements of bubble-scattered acoustics and high-speed imaging of bubbles. The numerical results show that up to 90% of the incoming wave energy can be scattered by the bubbles. This indicates potential loss of efficacy of the treatment due to cavitation. A strong correlation between the amplitude of the scattered acoustics and the energy shielding is discovered (Chapter 5).

- The solution method for the dynamical equation that formulates the dynamics of spherical gas bubbles under mutual interactions used in the Lagrangian point-bubble approach is discussed (Appendix A).

1.7 Organization of this thesis

In Chapters 2, the acoustic source model is developed and implemented in the Euler equation. Focused ultrasound waves generated from medical transducers are simulated using the model. Experimental validation is presented.

Chapter 3 is devoted to development of the Eulerian-Lagrangian method. Special emphasis is placed upon sub-grid models for accurate simulation of bubble dynamics and upon reduced order models for accelerate computation. Supplemental materials on the speed-up of the simulation due to the model reduction and on the sub-grid model are documented in the chapter appendixes.

Chapter 4 presents the combined experimental and numerical investigation of the dynamics of bubble clouds in intense ultrasound fields. The numerical tools developed in Chapter 2 and 3 and experimental high-speed imaging of bubble clouds in a focused ultrasound wave are utilized to elucidate the anisotropic structure. Supplemental materials on the dynamics of bubble clouds under pressure excitation in the long wavelength regime are documented in the chapter appendix.

Chapter 5 presents quantification of the energy shielding of a model stone by a layer of cavitation bubbles during BWL through a combined experimental and numerical study.

A summary of conclusions and recommendations for future work are stated in Chapter 6.

Appendix A describes a solution method for the Rayleigh-Plesset equation extended for a system of multiple bubbles that can be used in the Lagrangian-point bubble approach.

Chapter 2

AN ONE-WAY ACOUSTIC SOURCE MODEL FOR SIMULATION OF MEDICAL ULTRASOUND

A part of this chapter is published in Wave Motion, 2017.

2.1 Overview

In this chapter, a model of an acoustic source is developed to simulate the generation of focused ultrasound by piezo-ceramic medical transducers. This aim is generalized as a mathematical problem to derive a unique, uniform distribution of source terms of the Euler- and Navier-Stokes equations on an arbitrary surface immersed in three-dimensional space to generate uni-directional (one-way) waves that propagate toward one side of the surface.

Simulation of linear and nonlinear acoustic fields using the Euler or Navier-Stokes equations is of use in diverse applications. For many applications, a source of acoustic waves is modeled as an oscillating surface. Treating the source surface as a real oscillating surface requires either body-fitted grids or immersed boundary/surface techniques, see for example Ginter et al. (2002), Krimmel et al. (2010), and Okita et al. (2011). In many cases, however, the surface itself is irrelevant to the ensuing dynamics, and we therefore seek an immersed, volumetric representation of acoustic waves produced at such an immersed surface, but without explicitly modeling the surface as a boundary condition. It is desirable in such a source to suppress generation of waves from the “back” of the surface; even if the presence of the direct waves generated can be tolerated, their reflection from open computational boundaries (with imperfectly non-reflecting boundary conditions) can lead to undesirable contamination of the solution. Improving the boundary conditions and/or enlarging the domain can be cumbersome (Colonius, 2004), and we therefore further seek to require that the source generates a set of unidirectional waves to the surface normal.

A related problem is parabolization (Lee et al., 2000; Towne and Colonius, 2015), which seeks to derive well-posed equations that support only waves propagating in a single direction (or over a limited range of angles). This is distinct from the simpler goal of the present chapter, which is to obtain one-way sources for use in the full governing equations. To do so, we use a concept from active noise reduction

(Williams, 1984; Nelson and Elliott, 1991), which is that by placing sound sources of controlled phase delay at proper locations, resulting sound waves propagating in a particular direction can be actively canceled (Kuo and Morgan, 1995). To do this, we distribute singular sources of mass, momentum, and energy on a three-dimensional surface and use a smeared Dirac delta function to regularize the singular distribution to a volume surrounding the surface. The Green's function solution for locally planar waves is then used to construct an anti-sound source for waves propagating in one direction. The superposition of these sources gives the desired one-way source.

The model is validated with analytical solutions for spherical and planar waves, and then used to model a single element, high-intensity focused ultrasound (HIFU) transducer and a multi-element array medical transducer on a portion of a spherical surface. We compare the acoustic field produced by the one-way source for the single-element transducer with experimental measurements reported by Canney et al. (2008) in both linear and nonlinear regimes, and that of the multi-element array medical transducer with measurements reported by Maxell (2016) in a linear regime. The proposed model can in principle be combined with any discretization of the Euler or Navier-Stokes equations.

2.2 Model

Inhomogeneous Euler equations

To model acoustic generation in a fluid by forcing, we consider the compressible, inhomogeneous Euler equations,

$$\frac{\partial \rho}{\partial t} + \nabla \cdot (\rho \boldsymbol{u}) = S_1, \tag{2.1}$$

$$\frac{\partial (\rho \boldsymbol{u})}{\partial t} + \nabla \cdot (\rho \boldsymbol{u}\boldsymbol{u} + p\mathcal{I}) = \boldsymbol{S}_2, \tag{2.2}$$

$$\frac{\partial E}{\partial t} + \nabla \cdot [(E + p)\boldsymbol{u}] = S_3, \tag{2.3}$$

where S_1, $\boldsymbol{S_2}$ and S_3 represent scalar mass, vector momentum, and scalar energy sources, respectively. We close the equation by stiffened gas equation of state:

$$p = (\gamma - 1)\rho\varepsilon - \gamma\pi_\infty, \tag{2.4}$$

where ε is the specific internal energy, with $\rho\varepsilon = E - \frac{1}{2}\rho\boldsymbol{u} \cdot \boldsymbol{u}$, and γ and π_∞ are parameters. Ideal gas equation of state is recovered with $\pi_\infty = 0$. In the present study we use $(\gamma, \pi_\infty) = (1.4, 0)$ for air and $(\gamma, \pi_\infty) = (7.1, 3.06 \times 10^9)$ for water, respectively.

Our goal is to find a combination of S_1, $\boldsymbol{S}_2$ and S_3 that generates one-way waves. To this aim, in the following we will compute general solutions of the equation in terms of arbitrary S_1, $\boldsymbol{S}_2$ and S_3. First we rewrite the equation in terms of linear perturbation about a quiescent state:

$$\frac{\partial \rho'}{\partial t} + \rho_0 \nabla \cdot \boldsymbol{u}' = S_1, \tag{2.5}$$

$$\frac{\partial \boldsymbol{u}'}{\partial t} + \frac{1}{\rho_0} \nabla p' = \frac{\boldsymbol{S}_2}{\rho_0}, \tag{2.6}$$

$$\frac{\partial p'}{\partial t} + \gamma (p_0 + \pi_\infty) \nabla \cdot \boldsymbol{u}' = (\gamma - 1) S_3, \tag{2.7}$$

where scripts $()'$ and $()_0$ denote variables at perturbed and stationary states, respectively. The linearized equations may be further manipulated to obtain

$$\frac{1}{c_0^2} \frac{\partial^2 p'}{\partial t^2} - \nabla^2 p' = \frac{\partial S_1}{\partial t} - \nabla \cdot \boldsymbol{S_2}, \tag{2.8}$$

$$\frac{\partial \boldsymbol{\omega}'}{\partial t} = \frac{\nabla \times \boldsymbol{S_2}}{\rho_0}, \tag{2.9}$$

$$\rho_0 T_0 \frac{\partial s'}{\partial t} = S_3 - \frac{c_0^2}{\gamma - 1} S_1, \tag{2.10}$$

where $\boldsymbol{\omega}' = \nabla \times \boldsymbol{u}'$ is the vorticity perturbation, s' is the entropy perturbation and T_0 is the backgrounds temperature. In general, with a presence of entropy source at the source surface (e.g. heat injection), the right hand side of equation (2.10) is non-zero. In the present study, to avoid generating entropy at the surface, we therefore set $S_3 = c_0^2/(\gamma - 1) S_1$. The curl of the source distribution S_2 will, unavoidably, create vorticity perturbations near an arbitrarily shaped surface. For some simple geometries, including plane waves, the curl will be identically zero, but, in any case, the vorticity generated will remain confined to a small Stokes layer near the surface in an otherwise quiescent media.

Using a Green's function, the solution of the equation (2.8) is given as

$$p(\boldsymbol{x}, t) = \int_0^t d\tau \int_{-\infty}^{\infty} d\boldsymbol{\zeta} G(t, \tau, \boldsymbol{x}, \boldsymbol{\tau}) (\frac{\partial S_1}{\partial t} - \nabla \cdot \boldsymbol{S_2}). \tag{2.11}$$

The essential idea of the present model is to consider a local region on the two-dimensional surface is locally spherical (with planar as a special case), and use the appropriate Green's function to derive a set of sources and anti-sources that produces the desired one-way wave field. To motivate the general case, we first examine planar, spherical, and cylindrical surfaces in the next two sections.

Plane wave

Forcing a three-dimensional, initially quiescent, unbounded field of domain is considered using the source model for one-way plane wave. To this end we define a source plane represented by $x = x_0$ on which the source of the same strength is uniformly distributed. The source terms S_1 and S_2 can be expressed as

$$S_1 = f(t)\delta(x - x_0) \tag{2.12}$$

$$S_2 = g(t)\delta(x - x_0), \tag{2.13}$$

where $f(t)$ and $g(t)$ are arbitrary functions satisfying causality condition: $f(t) = g(t) = 0$ for $t < 0$. Though the analytical expressions for S_1 and S_2 are presented by Williams (1984), in the context of anti-sound generation for active noise control, we repeat the derivation for clarity.

The Green's function for the one-dimensional wave equation is

$$G(t, \tau, \boldsymbol{x}, \boldsymbol{\tau}) = H(c(t - \tau) - |x - \zeta|), \tag{2.14}$$

where H is Heaviside step function. Substituting S_1 and S_2 into the solution above, we obtain

$$p(x,t) = \frac{c}{2}\int_0^t d\tau \int_{-\infty}^{\infty} d\zeta H(c(t-\tau) - |\zeta - x|)(\frac{\partial S_1}{\partial t} - \nabla \cdot \boldsymbol{S_2}) \tag{2.15}$$

$$= \frac{c}{2}\int_0^t d\tau \int_{-\infty}^{\infty} d\zeta H(c(t-\tau) - |\zeta - x|)(\dot{f}(\tau)\delta(\zeta - x_0) - g(\tau)\delta'(\zeta - x_0)) \tag{2.16}$$

$$= \underbrace{\frac{c}{2}\int_0^t d\tau H(c(t-\tau) - |x_0 - x|)\dot{f}(\tau)}_{\text{(A)}} \tag{2.17}$$

$$- \underbrace{\frac{c}{2}\int_0^t d\tau \int_{-\infty}^{\infty} d\zeta H(c(t-\tau) - |\zeta - x|) g(\tau)\delta'(\zeta - x_0)}_{\text{(B)}}. \tag{2.18}$$

We can compute the integrals (A) and (B) as

$$
\begin{aligned}
(A) =& \Big[H(c(t-\tau) - |x_0 - x|) f(\tau) \Big]_0^t + \int_{-\infty}^{\infty} c(\delta(c(t-\tau) - |x_0 - x|)) f(\tau) && (2.19) \\
=& f(t - \frac{|x_0 - x|}{c}) && (2.20) \\
(B) =& -\int_0^t d\tau \int_{-\infty}^{\infty} d\zeta \frac{\partial}{\partial \zeta} [H(c(t-\tau) - |\zeta - x|)] g(\tau) \delta(\zeta - x_0) && (2.21) \\
=& \int_0^t d\tau \int_{-\infty}^{\infty} d\zeta \frac{\partial |\zeta - x|}{\partial \zeta} \delta(c(t-\tau) - |\zeta - x|) g(\tau) \delta(\zeta - x_0) && (2.22) \\
=& \int_0^t d\tau \int_{-\infty}^{\infty} d\zeta \ \mathrm{sgn}(\zeta - x) \delta(c(t-\tau) - |\zeta - x|) g(\tau) \delta(\zeta - x_0) && (2.23) \\
=& \int_0^t d\tau \ \mathrm{sgn}(x_0 - x) \delta(c(t-\tau) - |x_0 - x|) g(\tau) && (2.24) \\
=& \frac{1}{c} g(t - \frac{|x_0 - x|}{c}) \mathrm{sgn}(x_0 - x) && (2.25) \\
=& -\frac{1}{c} g(t - \frac{|x_0 - x|}{c}) \mathrm{sgn}(x - x_0) && (2.26)
\end{aligned}
$$

to obtain

$$
p(x,t) = \frac{1}{2} \left(c f(t - \frac{|x_0 - x|}{c}) + g(t - \frac{|x_0 - x|}{c}) \mathrm{sgn}(x - x_0) \right). \tag{2.27}
$$

Thus we see that the mass source S_1 acts as a monopole that generates outgoing waves of the same amplitude and the same sign, propagating in both $\pm x$ directions, while the momentum source S_2 acts as a dipole that generates outgoing waves of the same amplitude, but opposite sign, propagating in $\pm x$ directions.
By defining $f(t) = g(t)/c$, we obtain

$$
\begin{aligned}
p(x,t) =& \frac{1}{2} \left[g(t - \frac{|x_0 - x|}{c}) + g(t - \frac{|x_0 - x|}{c}) \mathrm{sgn}(x - x_0) \right] && (2.28) \\
=& \frac{1}{2} \left[(1 + \mathrm{sgn}(x - x_0)) g(t - \frac{|x_0 - x|}{c}) \right] && (2.29) \\
=& H(x - x_0) g(t - \frac{|x - x_0|}{c}). && (2.30)
\end{aligned}
$$

This is clearly a one-way solution that represents waves propagating only in $+x$ direction. The waves caused by S_1 and S_2 propagating in $-x$ direction cancel with each other since they have the same amplitude but opposite signs. In addition to the noise control, cancellation of a component of waves propagating in a particular direction by superposition of multiple sources, has been applied to analytical representation of Gaussian beam by point sources and sinks (Sapozhnikov, 2012).

Spherical wave

Next, we consider an acoustic source distributed on a spherical surface represented by $x = x_0$, where x is now the radius in spherical polar coordinates, to generate a one-way spherical wave. The wave equation in terms of x becomes

$$\frac{1}{c_0^2}\frac{\partial^2 p}{\partial t^2} - (\frac{\partial^2 p}{\partial x^2} + \frac{2}{x}\frac{\partial p}{\partial x}) = \frac{\partial S_1}{\partial t} - \nabla \cdot \boldsymbol{S_2}, \tag{2.31}$$

where we have used the definition of Laplacian in spherical polar coordinates $\nabla^2(\cdot) = \frac{1}{x^2}\frac{\partial^2}{\partial x^2}x^2(\cdot)$. Notice that we can reformulate the equation in terms of xp:

$$\frac{1}{c_0^2}\frac{\partial^2 (xp)}{\partial t^2} - \frac{\partial^2 (xp)}{\partial r^2} = x\left[\frac{\partial S_1}{\partial t} - \nabla \cdot \boldsymbol{S_2}\right]. \tag{2.32}$$

Then we can apply the same Green's function used for the plane source distribution to obtain:

$$xp(x,t) = \frac{c}{2}\int_0^t d\tau \int_{-\infty}^{\infty} d\zeta H(c(t-\tau) - |\zeta - x|)\zeta(\frac{\partial S_1}{\partial t} - \nabla \cdot \boldsymbol{S_2}) \tag{2.33}$$

$$= \frac{c}{2}\int_0^t d\tau \int_{-\infty}^{\infty} d\zeta H(c(t-\tau) - |\zeta - x|) \tag{2.34}$$

$$\zeta[\dot{f}(\tau)\delta(\zeta - x_0) - g(\tau)\frac{1}{\zeta^2}\frac{\partial}{\partial \zeta}(\zeta^2\delta(\zeta - x_0))] \tag{2.35}$$

$$= \frac{cx_0}{2}\underbrace{\int_0^t d\tau H(c(t-\tau) - |x_0 - x|)\dot{f}(\tau)}_{\text{(A)}} \tag{2.36}$$

$$- \frac{cx_0^2}{2}\underbrace{\int_0^t d\tau \int_{-\infty}^{\infty} d\zeta \frac{1}{\zeta} H(c(t-\tau) - |\zeta - x|)g(\tau)\delta'(\zeta - x_0)}_{\text{(C)}}. \tag{2.37}$$

Integral (A) follows that used in the plane wave solution. The integral (C) differs from (B). We further compute

$$(\mathrm{C}) = -\int_0^t d\tau \int_{-\infty}^{\infty} d\zeta \frac{\partial}{\partial \zeta}\bigg(\frac{1}{\zeta}H(c(t-\tau)-|\zeta - x|)\bigg)g(\tau)\delta(\zeta - x_0) \tag{2.38}$$

$$= -\int_0^t d\tau \int_{-\infty}^{\infty} d\zeta\bigg(-\frac{\mathrm{sgn}(\zeta - x)}{\zeta}\delta(c(t-\tau)-|\zeta - x|) \tag{2.39}$$

$$-\frac{1}{\zeta^2}H(c(t-\tau)-|\zeta - x|)\bigg)g(\tau)\delta(\zeta - x_0) \tag{2.40}$$

$$= \underbrace{\frac{1}{x_0}\int_0^t d\tau \mathrm{sgn}(x_0 - x)\delta(c(t-\tau)-|x_0 - x|)g(\tau)}_{(\mathrm{B})} \tag{2.41}$$

$$+ \frac{1}{x_0^2}\underbrace{\int_0^t d\tau H(c(t-\tau)-|x_0 - x|)g(\tau)}_{(\mathrm{D})}. \tag{2.42}$$

Integral (D) becomes

$$(\mathrm{D}) = \Big[H(c(t-\tau)-|x_0 - x|)(G_g(\tau) + C)\Big]_0^t$$

$$+ \int_0^t d\tau c\delta(c(t-\tau)-|x_0 - x|)(G_g(\tau) + C(x)) \tag{2.43}$$

$$= G_g(t - \frac{|x_0 - x|}{c}) + C(x), \tag{2.44}$$

where $G_g(t)$ is the anti-derivative of $g(t)$ and $C(x)$ is an integration constant.

By using the expressions for (A) – (C), we obtain the following solution:

$$p(x,t) = \frac{1}{2}\frac{x_0}{x}\bigg(cf(t - \frac{|x_0 - x|}{c}) + g(t - \frac{|x_0 - x|}{c})\mathrm{sgn}(x_0 - x)$$

$$-\frac{c}{x_0}(G_g(t - \frac{|x_0 - x|}{c}) + C(x))\bigg). \tag{2.45}$$

$C(x)$ can be obtained by comparing this solution with the initial condition, $p(x, t = 0)$.

We see that, the waves generated by the mass source S_1 is a monopole solution like in the plane solution, while the waves generated by the momentum source S_2 also contain a monopole solution, in addition to the dipole component seen in the plane wave solution. The monopole component induced by S_2 clearly originates from the spherical geometry. It is straightforward that defining

$$f(t) = \frac{1}{c}g(t) + \frac{1}{x_0}(G_g(t - \frac{|x_0 - x|}{c}) + C(x)) \tag{2.46}$$

makes the following one-way wave solution propagating outward:

$$p(x,t) = \frac{x_0}{x} H(x - x_0) g(t - \frac{|x_0 - x|}{c}). \tag{2.47}$$

Despite its simplicity, this form of the one-way spherical wave source has not, to our knowledge, been previously reported.

Cylindrical wave

It is widely known that the cylindrical wave equation does not have a closed form of solution. The model of one-way cylindrical source in a simple form is therefore not available, unlike the plane or spherical one-way source. Instead, we can obtain an approximate solution in a closed form by solving the following inhomogeneous wave equation in terms of $\sqrt{x}p$, in analogous to equation (2.32):

$$\frac{1}{c_0^2}\frac{\partial^2(\sqrt{x}p)}{\partial t^2} - \frac{\partial^2(\sqrt{x}p)}{\partial x^2} = \sqrt{x}\left[\frac{\partial S_1}{\partial t} - \nabla \cdot \boldsymbol{S_2}\right]. \tag{2.48}$$

This approximation is valid for a cylindrical wave with a characteristic wave length much smaller than the radius of the cylindrical source plane (Whitham, 2011). The solution of equation(2.48) is readily available using the Green's function:

$$\begin{aligned} p(x,t) &= \frac{1}{2}\frac{c}{\sqrt{x}}\int_0^t d\tau \int_{-\infty}^{\infty} d\zeta H(c(t-\tau) - |\zeta - x|)\sqrt{\zeta}(\frac{\partial S_1}{\partial t} - \nabla \cdot \boldsymbol{S_2}) && (2.49) \\ &= \frac{1}{2}\frac{\sqrt{x_0}}{\sqrt{x}}\Bigg(c f(t - \frac{|x_0 - x|}{c}) + g(t - \frac{|x_0 - x|}{c})\mathrm{sgn}(x_0 - x) && (2.50) \\ &\quad - \frac{c}{\sqrt{x_0}}(G_g(t - \frac{|x_0 - x|}{c}) + C(x))\Bigg). && (2.51) \end{aligned}$$

It is straightforward that defining

$$f(t) = \frac{1}{c}g(t) + \frac{1}{\sqrt{x_0}}(G_g(t - \frac{|x_0 - x|}{c}) + C(x)) \tag{2.52}$$

makes the following one-way wave solution:

$$p(x,t) = \frac{\sqrt{x_0}}{\sqrt{x}} H(x - x_0) g(t - \frac{|x_0 - x|}{c}). \tag{2.53}$$

Arbitrary, smooth surfaces

For the general case of acoustic source that is distributed on combinations of arbitrary but smooth, two-dimensional surfaces, we may combine the plane, cylindrical and/or spherical one-way sources as building blocks that align on the source plane. As an example of such cases, in section 2.4 we will demonstrate a simulation of acoustic fields generated by a multi-element array medical transducer, using a combination of spherical one-way sources to model the transducer elements.

2.3 Numerical implementation

In principle, the models for one-way source derived in the previous section can be used for any numerical methods that solve the Euler or Navier-Stokes equations. For good accuracy, the waves should be introduced into a region of approximately quiescent flow, and the amplitude should be limited such that the linearization, upon which the source model rests, holds. Regardless, we can simply amend the derived source terms to the original nonlinear equations. In order to demonstrate verifications and validations of the model, in the present chapter we use a finite-volume, fifth-order WENO scheme (Titarev and E. Toro, 2004) both in cylindrical coordinates with an azimuthal symmetry and Cartesian coordinates. High-order WENO scheme is particularly capable of accurately simulating discontinuous solutions, including shockwave and material interface (Coralic and Colonius, 2014).

In the following we describe a method of numerical representation of the governing equation in cylindrical coordinates with azimuthal symmetry. That in 3D Cartesian coordinates can be trivially derived in a similar manner, and thus is omitted here. We spatially discretize the forced Euler equation in the following form:

$$\frac{\partial \boldsymbol{q}}{\partial t} + \frac{\partial \boldsymbol{f}(\boldsymbol{q})}{\partial z} + \frac{\partial \boldsymbol{g}(\boldsymbol{q})}{\partial r} = \boldsymbol{s}^g(\boldsymbol{q}) + \boldsymbol{s}^s(\boldsymbol{q}), \tag{2.54}$$

where $\boldsymbol{q}$ is the vector of conservative variables, $\boldsymbol{f}$, $\boldsymbol{g}$ are vectors of fluxes, $\boldsymbol{s}$ is the vector of source terms and the superscripts $(\cdot)^g$ and $(\cdot)^s$ denote the geometrical source and the acoustic source, respectively. This formulation is convenient since the variables can be discretized in 2D Cartesian coordinates (E. F. Toro, 2013). We integrate the above equation in arbitrary finite volume grid cell

$$I_{i,j} = [z_{i-1/2}, z_{i+1/2}] \times [r_{j-1/2}, r_{j+1/2}], \tag{2.55}$$

where i and j are the indices of the cells in $z-$ and $r-$directions, and $z_{i\pm1/2}$ and $r_{j\pm1/2}$ are the positions of cell faces. At each finite volume cell, we express the equation in the following semi-discrete form:

$$\begin{aligned}\frac{d\boldsymbol{q}_{i,j}}{dt} = \frac{1}{\Delta z_i}[\boldsymbol{f}_{i-1/2,j} - \boldsymbol{f}_{i+1/2,j}] + \frac{1}{\Delta r_j}[\boldsymbol{g}_{i,j-1/2} - \boldsymbol{g}_{i,j+1/2}]\\ + \frac{1}{2r_j}[\boldsymbol{s}^g_{i,j-1/2} + \boldsymbol{s}^g_{i,j+1/2}] + \boldsymbol{s}^s_{i,j}.\end{aligned} \tag{2.56}$$

The conservative variables at cell faces are reconstructed by 5th order WENO scheme from the cell-centered values, then are used in HLLC Riemann solver to calculate the fluxes. A symmetry boundary condition is used at the domain boundary corresponding to the axis of symmetry, $r = 0$, and approximately nonreflecting, characteristic boundary conditions are used at other domain boundaries (Thompson, 1987). Further details are provided in Coralic and Colonius (2014).

We express the forcing term $\boldsymbol{s}^s$ defined on a surface Γ using the following integral representation:

$$\boldsymbol{s}^s = \int_\Gamma \boldsymbol{\Omega}_\Gamma(\boldsymbol{\xi}, t)\delta(\boldsymbol{X}(\boldsymbol{\xi}, t) - \boldsymbol{x})d\boldsymbol{\xi}, \tag{2.57}$$

where $\boldsymbol{\xi}$ is the coordinate defined on Γ, $\boldsymbol{\Omega}_\Gamma(\boldsymbol{\xi}, t)$ is the forcing, and $\boldsymbol{X}(\boldsymbol{\xi}, t) \in \Gamma$ is the function that maps $\boldsymbol{\xi}$ to $\boldsymbol{x}$. In $z - r$ 2D axi-symmetric coordinates, arbitrary surface with axi-symmetric geometry can be represented by a curve L. L can be parametrized by a single scalar ξ, thus we have

$$\boldsymbol{s}^s = \int_\Gamma \boldsymbol{\Omega}_\Gamma(\xi, t)\delta(\boldsymbol{X}(\xi, t) - \boldsymbol{x})d\xi, \tag{2.58}$$

where $d\xi$ is the line element of L.

We express the forcing at cell $I_{i,j}$ by

$$\boldsymbol{s}^s_{i,j} = \sum_{k=1}^{K} \boldsymbol{\Omega}_\Gamma(\xi_k, t)\delta_h(|\boldsymbol{X}(\xi_k, t) - \boldsymbol{x}_{i,j}|)\Delta\xi_k, \tag{2.59}$$

where δ_h is a smeared delta function, $\Delta\xi_k$ is the length of kth line elements of L, and $k \in \mathbb{Z} : k \in [1, K]$. Various forms of δ_h are available (Peskin, 2002). In the present study we employ the second-order, two-dimensional Gaussian function:

$$\delta_h(h) = \frac{1}{(\sqrt{2\pi}\sigma)^2} e^{-\frac{1}{2}\frac{h^2}{\sigma^2}}, \tag{2.60}$$

where σ is the support width. Typically $\sigma = O(\Delta)$ is taken, where Δ is the characteristic grid size at the region of the source. The overall rate of grid convergence of the scheme is second-order in smooth regions of the field. Note that the second order accuracy of the scheme for smooth regions is due to the second-order accurate spatial discretization of the geometrical source, shown in equation (2.56), despite 5th order WENO scheme is used for reconstruction of variables at cell faces. Temporal integration of the partial differential equation is realized by third-order total variation diminishing Runge-Kutta scheme (TVD-RK).

2.4 Numerical Results

We now verify and validate the one-way source models. First, we verify the source model by simulating the one- and three-dimensional sources for which analytical solutions are available. Next we consider HIFU waves produced on a portion of a spherical shell and compare with previous experimental measurements as well as numerical solutions employing the KZK equation. Finally, we apply the spherical one-way source to 3D simulation of a ultrasound generation with a multi-element array medical transducer, and then compare the simulated acoustic fields with experimental measurements.

Simulation of a plane Gaussian pulse

We first simulate a one-way, Gaussian acoustic pulse in air propagating in $+z$ direction from the source distributed on the plane of $z = 0$. On $z - r$ Cartesian grid, since the line source is aligned on the r axis, source representation can be simplified by smearing the source in $\pm z$ direction to express the source term as

$$\boldsymbol{s}^{s}_{i,j} = \boldsymbol{\Omega}_{\Gamma}(t)\delta_h(|r_i|), \tag{2.61}$$

where $\boldsymbol{\Omega}_{\Gamma}(t) = [f(t)/c_0, f(t), 0, c_0^2 f(t)/(\gamma - 1)]$ and

$$f(t) = \frac{p_a}{\sqrt{2\pi}\sigma_t} e^{-\frac{1}{2}\frac{(t-t_0)^2}{\sigma_t^2}}, \tag{2.62}$$

where σ_t is the support width of the Gaussian pulse in the time space and t_0 is the delay. We take $p_a = 10$ Pa, $\sigma_t = 5$ μs and $t_0 = 20$ μs. The simulation domain is $z \in [-20, 20]$ and $r \in [0, 20]$ mm. The initial condition is given by $(\rho, u, p) = (1.204, 0, 101325)$, where the density, velocity, and pressure are in kg/m^3, m/s and Pa, respectively. The simulation is evolved with a constant time-step, $\Delta t = 160$ ns. 200×100 uniform computational grids are used.

In figure 2.1 (a) we compare the analytical and numerical solutions of p' at $t = 49.3$ μs. For reference, We plot the components of the numerical solution of p' that emanate from the mass and the momentum sources in figure 2.1 (b) and (c), respectively. The results show that the numerical solution agrees well with the analytical solution. As expected, in the right-going part of the numerical solution, the component from the mass source, identified as a monopole, has the same amplitude and sign with those of the component from the momentum source, thus they get amplified with each other. In the left-going part, the component from the mass source and that of the momentum source have the same amplitude but opposite sign, thus they cancel with each other.

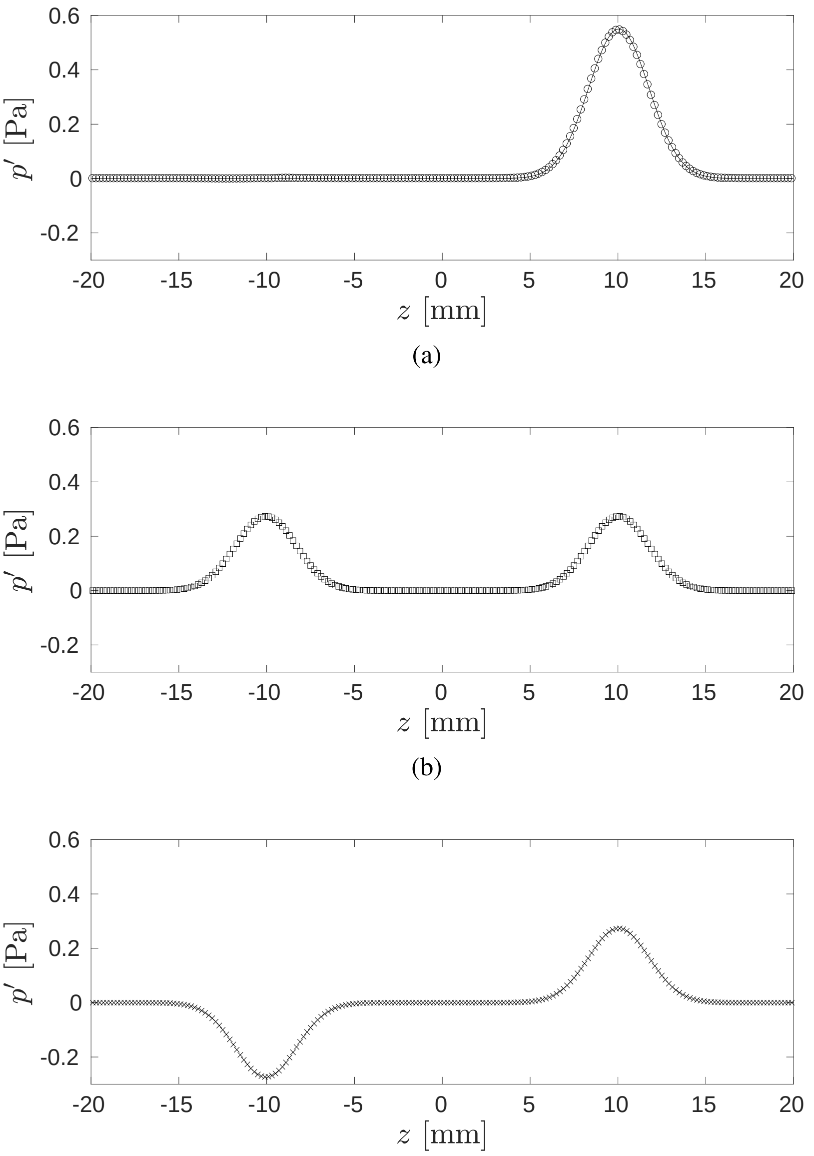

(a)

(b)

(c)

Figure 2.1: Pressure distribution on the z-axis at $t = 49.3\ \mu$s. (a) The analytical (-) and numerical (∘) solutions are compared. The components of the numerical solution that emanate from (b) the mass source (□) and (c) the momentum source (×) are plotted for reference.

Simulation of a spherical sinusoidal pulse

Secondly, we simulate a one-way, sinusoidal acoustic pulse in water propagating inward from a uniform acoustic source distributed on a spherical shell with its center located at the origin, and with a radius of $r_0 = 15$ mm. The expressions used for the source terms are $\boldsymbol{\Omega}_\Gamma(\xi, t) = [f(t), g_z(\xi, t), g_r(\xi, t), c_0^2 f(t)/(\gamma - 1)]$, where, with angular frequency $\omega = 2\pi f_s$,

$$f(t) = \frac{p_a}{c_0}\sin(\omega(t - t_0)) + \frac{p_a}{r_0}(G_g(\omega(t - t_0)) + C), \tag{2.63}$$

$$g_z(\xi, t) = -p_a \sin(\omega(t - t_0))\cos\xi, \tag{2.64}$$

$$g_r(\xi, t) = -p_a \sin(\omega(t - t_0))\sin\xi. \tag{2.65}$$

The spherical shell is represented as an upper hemi-circle in the $z - r$ coordinate plane. ξ is defined as the polar angle that parametrizes the arc of the hemi-circle; $\xi \in \mathbb{R} : \xi \in [0, \pi]$ and $\boldsymbol{X}(\xi) = [r_0\cos\xi, r_0\sin\xi]$. The geometrical components of the mass source $G_g(t)$ and C are expressed as

$$G_g(t) = \int -\sin(\omega\tau)d\tau = \frac{1}{\omega}\cos(\omega t), \tag{2.66}$$

$$C = -G_g(0) = -\frac{1}{\omega}. \tag{2.67}$$

We take $p_a = 10$ Pa, $f_s = 3.0 \times 10^5$ Hz, and $t_0 = \pi/(2f)$ s. The simulation domain is $z \in [-20, 20]$ and $r \in [0, 20]$ mm. We evolve the simulation with the initial condition given by $(\rho, u, p) = (1000, 0, 101325)$, where the density, velocity, and pressure are in kg/m^3, ms^{-1} and Pa, respectively. The simulation is evolved with a constant time-step, $\Delta t = 20$ ns. 800×400 uniform computational grids are used.

In figure 2.2 (a) we compare the distribution of the analytical and numerical solutions of the pressure scaled by the radial coordinate, rp'/r_0, on the r-axis at $t = 5.12$ μs. The numerical solution with and without the geometric component in the source term, $G_g(t)$, are plotted. The result shows that the numerical solution with $G_g(t)$ agrees well with the analytical solution, while that without $G_g(t)$ does not. Figure 2.2 (b) shows the error defined as $E = r((p'_{\text{Anal}} - p'_{\text{Numel}})/p_{\text{a}})/r_0$ for the numerical solution with and without $G_g(t)$. The difference between the two errors corresponds to the wave excited by $G_g(t)$ in the numerical solution. The difference in the error is composed of an incoming and outgoing component of the same form and amplitude. This observation agrees with the result of our modeling that the geometrical component of the momentum source corresponds to monopole excitation. Finally, a convergence study is performed on the pressure. Figure 2.3

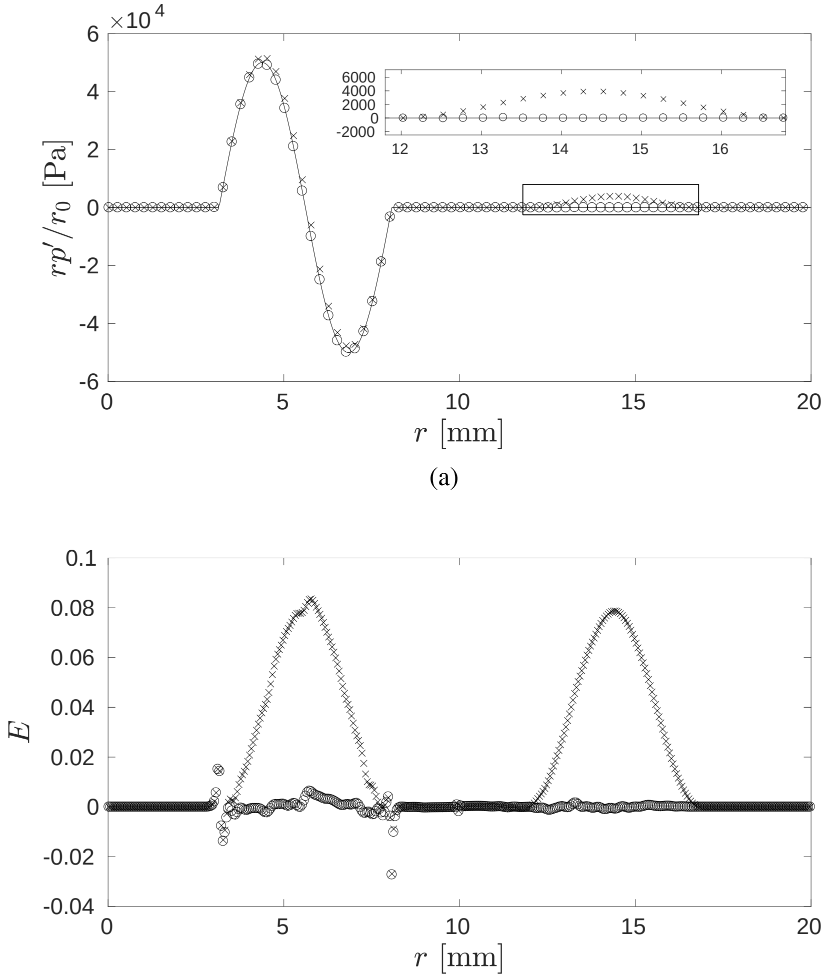

(a)

(b)

Figure 2.2: (a)The distribution of the scaled pressure rp'/r_0 on the r-axis at $t = 5.12$ μs. The analytical ($-$) and numerical solutions are compared. The numerical solution with ($\circ$) and without ($\times$) the geometric component in the source term, $G_g(t)$), are plotted. One of every five data points are shown for the numerical solutions. (b)The magnitude of the scaled error between the same analytical and numerical solutions, $E = r((p'_{\text{Numel}} - p'_{\text{Anal}})/p'_{\text{Anal}})/r_0$, on the r-axis at $t = 5.12$ μs. The errors in terms of the numerical solution with the geometric component ($\circ$) and without the geometric component ($\times$) in the source term are plotted.

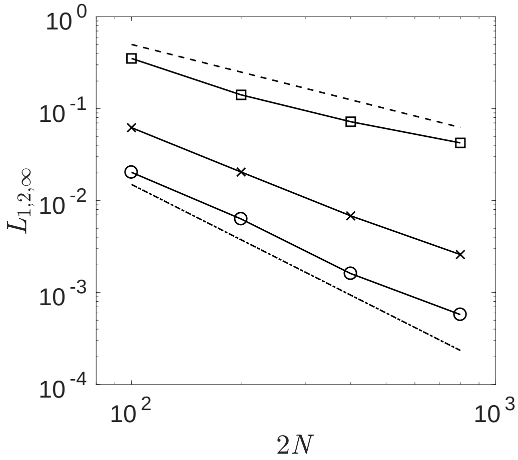

(a)

Figure 2.3: $L_{1,2,\infty}$-norm of the error between the analytical solution and the numerical solution at $t = 5.12$ μs as a function of the grid size ($2N \times N$). Reference slopes for the first and second order convergence are included.

shows $L_{1,2,\infty}$-norm of the error between the analytical solution and the numerical solution with $G_g(t)$, both of which are shown in figure 2.2 (a), as a function of the grid size. The result indicates that the numerical solution is first-order accurate. While the underlying finite-volume scheme being used is second-order accurate (for smooth solution), our regularization of the singular source on the scale of the grid spacing strands a first-order error in the source representation (Tornberg and Engquist, 2003).

High-Intensity Focused Ultrasound

Next, we simulate a focused ultrasound field generated by a medical transducer studied by Canney et al. (2008). The transducer is composed of a single element of spherically focused, piezoceramic crystal with a characteristic frequency of 2.158 MHz. Following the linear analysis of a focused acoustic field by Canney et al., we define the aperture and radius of curvature of the transducer as 42.0 mm and 44.4 mm, respectively. On the $z - r$ coordinate plane, we define the source as the arc of the circular section with its center located at the origin, radius $r_0 = 22$ mm and central angle $\alpha/2$. ξ is defined as the polar angle that parametrizes the arc of the circular section; $\xi \in \mathbb{R} : \xi \in [0, \alpha/2]$ and $\boldsymbol{X}(\xi) = [r_0\cos\xi, r_0\sin\xi]$. Definition of the source follows equation (2.63-2.65). The simulation domain is $z \in [-0.6, 68.4]$ and $r \in [0, 24]$ mm. The initial condition is given by $(\rho, u, p) = (1, 0, 101325)$, where the density, velocity and pressure are in kg/m^3, m/s and Pa, respectively.

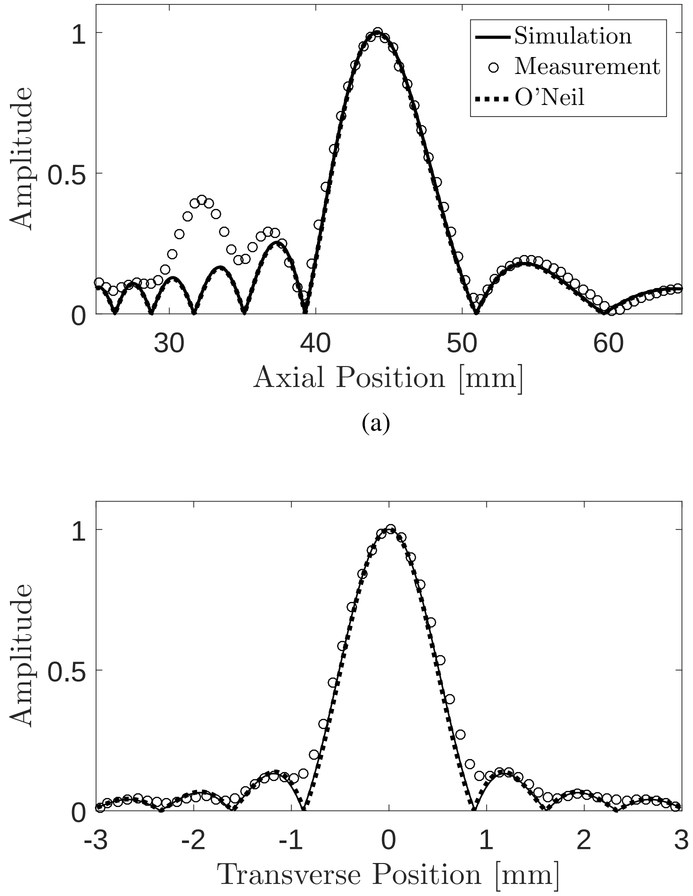

(a)

(b)

Figure 2.4: The (a)axial and (b)focal scans of the pressure field in water by the SEA hydrophone for $p_0 = 1.0 \times 10^4$ Pa. The result of the direct numerical simulation (-), and SEA hydrophone measurement by Canney et al. (2008) (○), and O'Neal analytic solution (- -) (O'Neil, 1949) are compared.

To validate the source model for the transducer, we first simulate a focused acoustic field in the linear regime with a source amplitude of $p_a = 1.0 \times 10^4$ Pa to obtain the axial and focal scan of the pressure, for which an experimental measurement and analytical solution are available. The simulation is evolved with a constant time-step, $\Delta t = 6.75$ ns. 3250×1200 uniform computational grids, with a cell size of $\Delta x = \Delta y = 20$ μm, are used. In figure 2.4 we compare the results. The present simulation agrees very well with the analytical solution, and relatively well with the experimental measurement. We also note that the gain of the transducer obtained in the simulation is $Ga = 48$, where $Ga = p_\mathrm{f}/p_\mathrm{a}$ and p_f is the focal pressure. The value of the gain agrees with that of both the measurement and analytical solution. The discrepancy between the experimental measurement, notably seen in the pre-focal regions on the axis, can be explained by a non-uniform velocity distribution on the piezoceramic plate of the real transducer, which is not considered in the simulation and the analytical solution.

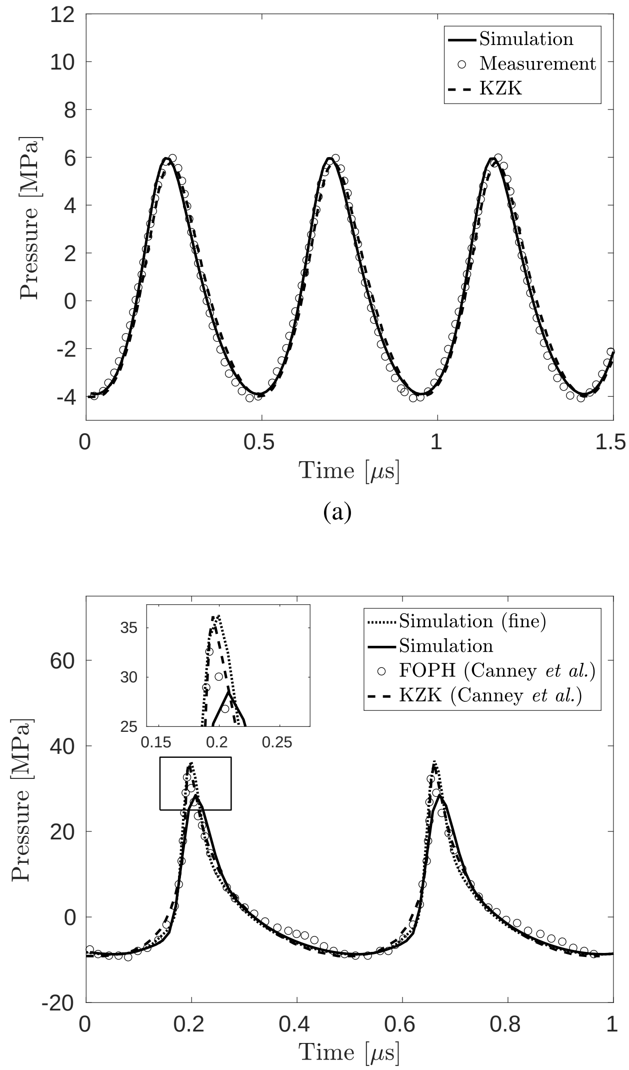

(a)

(b)

Figure 2.5: The focal pressure evolutions in water with (a) $p_a = 1.0 \times 10^5$ and (b) $p_a = 2.9 \times 10^5$. In the plot (a), the result of the direct numerical simulation (–), FOPH measurement by Canney et al. (2008) (○), and analytical solution calculated with the KZK equation presented in Canney et al. (2008) (- -) are compared. In the plot (b), the results of the direct numerical simulation with a cell size of $\Delta x = \Delta y = 12.5$ μm (- -) and $\Delta x = \Delta y = 20$ μm (–) are compared with FOPH measurement and analytical solution calculated with the KZK equation.

Next we simulate focused acoustic fields in nonlinear regimes with a source amplitude of $p_a = 1.0 \times 10^5$ Pa using uniform grids with a cell size of $\Delta x = \Delta y = 20$

μm, and $p_a = 2.9 \times 10^5$ Pa using two distinct resolutions of uniform grids with a cell size of $\Delta x = \Delta y = 20$ μm and $\Delta x = \Delta y = 12.5$ μm, respectively. In figure 2.5 we compare the focal pressure evolutions obtained from the present simulations and the experimental measurement conducted by Canney et al. The corresponding solutions of the KZK equation presented in Canney et al are also plotted. In the case with $p_a = 1.0 \times 10^5$ Pa, shown in figure 2.5 (a), the result of the simulation agrees very well with the measurement as well as the solution of the KZK equation. The acoustic field in the focal region is in a weekly nonlinear regime. The amplitude of the positive peak is 6 MPa, while that of the negative peak is 4 MPa. The wave form is not largely distorted from a sinusoidal form. In the case with $p_a = 2.9 \times 10^5$ Pa, shown in figure 2.5 (b), the wave form obtained by the simulations agrees well with the measurement. The maximum pressure obtained by the simulation with coarse grids is slightly lower than that of the others, shown in the inset of figure 2.5 (b). This is due to numerical dissipation that reduces the amplitude of the sharp peak formed by nonlinear sharpening. As shown by the result of the simulation using fine grids, this dissipation can be reduced by refining the grid.

figure 2.6 shows the flooded pressure contour of the simulated acoustic fields with $p_a = 2.9 \times 10^5$ at $t = 20$ μs and $t = 70$ μs. The waves generated on the source plane propagate and get focused toward the focal region. Waves propagating outward from the source plane are canceled.

Multi-element array medical transducer

Finally, we simulate a focused acoustic field generated by a medical, multi-element array medical transducer in a linear regime using the one-way spherical source, and validate the simulation with an experimental measurement. The purpose of this case is to demonstrate the feasibility of the proposed source models for applications to a non-trivial source geometry.

Figure 2.7 (a) shows an image of the multi-element array medical transducer. The transducer is composed of 18 circular elements made from a ring-shaped piezoceramic plate with an outer diameter of 38.1 mm and an inner diameter of 12.7 mm. Each of the elements is designed to generate a spherical wave front, with a radius of 150 mm, that propagates inward to the center corresponding to the focal point. The detailed design of the transducer is reported by Maxell (2016). Figure 2.7 (b) shows the modeled source surfaces. Unlike the single-element transducer considered in section 2.4, the source geometry of the multi-element array medical transducer is

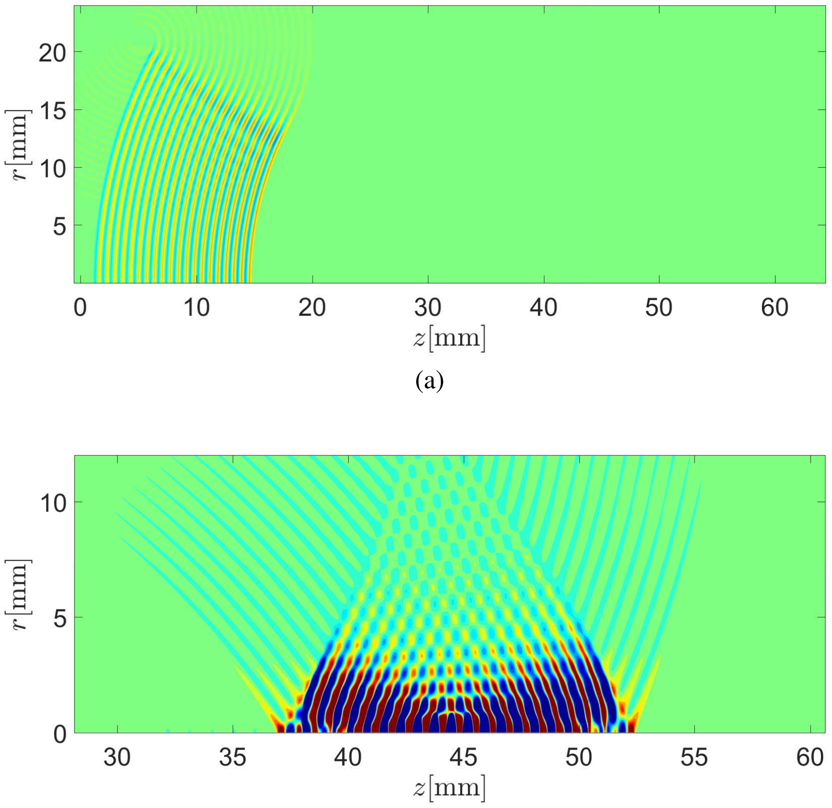

(a)

(b)

Figure 2.6: Flooded pressure contour of the simulated acoustic fields with $p_a = 2.9 \times 10^5$ at (a) $t = 20$ μs and (b) $t = 70$ μs. The contour level is ±1 MPa

not fully axi-symmetric. Therefore we use an x-y-z Cartesian coordinate system in this case of simulation. To model the element, we distribute the one-way spherical source on a ring-shaped portion of a spherical surface with a radius of 150 mm with its center located at the origin. Correspondingly, using a smeared delta function, the strength of the source is regularized onto three-dimensional grid cells neighboring the surface.

The expressions used for the source terms are

$$\mathbf{\Omega}_\Gamma(\xi, \eta, t) = \chi(\boldsymbol{X})[f(t), g_x(\xi, \eta, t), g_y(\xi, \eta, t), g_z(\xi, \eta, t), c_0^2 f(t)/(\gamma - 1)], \tag{2.68}$$

where, with angular frequency $\omega = 2\pi f_s$,

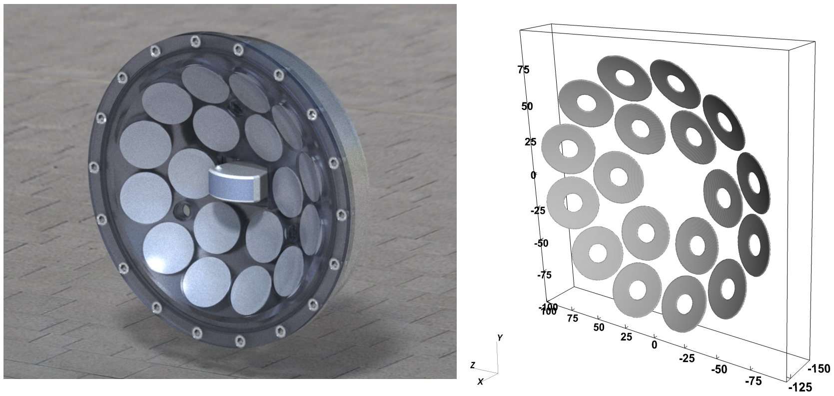

(a) (b)

Figure 2.7: Multiarray transducer with 18 elements considered in the present study. (a) Real transducer. The ring-shaped piezo-ceramic elements are covered by acoustic lenses. (b) Modeled source distribution used in the simulation. The length unit used in the figure is mm. Each element is modeled as a ring-shaped source plane aligned on a spherical section with a radius of 150 mm.

$$f(t) = \frac{p_a}{c_0}\sin(\omega(t-t_0)) + \frac{p_a}{r_0}(G_g(\omega(t-t_0)) + C), \tag{2.69}$$

$$g_x(\xi,\eta,t) = -\,p_a \sin(\omega(t-t_0))\cos\xi\cos\eta, \tag{2.70}$$

$$g_y(\xi,\eta,t) = -\,p_a \sin(\omega(t-t_0))\cos\xi\sin\eta, \tag{2.71}$$

$$g_z(\xi,\eta,t) = -\,p_a \sin(\omega(t-t_0))\sin\xi. \tag{2.72}$$

[1] ξ and η are defined as the polar and azimuthal angles that parametrize the spherical section; $\xi, \eta \in \mathbb{R} : \xi \in [0,\pi], \eta \in [-\pi,\pi]$, and $\boldsymbol{X}(\xi,\eta) = [r_0\cos\xi\cos\eta, r_0\cos\xi\sin\eta, r_0\sin\xi]$. χ is an indicator function that takes a value of 1 when Lagrangian point $\boldsymbol{X}(\xi,\eta)$ is within the region of the defined ring-shaped transducer surfaces, and 0 elsewhere. G_g and C follow equations (2.66) and (2.67), respectively.

To validate the source model, we simulate a focused acoustic field in a linear regime with 20 cycles of a sinusoidal form of pressure waves with a frequency of 340 kHz and a source amplitude of 10 Pa. The spacial configuration of the source and the resulting acoustic field are symmetric along the x-y and x-z planes that intersect the x-axis. To reduce the computational cost, we simulate a domain of $x \in [-160, 60]$,

---

[1] Note that we set $\boldsymbol{\xi} = [\xi, \eta]^{\mathrm{T}}$ in equation (2.57). For regularization of the singular sources, we use the second-order, three-dimensional Gaussian function: $\delta_h(h) = \frac{1}{(\sqrt{2\pi}\sigma)^3} e^{-\frac{1}{2}\frac{h^2}{\sigma^2}}$.

$y \in [0, 100]$ and $z \in [0, 100]$ mm, with symmetry boundary conditions applied along the x-y and x-z planes. Non-reflecting boundary conditions are applied on the other domain boundaries. The simulation is evolved with a constant time-step, $\Delta t = 36.7$ ns. 1320×600×600 uniform computational grids are used.

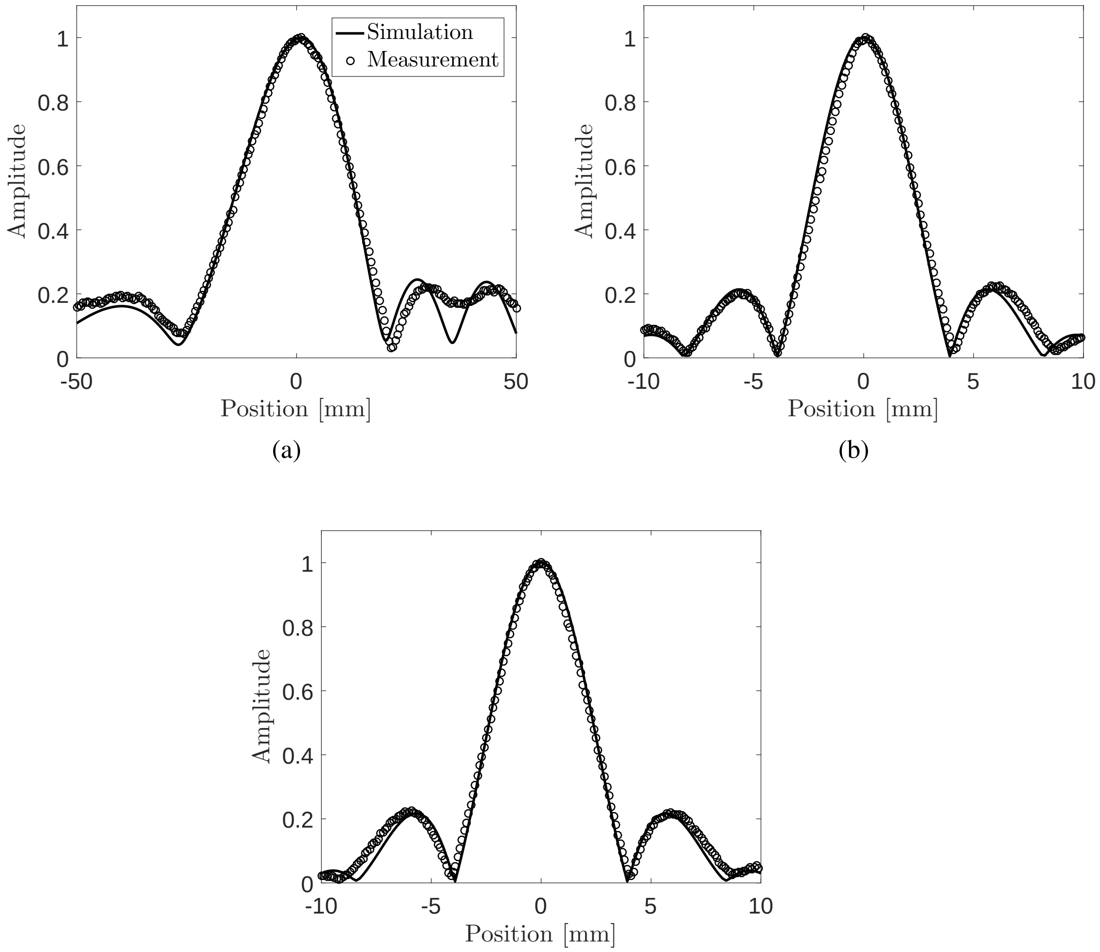

(a)

(b)

(c)

Figure 2.8: The scans of the pressure field around the focal point generated by the multi-element array medical transducer along the (a) x-axis, (b) y-axis, and (c) z-axis, respectively. The amplitudes of the pressure are normalized by their maximum values in each plot. Results obtained in the present simulation and the hydrophone measurement are compared.

Figure 2.8 shows the scans of the pressure field around the focal point along the coordinate axes obtained from the simulation and a corresponding experimental measurement using a capsule hydrophone reported by Maxell (2016). The present simulation agrees well with the measurement along all the axes, except for the region around x = 30-40 mm on the x-axis. The discrepancy on the x-axis could be reduced by improving the accuracy of measurements and/or using more accurate geometric parameters of the source in simulations (e.g. the size of the piezo-ceramics plates). Note that the linear gain of the transducer obtained from the present simulation was Ga = 27.

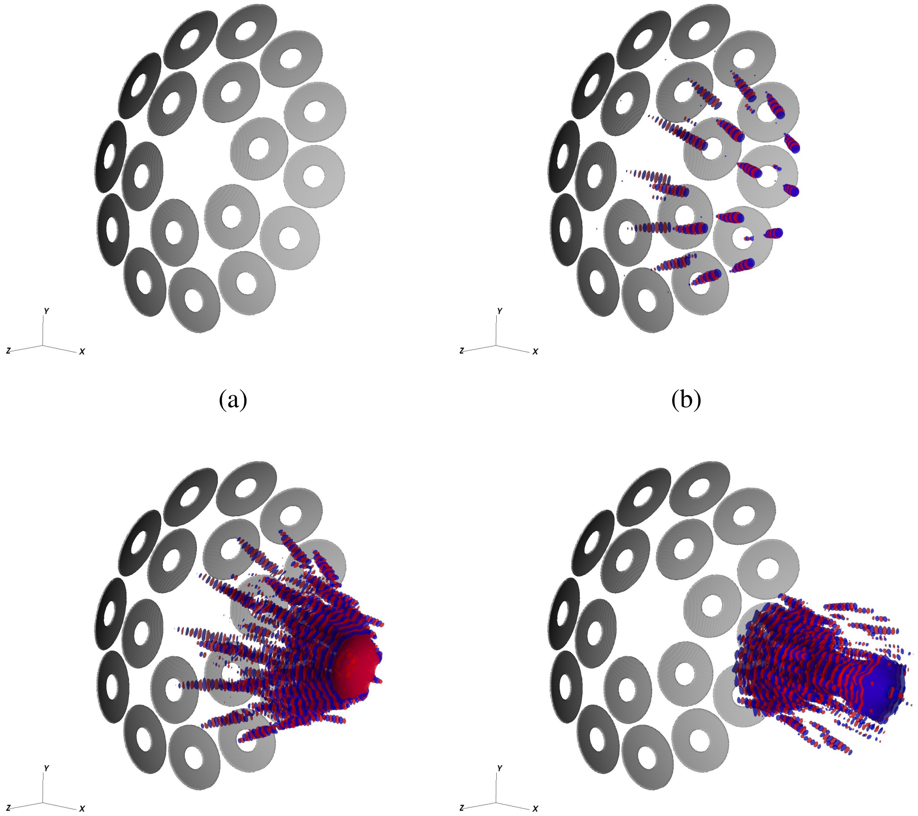

(a) (b) (c) (d)

Figure 2.9: Pressure iso-contours of the simulated acoustic fields with the contour levels of -200 Pa (blue color) and 200 Pa (red color) at (a)0, (b)40, (c)80 and (d)120 μs.

Figure 2.9 shows the pressure iso-contours of the simulated acoustic fields with the contour level of -200 Pa (blue color) and 200 Pa (red color), respectively. The train of waves generated at each element overlaps with each other as they propagate, then converges toward the focal point. As shown in figure 2.9 (d), at t = 120 μs, the leading part of the train of waves diverge after passing the focal point.

2.5 Summary

In this chapter, simple, general models of source terms are constructed for the Euler/Navier-Stokes equations that generate unidirectional radiation from one face of an arbitrary, smooth surface. The models are built on a singular distribution of simple monopole and dipole sources that are regularized on the computational grid. The models were verified by simulation of one-way Gaussian wave in air and spherical waves in water, solved using a numerical method consisted of a finite-volume WENO scheme. The scheme is applied to simulate focused ultrasound fields generated by a HIFU transducer on 2D axi-symmetric grids and a multi-element array medical transducer on 3D grids. For the HIFU transducer, the obtained ultrasound fields on the central axis and focal axis in a linear regime as well as the focal pressure evolutions in a non-linear regime agreed well with those of experimental measurements reported by Canney et al. (2008). For the multi-element array medical transducer, simulated focal scans of the ultrasound fields in a linear regime agree well with experimental measurements reported by Maxell (2016). The source models for plane, cylindrical, and spherical one-way waves presented can be used as building blocks to construct a source distributed on a surface with arbitrary geometries and strength. In addition to acoustic waves in a pure fluid, the one-way source models can be also adapted to various hyperbolic systems. The fields of applications can include seismology, astrophysics, and elastic solid mechanics.

Chapter 3

EULERIAN-LAGRANGIAN METHOD FOR SIMULATION OF CLOUD CAVITATION

A part of this chapter has been accepted for publication in Journal of Computational Physics.

3.1 Overview

In this chapter, an Eulerian-Lagrangian method is developed for simulation of cloud cavitation induced by an intense ultrasound wave.

In the method, the dynamics of bubbly-mixture is described using the volume-averaged equations of motion that fully account for the compressibility of liquid. The continuous phase is discretized on an Eulerian grid, while the gas phase is modeled as spherical, radially oscillating cavities that are tracked as Lagrangian points at the sub-grid scale. The dynamics of the continuous phase is evolved using a high-order, finite-volume weighted essentially non-oscillatory (WENO) scheme, that was originally developed for simulation of viscous, compressible, multi-component flows (Coralic and Colonius, 2014) and is capable of capturing strong pressure waves with fine structures. The volume of bubbles is mapped onto the Eulerian grids as the void fraction using a regularization kernel. The radial oscillation of each bubble is evolved by solving the Keller-Miksis equation. When the grid size is smaller than the characteristic inter-bubble distance, the method is capable of capturing the violent cavitation growth and collapse of each bubble as well as resolving the strong, complex structures of bubble-scattered pressure waves in the liquid.

For the most general cases, the continuous phase is discretized on a three-dimensional Cartesian grid, and a standard regularization kernel is used to map the volume of bubbles onto the field of void fraction. To reduce the cost for simulations of a bubbly-mixture that possesses translational or axi-symmetric homogeneity, we newly introduce reduced-order models. In the models, the continuous phase is discretized on two-dimensional or axi-symmetric grids. The volume of bubbles distributed in three-dimensional space is mapped onto the two-dimensional or axi-symmetric field of void fraction by using a modified regularization kernel. By doing so, the cost of computations required to solve for the continuous phase is reduced from $O(N^3)$ to $O(N^2)$, where N is the number of grid cell per dimension, in comparisons to the three-dimensional model.

In order to properly close the Keller-Miksis equation, the pressure field at the sub-grid scale needs to be appropriately modeled. In the case of the three-dimensional model, in each grid cell that encloses a bubble, the contribution of the pressure wave scattered by the bubble to the averaged pressure in the cell can become significant, and thus the pressure of the cell cannot be directly used to force the oscillations of bubble. In that case, following the scheme proposed by Fuster and Colonius (2011), we obtain the component of the cell-averaged pressure that forces the oscillations of bubble by using the state of the bubble and potential flow theory at the sub-grid scale. In the two-dimensional and axi-symmetric models, the discretized pressure field is treated as uniform in the direction of symmetry, despite the three-dimensionality of the true pressure field associated with any distribution of bubbles. In order to reduce the error associated with the neglected three-dimensional pressure fluctuations, we model the spatial distribution of the pressure at the sub-grid scale as white noise. In each grid cell that contains a bubble, we estimate the variance of the noise by sampling the pressure in the neighboring cells, with an assumption that the pressure fluctuations are locally, spatially isotropic on the scale of the sampling window. The noise is expressed by superposing Fourier modes with pre-computed, randomized phases, following a method of expressing stochastic fluctuations in turbulence modeling (Bechara et al., 1994; Smirnov et al., 2001). The sub-grid closures for the three-dimensional and the reduced models are verified using the test cases of acoustic cavitation of a single bubble and a bubble screen, and a bubble cloud, respectively.

Finally, the methods are used to simulate a challenging case of cloud cavitation excited in a strong ultrasound wave. The structure of the bubble cloud obtained in the simulation is confirmed to qualitatively agree with a bubble cloud observed in high-speed images, that was excited by a focused ultrasound generated by a medical transducer. The chapter proceeds as follows. In § 3.2, we introduce volume-averaged equations of motion. Then we describe the discretization and spatial integration of the governing equations on a three-dimensional Cartesian grid and regularization of the volume of bubbles using a kernel. Subsequently we describe the dynamical equations of the radial oscillations of bubbles as a closure. In § 3.3, we describe the reduction of the governing equations on two-dimensional and axi-symmetric coordinates and introduce regularization kernels for the grids. In § 3.4, we present numerical tests of single bubble and cloud cavitation for verifications of the methods. Finally, in § 4.7, we state a chapter summary.

3.2 Governing equations

Volume averaged equations of motion

We introduce volume-averaged equations of motion to describe the dynamics of a mixture of dispersed bubbles and a compressible liquid in three-dimensional space. Volume-averaged equations consider the conservation of mass, momentum, and energy of the mixture as a continuum media that are defined by applying the volume averaging operator $\overline{(\cdot)}$ to a control volume of the mixture: $\overline{(\cdot)} = (1-\beta)(\cdot)_l + \beta(\cdot)_g$, where $\beta \in [0, 1)$ is the volume fraction of gas (void fraction), and subscripts l and g denote the liquid and gas phase, respectively. We start by writing the equations in a conservative form:

$$\frac{\partial \overline{\rho}}{\partial t} + \nabla \cdot (\overline{\rho \boldsymbol{u}}) = 0, \tag{3.1}$$

$$\frac{\partial (\overline{\rho \boldsymbol{u}})}{\partial t} + \nabla \cdot (\overline{\rho \boldsymbol{u}} \otimes \overline{\boldsymbol{u}} + p\mathcal{I} - \mathcal{T}) = 0, \tag{3.2}$$

$$\frac{\partial \overline{E}}{\partial t} + \nabla \cdot \left((\overline{E} + p)\overline{\boldsymbol{u}} - \mathcal{T} \cdot \overline{\boldsymbol{u}}\right) = 0, \tag{3.3}$$

where ρ is the density, $\boldsymbol{u} = (u, v, w)^{\mathrm{T}}$ is the velocity, p is the pressure and E is the total energy, respectively. $\mathcal{T}$ is the effective viscous stress tensor of the mixture. We invoke two approximations widely used in averaged models at the limit of low void fraction, up to $O(10^{-2})$ (Caflisch et al., 1985; Commander and Prosperetti, 1989; Fuster and Colonius, 2011). First, the density of liquid is typically much larger than that of gas, $\rho_l \gg \rho_g$, and thus the density of the mixture is approximated by that of the liquid:

$$\overline{\rho} = (1-\beta)\rho_l + \beta\rho_g \approx (1-\beta)\rho_l. \tag{3.4}$$

This approximation is clearly valid for the mixture of water and air/vapor bubbles under practical conditions. Second, the slip velocity between the two phases is zero:

$$\overline{\boldsymbol{u}} \approx \boldsymbol{u}_l = \boldsymbol{u}_g. \tag{3.5}$$

With the assumption of zero slip-velocity, the momentum flux across the gas-liquid interface is effectively zero, and therefore, we approximate the total viscous stress as that in the continuous phase:

$$\mathcal{T} \approx \mathcal{T}_l. \tag{3.6}$$

$\mathcal{T}_l$ is the viscous stress tensor of pure Newtonian liquid:

$$\mathcal{T}_l = 2\mu \left(\mathcal{D}_l - \frac{1}{3}(\nabla \cdot \boldsymbol{u}_l)\mathcal{I} \right), \tag{3.7}$$

where μ_l is the shear viscosity of liquid and $\mathcal{D}_l$ is the deformation rate tensor:

$$\mathcal{D}_l = \frac{1}{2}(\boldsymbol{u}_l + \boldsymbol{u}_l^{\mathrm{T}}). \tag{3.8}$$

In reality, spherical bubbles experience hydrodynamic forces from the surrounding liquid (Magnaudet and Legendre, 1998), and the resulting slip velocity can be non-zero. The momentum flux across the gas-liquid interface can contribute to the effective viscosity of the mixture (Zhang and Prosperetti, 1994). Such modeling is not a focus of the present study, though one could extend the present formulation to include the effect of the non-zero slip velocity on $\mathcal{T}$. Nevertheless, for many practical problems of cavitation, the time scale of the radial oscillations of bubbles are estimated to be much shorter than that of the translational motions, and therefore, assumption of the zero-slip velocity is a reasonable first approximation (Caflisch et al., 1985).

Using relations (3.4-3.6), equations (3.1-3.3) can be rewritten as conservation equations in terms of the mass, momentum, and energy of the liquid with source terms, as an inhomogeneous hyperbolic system:

$$\frac{\partial \rho_l}{\partial t} + \nabla \cdot (\rho_l \boldsymbol{u}_l) = \frac{\rho_l}{1-\beta}\left[\frac{\partial \beta}{\partial t} + \boldsymbol{u}_l \cdot \nabla \beta\right], \tag{3.9}$$

$$\frac{\partial (\rho_l \boldsymbol{u}_l)}{\partial t} + \nabla \cdot (\rho_l \boldsymbol{u}_l \otimes \boldsymbol{u}_l + p\mathcal{I} - \mathcal{T}_l) = \frac{\rho_l \boldsymbol{u}}{1-\beta}\left[\frac{\partial \beta}{\partial t} + \boldsymbol{u}_l \cdot \nabla \beta\right] - \frac{\beta \nabla \cdot (p\mathcal{I} - \mathcal{T}_l)}{1-\beta}, \tag{3.10}$$

$$\frac{\partial E_l}{\partial t} + \nabla \cdot ((E_l + p)\boldsymbol{u}_l - \mathcal{T}_l \cdot \boldsymbol{u}_l) = \frac{E_l}{1-\beta}\left[\frac{\partial \beta}{\partial t} + \boldsymbol{u}_l \cdot \nabla \beta\right] - \frac{\beta \nabla \cdot (p\boldsymbol{u}_l - \mathcal{T}_l \cdot \boldsymbol{u}_l)}{1-\beta}. \tag{3.11}$$

This form of equations is particularly convenient since we can directly apply the finite volume WENO scheme for spatial integration of the equations, which will be discussed in the following section. For later convenience, we also denote the equations in a vector form:

$$\frac{\partial \boldsymbol{q}_l}{\partial t} + \nabla \cdot \boldsymbol{f}(\boldsymbol{q}_l) = \boldsymbol{g}(\boldsymbol{q}_l, \beta, \dot{\beta}), \tag{3.12}$$

where $\boldsymbol{q}_l = [\rho_l, \rho_l \boldsymbol{u}_l, E_l]$ and

$$\boldsymbol{g} = \frac{1}{1-\beta}\frac{d\beta}{dt}\boldsymbol{q}_l - \frac{\beta}{1-\beta}\nabla \cdot (\boldsymbol{f} - \boldsymbol{u}_l \boldsymbol{q}_l). \tag{3.13}$$

For a thermodynamic closure for the liquid, we employ stiffened gas equation of state:

$$p = (\gamma - 1)\rho\varepsilon - \gamma\pi_\infty, \tag{3.14}$$

where ε is the internal energy of liquid, γ is the specific heat ratio, and π_∞ is the stiffness, respectively. In the present study we use $(\gamma, \pi_\infty) = (7.1, 3.0610^8)$ for water, where the unit of π_∞ is Pa. At the limit of small change in the density of liquid, the equation of state can be linearized as

$$p = p_0 + c_0^2(\rho - \rho_0), \tag{3.15}$$

where

$$c = \sqrt{\gamma(p + \pi_\infty)/\rho} \tag{3.16}$$

is the speed of sound in liquid and the subscript 0 denotes reference states.

Spatial discretization

In the following we describe a method of numerical representation of the governing equation in $x - y - z$ 3D Cartesian coordinate. We spatially discretize equation (3.12):

$$\frac{\partial \boldsymbol{q}_l}{\partial t} + \frac{\partial \boldsymbol{f}^x(\boldsymbol{q}_l)}{\partial x} + \frac{\partial \boldsymbol{f}^y(\boldsymbol{q}_l)}{\partial y} + \frac{\partial \boldsymbol{f}^z(\boldsymbol{q}_l)}{\partial z} = \boldsymbol{g}, \tag{3.17}$$

where $\boldsymbol{f}^x$, $\boldsymbol{f}^y$, and $\boldsymbol{f}^z$ are vectors of fluxes in x, y, and z directions. We integrate the above equation in arbitrary finite volume grid cell

$$I_{i,j,k} = [x_{i-1/2}, x_{i+1/2}] \times [y_{j-1/2}, y_{j+1/2}] \times [z_{k-1/2}, z_{k+1/2}], \tag{3.18}$$

where i, j, and k are the indices in $x-$, $y-$ and $z-$ directions, and $x_{i\pm1/2}$, $y_{j\pm1/2}$, and $z_{k\pm1/2}$ are the positions of cell faces. At each finite volume cell, we express the equation in the following semi-discrete form:

$$\begin{aligned}\frac{d\boldsymbol{q}_{l,i,j,k}}{dt} = \frac{1}{\Delta x_i}[\boldsymbol{f}^x_{i-1/2,j,k} - \boldsymbol{f}^x_{i+1/2,j,k}] + \frac{1}{\Delta y_j}[\boldsymbol{f}^y_{i,j-1/2,k} - \boldsymbol{f}^y_{i,j+1/2,k}] \\ + \frac{1}{\Delta z_j}[\boldsymbol{f}^z_{i,j,k-1/2} - \boldsymbol{f}^z_{i,j,k+1/2}] + \boldsymbol{g}_{i,j,k}.\end{aligned} \tag{3.19}$$

The conservative variables at cell faces are reconstructed by a high-order WENO scheme from cell-centered values, then are used in HLLC Riemann solver to calculate the fluxes. In the present study we employ fifth-order WENO scheme (WENO5) introduced by Coralic and Colonius (Coralic and Colonius, 2014), unless otherwise noted. High-order WENO schemes are, in general, robust in capturing discontinuities including shock wave and material's interface, while capable of resolving continuous waves with a high-amplitude with relatively small numerical dissipation/dispersion (Titarev and E. Toro, 2004; Pirozzoli, 2006; Shu, 2016). Such properties of WENO schemes are suitable for simulations of cloud cavitation in the regime of the interest of the present study; a passage of strong pressure waves causes violent, nonlinear oscillations of bubbles, each of which emits strong pressure waves with broadband frequency and generates complex structures of pressure fields by mutual interactions.

Void fraction

We express $\boldsymbol{g}$, β and $\dot{\beta}$ as functions of the state of the bubbles. To do so, we employ a Lagrangian point-bubble approach, in that the gas phase is modeled as spherical, radially oscillating cavities consisted of a non-condensible gas and liquid vapor. The center of nth bubble ($n \in \mathbb{Z} : n \in [1, N]$), with a radius of R_n and a radial velocity of $\dot{R}_n$, is initially defined at the coordinate $\boldsymbol{x}_n$ and tracked as Lagrangian points during simulations. To define the continuous field of the void fraction in the mixture at coordinate $\boldsymbol{x}$, we smear the volume of bubble using a regularization kernel δ:

$$\beta(\boldsymbol{x}) = \sum_{n=1}^{N} V_n(R_n)\delta(d_n, h), \tag{3.20}$$

where V_n is the volume of bubble n, $V_n = 4/3\pi R_n^3$, and d_n is the distance of the coordinate $\boldsymbol{x}$ from the center of the bubble, $d_n = |\boldsymbol{x} - \boldsymbol{x}_n|$. Various types of kernels are used to regularize Lagrangian variables in particle methods and immersed boundary methods (Cottet and Koumoutsakos, 2000; Peskin, 2002; Monaghan, 2005), and have also been applied to dispersed bubbly-mixture (Kitagawa et al., 2001; Fuster and Colonius, 2011; Jingsen et al., 2018). In the present study, we use the continuous, second order, truncated Gaussian function for the kernel:

$$\delta(d_n, h) = \begin{cases} \frac{1}{h^3(2\pi)^{3/2}} e^{-\frac{d_n^2}{2h^2}}, & 0 \le \frac{d_n}{h} < 3 \\ 0 & 3 \le \frac{d_n}{h}, \end{cases} \tag{3.21}$$

where h is the width of the support of the kernel. Likewise,

$$\frac{\partial \beta(\boldsymbol{x})}{\partial t} = \frac{\partial}{\partial t} \sum_{n=1}^{N} V_n \delta = \sum_{n=1}^{N} \frac{\partial V_n}{\partial t} \delta + \sum_{n=1}^{N} V_n \frac{\partial \delta}{\partial t}, \tag{3.22}$$

where

$$\frac{\partial V_n}{\partial t} = 4\pi R_n^2 \dot{R}_n, \quad \frac{\partial \delta}{\partial t} = -\boldsymbol{u}_l \cdot \nabla \delta. \tag{3.23}$$

In the discretized field, we are regularizing the discontinuous distribution of the volume of a bubble defined at a singular point in a finite volume cell, by distributing the void fraction within neighboring cells around the bubble (figure 3.1 (a)).

Bubble dynamics

We model the dynamics of volumetric oscillations of the bubbles forced by pressure fluctuations in the surrounding liquid. When the time scale of the evolution of the pressure in the mixture is sufficiently mild and slow, compared to the characteristic frequency of bubbles, the change of the states of the gas inside the bubble can be assumed as being quasi-static. Meanwhile, in the problems we aim to simulate, bubbles oscillate in response to rapid and high-amplitude changes in the pressure with a high amplitude. In turn, the bubble oscillations generate and scatter pressure waves into the surrounding liquid. Moreover, mass-transfer due to phase change as well as heat transfer at the bubble wall can damp the volumetric oscillations. To model bubble oscillations, we employ the Keller-Miksis equation, combined with a reduced-order model introduced by Preston et al. (2007) for the heat and mass-transfer. In the model, the states of the vapor-gas mixture are treated as being uniform in the bubble. The Keller-Miksis equation is a second order, nonlinear ODE in terms of the radius of a single, isolated bubble in an unbounded, weakly compressible liquid:

$$\left(R_n\left(1-\frac{\dot{R}_n}{c}\right)\right)\ddot{R}_n+\frac{3}{2}\dot{R}^2\left(1-\frac{\dot{R}_n}{3c}\right)=\frac{p_n-p_\infty}{\rho}\left(1+\frac{\dot{R}_n}{c}\right)+\frac{R_n\dot{p}_n}{\rho c}, \tag{3.24}$$

$$p_n=p_{Bn}-\frac{4\mu_l\dot{R}_n}{R_n}-\frac{2\sigma}{R_n}, \tag{3.25}$$

where p_n is the pressure at the bubble wall, p_{Bn} is the pressure inside the bubble, σ is the surface tension, and p_∞ is the component of the pressure that forces the radial oscillations of the bubble. The reduced-order model formulates $\dot{p}_n$ and the vapor mass in the bubble $\dot{m}_{Vn}$ as

$$\dot{p}_{Bn}=\mathsf{func}[R_n,\dot{R}_n,m_{Vn}] \tag{3.26}$$

$$\dot{m}_{Vn}=\mathsf{func}[R_n,m_{Vn}]. \tag{3.27}$$

For the explicit forms of equations (3.26) and (3.27) as well as further details and validation/verification of the model, see Preston et al. (2007). Overall, equations (3.24-3.27) consist a system of ODEs in terms of $[R_n,\dot{R}_n,p_{Bn},m_{Vn}]$, that can be integrated given initial conditions and p_∞. We will discuss the treatment of p_∞ in the next section. In principle, other variations of the Rayleigh-Plesset equation as well as models of heat and mass-transfer could be used to express the sub-grid bubble dynamics.

Modeling p_∞: bubble dynamic closure

We now introduce a closure to model p_∞. The Keller-Miksis equation models the pressure field surrounding a single, isolated, spherically symmetric bubble (Keller and Miksis, 1980). p_∞ represents an incoming acoustic wave that drives the oscillations. The pressure wave scattered by the bubble is also represented by a spherical outgoing wave, p_{out}. The pressure field, as a solution of the Keller-Miksis equation, is thus the superposition of p_∞ and p_{out}. In a bubble cloud, p_∞

for each bubble is the superposition of p_{out} emitted by the surrounding bubbles and the pressure wave that propagate from outside the cloud, and in general not know a-priori. Following Fuster and Colonius (hereafter denoted as FC) (Fuster and Colonius, 2011), we obtain p_∞ for each sub-grid bubble by modeling the pressure field in a finite volume cell that encloses the bubble. The pressure of the cell (or group of cells) is given by the spatial average of the superposition of p_∞ and p_{out} emitted by the sub-grid bubble:

$$p_{cell} = \frac{1}{V_{l,cell}} \int_{V_{cell}} (p_\infty + p_{out}) dv_l \approx p_\infty + \frac{1}{V_{l,cell}} \int_{V_{cell}} p_{out} dv_l, \tag{3.28}$$

where $V_{l,cell}$ is the volume of the liquid in the control volume V_{cell} and dv_l is the volume element of the liquid, respectively. A natural choice of V_{cell} is the region of the liquid over which the volume of bubble is smeared over. [1] We can assume that

$$\frac{1}{V_{l,cell}} \int_{V_{cell}} p_\infty dv_l \approx p_\infty, \tag{3.29}$$

since p_∞ is approximately uniform at a scale of the cell: $\Delta \ll \lambda$, where λ is the characteristic wave length of the pressure wave. Meanwhile, in the discretized field, p_{cell} can be directly approximated as

$$p_{cell,i,j,k} \approx \frac{\sum_{i-N_r}^{i+N_r} \sum_{j-N_r}^{j+N_r} \sum_{k-N_r}^{k+N_r} (1-\beta_{m,n,p}) p_{m,n,p} V_{m,n,p}}{\sum_{i-N_r}^{i+N_r} \sum_{j-N_r}^{j+N_r} \sum_{k-N_r}^{k+N_r} (1-\beta_{m,n,p}) V_{m,n,p}}, \tag{3.30}$$

where $V_{i,j,k}$ is the volume of cell $I_{i,j,k}$. $\frac{1}{V_{l,cell}} \int p_{out} dv_l$ can be modeled using the dynamical states of the bubble and p_{cell}:

$$\frac{1}{V_{l,cell}} \int_{V_{cell}} p_{out} dv_l \approx \frac{1}{1-C_1} \left[p_{cell} - p_n - \left(C_2 - \frac{1}{2} \right) \rho \dot{R}_n^2 \right], \tag{3.31}$$

where C_1 and C_2 are functions of R_n and $V_{l,cell}$. We can spatially discretize this expression to represent p_{out} at each computational cell that contains a bubble, and substitute into relation (3.28), along with (3.30), to obtain p_∞. As discussed by FC, p_{out} spatially decay with r, where r is the distance from the center of the bubble. When V_{cell} is much larger than the volume of the bubble, the contribution of p_{out} to

---

[1] For a bubble located in a cell $I_{m,n,p}$, we define that the cells over which the volume of the bubble is smeared as $I_{i,j,k} : i \in [m - N_r, m + N_r], j \in [n - N_r, n + N_r], k \in [p - N_r, p + N_r]$, where $N_r = \lfloor 3h/\Delta \rfloor$.

p_{cell} is negligible and $p_{cell} \approx p_\infty$ holds. We note the detailed derivation of relation (3.31) in Appendix C.

Length scales of parameters

The present method is designed to correctly capture the small-scale dynamics of cloud cavitation when the following inequalities are satisfied:

$$\left.\begin{cases} R_b \\ \Delta \end{cases}\right\} \leq h < L_b, \tag{3.32}$$

where R_b is the characteristic bubble radius, Δ is the characteristic Eulerian grid size and L_b is the characteristic inter-bubble distance. With the range of parameters satisfying (3.32), we naturally have at most single bubble within each cell. The inequality between β and h comes from the upper bound of β: $\beta < 1$.

$$\max(\beta_{i,j,k}) \sim V_b \max(\delta) \sim \frac{\max(R_b)^3}{h^3}. \tag{3.33}$$

Therefore

$$\max(\beta_{i,j,k}) < 1 \longrightarrow \max(R_b) < h. \tag{3.34}$$

Meanwhile, the value of $\max(R_b)$ is not known a-priori, and inequality (3.34) may not be not guaranteed to hold for the initially given h. In that case, one may dynamically increase h to satisfy the inequality during the simulation. The inequality between Δ and h is a necessary condition for the correct representation of the regularization kernel on the grid (Cottet and Koumoutsakos, 2000). The inequality between h and L_b prevents overlap among the kernel support. The minimum resolved length scale of waves emitted by the source is h; spatial scales finer than h are smeared by the kernel. Therefore when the smeared regions of neighboring bubbles overlap with each other, the pressure field of a scale as small as inter-bubble distance is likewise filtered. In that case, as partially discussed by FC, the model tends to recover solutions of classical ensemble averaged equations, in that the smallest length scale in the field becomes the wavelength of the pressure waves that propagate in the averaged bubbly-mixture. The present method is designed to capture the small scales, and thus the support width is set shorter than the characteristic inter-bubble distance. Note that R_b can be admissibly larger than Δ (which means that the bubble size can be larger than the grid size) as long as (3.34) is satisfied. Similar arguments may hold when different forms of kernel function are used.

Temporal integration

For temporal integrations of solutions, we employ 4th/5th order Runge–Kutta-Cash-Karp (RKCK) algorithm (Cash and Karp, 1990). The stability of the temporal integration of Eulerian variables is dictated by the Courant-Friedrichs-Lewy (CFL) number, C, and the diffusion number, D (CFL conditions). The Keller-Miksis equation is a stiff ODE, and in a certain interval of integration it requires a time step size much smaller than that required by the CFL conditions. In the problems shown in the present study, we initially set a fixed time step size that satisfies the CFL condition to satisfy $C < 0.3$ and $D < 0.15$. At each time step, we integrate Eulerian variables using the 4th order scheme built in the algorithm. Lagrangian variables are updated using the 4th and 5th order schemes with the same time step size, then the errors between the two solutions are calculated. If the errors are smaller than a tolerance, the algorithm employs the 5th order solution, while if not, both Eulerian/Lagrangian variables are re-calculated with a smaller value of time step size. We repeat this process until the error becomes smaller than the tolerance.

Acoustic source

In simulations we excite volumetric oscillations of bubbles using various amplitudes of traveling pressure waves. In order to generate the waves, we utilize a source-term approach introduced in Chapter 2.

3.3 Model reduction of the three-dimensional volume-averaged equations

In many problems, cloud cavitation occurs in statistically two-dimensional (e.g. flows over a two-dimensional body), or axi-symmetric (e.g. ellipsoidal/spherical bubble cloud) configurations, in the sense that the flow field and the spatial distribution of bubbles are homogeneous in certain directions. To simulate the bubbly-mixture in such configurations with lower computational expense, we derive a reduced model by spatially averaging the three-dimensional volume-averaged equations along the direction of symmetry, and then discretize the continuous phase on a two-dimensional/axi-symmetric grid. In order to properly map the three-dimensional distribution of bubbles onto the void fraction defined in such grid cells, we will introduce modified regularization kernels. p_∞ is recovered by modeling pressure fluctuations at the sub-grid scale as locally isotropic, stochastic noise.

The speed-up of simulations achieved by using the reduced models is discussed in Appendix B.

Two-dimensional volume averaged equations

We consider the flow field defined on Cartesian coordinates. We assume that the flow field and the spatial distribution of bubbles are homogeneous along the z-axis. We define the line-averaging operator T_z as

$$T_z(\cdot) = \frac{1}{L}\int_{-L/2}^{L/2} (\cdot) dz, \tag{3.35}$$

where L is the scale of homogeneity. In order to obtain two-dimensional equations, we apply T_z to the three-dimensional volume-averaged equations:

$$T_z\left[\frac{\partial \boldsymbol{q}_l}{\partial t} + \nabla \cdot \boldsymbol{f}(\boldsymbol{q}_l)\right] = T_z \boldsymbol{g}(\boldsymbol{q}_l, \beta, \dot{\beta}). \tag{3.36}$$

Due to the homogeneity of the flow field along the z-axis, z component of equation (3.36) is projected onto the nullspace of T_z. $T_z \partial \boldsymbol{q}_l / \partial t = \partial(T_z \boldsymbol{q}_l)/\partial t$, while $T_z \nabla \cdot \boldsymbol{f}(\boldsymbol{q}_l) \neq \nabla \cdot \boldsymbol{f}(T_z \boldsymbol{q}_l)$ and $T_z \boldsymbol{g}(\boldsymbol{q}_l, \beta, \dot{\beta}) \neq \boldsymbol{g}(T_z \boldsymbol{q}_l, T_z\beta, T_z\dot{\beta})$, since $\boldsymbol{f}$ and $\boldsymbol{g}$ are nonlinear functions of $\boldsymbol{q}_l$, β and/or $\dot{\beta}$. We decompose $T_z \nabla \cdot \boldsymbol{f}$ and $T_z \boldsymbol{g}$ into linear and nonlinear components:

$$T_z \nabla \cdot \boldsymbol{f}(\boldsymbol{q}_l) = \nabla \cdot \boldsymbol{f}(T_z \boldsymbol{q}_l) + \nabla \cdot \boldsymbol{f}_{res}, \tag{3.37}$$

$$T_z \boldsymbol{g}(\boldsymbol{q}_l, \beta, \dot{\beta}) = \boldsymbol{g}(T_z \boldsymbol{q}_l, T_z\beta, T_z\dot{\beta}) + \boldsymbol{g}_{res}, \tag{3.38}$$

where $\boldsymbol{f}_{res}$ and $\boldsymbol{g}_{res}$ are residuals defined by these equations. By substituting these expressions, equation (3.36) becomes

$$\frac{\partial (T_z \boldsymbol{q}_l)}{\partial t} + \nabla \cdot \boldsymbol{f}(T_z \boldsymbol{q}_l) = \boldsymbol{g}(T_z\beta, T_z \boldsymbol{q}_l) - \nabla \cdot \boldsymbol{f}_{res} + \boldsymbol{g}_{res} \tag{3.39}$$

$$\approx \boldsymbol{g}(T_z\beta, T_z \boldsymbol{q}_l) + \boldsymbol{g}_{res}, \tag{3.40}$$

where we applied $|\nabla \cdot \boldsymbol{f}_{res}| \ll |\nabla \cdot \boldsymbol{f}(T_z \boldsymbol{q}_l)|$, assuming that the back-ground flow field is uniform at the scale of homogeneity, L. In order to close the equations, $\boldsymbol{g}_{res}$

needs to be modeled. To do so, we decompose p and β into their spatial mean and fluctuation in the z direction:

$$p = T_z p + p' \tag{3.41}$$

$$\beta = T_z \beta + \beta', \tag{3.42}$$

where the prime denotes fluctuations. Note that $T_z(\cdot)' = 0$.

By substituting these expressions and neglecting terms higher than 2nd order, $T_z \boldsymbol{g}$ can be expressed as:

$$T_z \boldsymbol{g}_z(\boldsymbol{q}_l, \beta, \dot{\beta}) = T_z \left(\frac{1}{1-\beta} \frac{d\beta}{dt} \boldsymbol{q}_l \right) - T_z \left(\frac{\beta}{1-\beta} \nabla \cdot (\boldsymbol{f} - \boldsymbol{u}_l \boldsymbol{q}_l) \right) \tag{3.43}$$

$$\approx \boldsymbol{g}_z(T_z \boldsymbol{q}_l, T_z \beta, T_z \dot{\beta}) + T_z \left(\beta' \frac{d\beta'}{dt} \right) + (2 T_z \beta + 1) T_z (\beta' \nabla \cdot (\boldsymbol{f} - \boldsymbol{u}_l \boldsymbol{q}_l)'), \tag{3.44}$$

where $\nabla \cdot (\boldsymbol{f} - \boldsymbol{u}_l \boldsymbol{q}_l)' \approx [0, \nabla p', (T_z \boldsymbol{u}_l) \cdot \nabla p']^{\mathrm{T}}$. Therefore it is sufficient to model p', β' and $\dot{\beta}'$ to express $\boldsymbol{g}_{res}$.

Regularization kernel for 2D Cartesian grid

In order to compute $\beta' = \beta - T_z \beta$ and $\partial \beta' / \partial t = \partial \beta / \partial t - T_z (\partial \beta' / \partial t)$, we express

$$T_z \beta(x, y) = \frac{1}{L} \int_{-L/2}^{L/2} \beta(x, y, z) dz \tag{3.45}$$

$$= \frac{1}{L} \int_{-L/2}^{L/2} \sum_{N}^{P} V_n \delta dz \tag{3.46}$$

$$= \sum_{N}^{P} V_n \left[\frac{1}{L} \int_{-L/2}^{L/2} \delta dz \right] \tag{3.47}$$

$$= \sum_{N}^{P} V_n \delta_{2D}, \tag{3.48}$$

and

$$T_z \frac{d\beta}{dt} = \sum_{N}^{P} \frac{d}{dt} \left[V_n \delta_{2D} \right], \tag{3.49}$$

where we defined

$$\delta_{2D} = \frac{1}{L}\int_{-L/2}^{L/2} \delta dz. \tag{3.50}$$

δ_{2D} can be interpreted as a regularization kernel that maps the volume of bubbles distributed in three-dimensional space onto two-dimensional space spanned by x-y coordinates basis vectors.

In a geometric interpretation, we are essentially solving for the volume averaged equations with $u_z = 0$, on finite volume grid cells in a shape of parallelepiped with a span of L along the z-axis (figure 3.1 (b)). The Eulerian variables are treated as being uniform in each parallelepiped cell. However, the physical distributions of the bubbles are three-dimensional and non-uniform in the z direction. To correct the discrepancy, we are modeling the quadratic, nonlinear terms in terms of β and $\dot{\beta}$, which appear in $\boldsymbol{g}_{res}$. In order to numerically represent δ_{2D} at each parallelepiped cell, we discretize the parallelepiped cell into smaller n_p cells in z-direction, and apply a mid-point rule to the integral:

$$\delta_{2D_{i,j}} \approx \frac{1}{L}\sum_{k=1}^{n_p} \Delta z_k \delta(d_n(\boldsymbol{x}_n, \boldsymbol{x}_{i,j,k}), h). \tag{3.51}$$

Note that the small cells are essentially identical to those defined on 3D Cartesian grids, $I_{i,j,k}$. The total contribution of the volume of bubble n on $\beta_{2D_{i,j}}$ is represented by an overlapping region of $I_{i,j}$ and the ball within that V_n is smeared over (figure 3.1 (b)).

Modeling p_∞ on the reduced space: stochastic closure

As discussed in section (3.2), p_∞ needs to be recovered from $p_{cell} = T_z p_{cell} + p'_{cell}$ to correctly force the Lagrangian bubbles. The first term can be approximated as $T_z p_{cell}$:

$$T_z p_{cell} = T_z \frac{1}{V_{cell}}\int_{V_{cell}} (p_\infty + p_{out}) dv_l \approx T_z p_\infty + T_z \int_{V_{cell}} p_{out} dv_l \approx T_z p_\infty. \tag{3.52}$$

Note that the contribution of p_{out} is negligible compared to p_∞ since $V_{cell} \gg V_n$. We are missing p'_{cell} and not able to recover it from the sub-grid dynamics, unlike

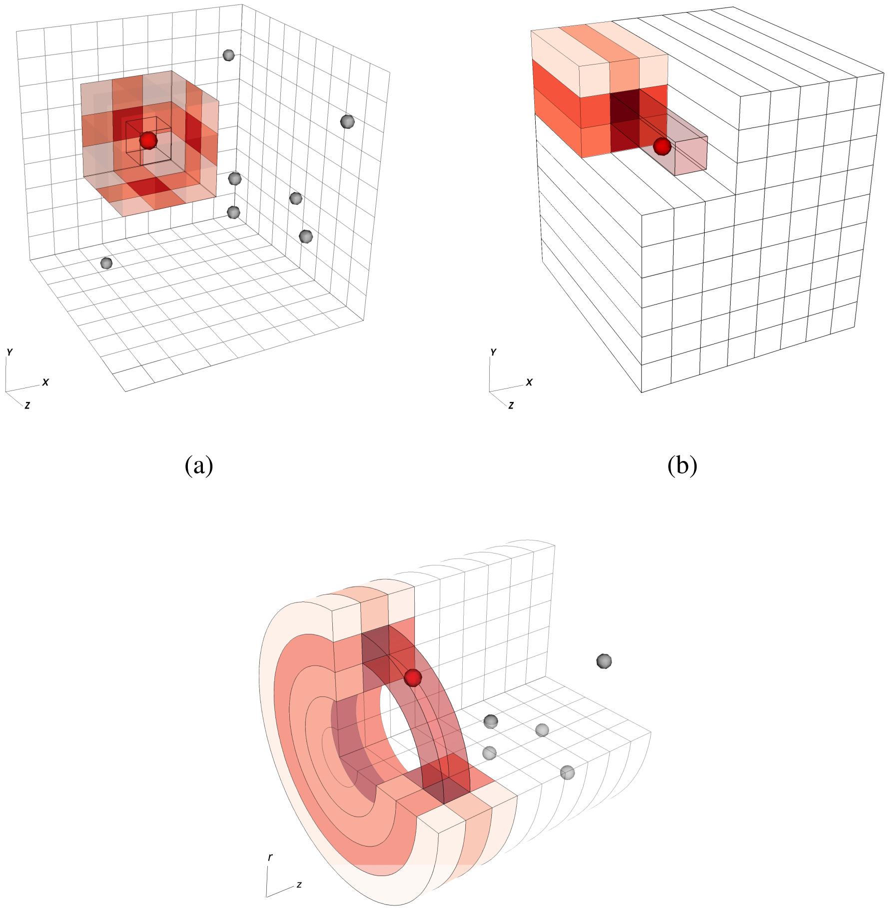

(a)

(b)

(c)

Figure 3.1: Schematic of the smearing of the volume of Lagrangian bubbles on neighboring finite volume cells defined on various grids in the same domain: (a) three dimensional Cartesian grid; (b) two dimensional Cartesian grid; (c) axi-symmetric grid. On each grid, for the same bubble (red-colored), we are shading the cell that contains the bubble and those neighboring to it, on which the volume of bubble is smeared over as the void fraction. Depth of the shade indicates the value of the void fraction, which decays with the distance from the bubble. It is apparent that, depending on the choice of grids, the volume is mapped onto different regions in the domain.

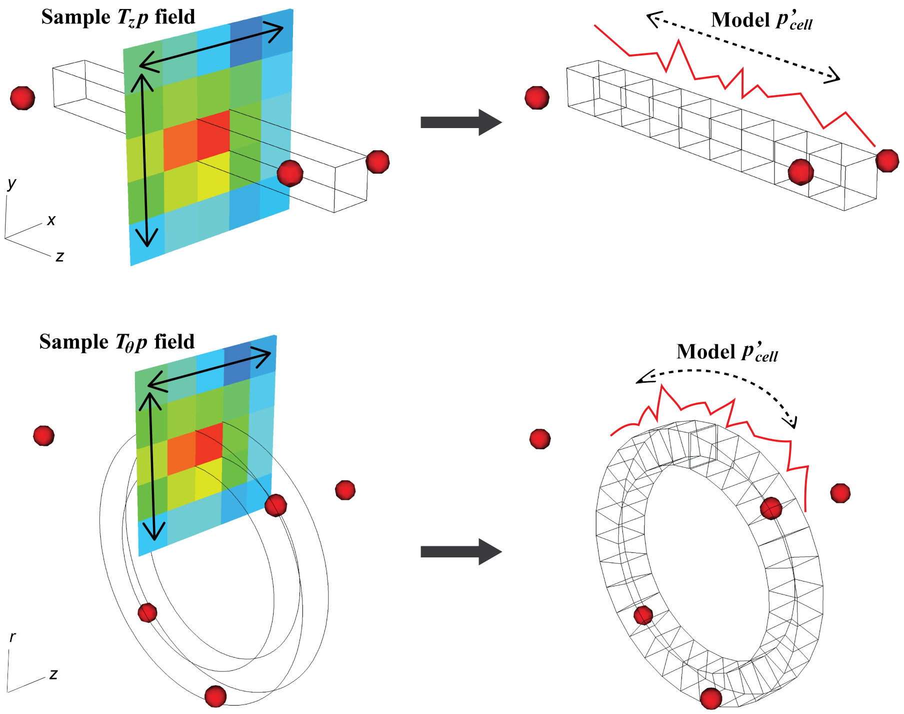

Figure 3.2: Schematic of the technique to estimate p'_{cell} in the reduced models (top: two-dimensional, bottom: axi-symmetric).

the closure for the three-dimensional model. Therefore we introduce an alternative method to estimate p'_{cell}.

From the far-field, bubbles can be seen as acoustic point sources isotropically distributed in space. In classical scattering theory, pressure fluctuations resulting from such sources are modeled as a stochastic noise (Ishimaru, 1978; Fouque et al., 2007). Following the theory, we model p'_{cell} as white noise that is locally, spatially isotropic. In that case, p'_{cell} is characterized by its (zero) mean and variance. In the discretized field, we have the following relation between $E[p'^2_{cell}]$ and $E[(T_z p_{cell})'^2]$:

$$E[(T_z p_{cell})'^2]_{i,j} \approx \frac{1}{C_T} E[p'^2_{cell}]_{i,j}, \tag{3.53}$$

where $C_T = n_p/(2N_r + 1)$.[2] This means that the variance of the original random

---

[2] When mutually independent, Gaussian white noise fields with the same variance are averaged over X times, the resulting variance of the averaged field can be approximated as $1/X$ of the variance of the original fields (e.g. Brunt et al. (2010)). The factor C_T comes from the fact that p_{cell} in each cell is obtained by volume averaging p over the surrounding $(2N_r + 1)^3$ cells, while $(T_z p_{cell})$ is obtained by averaging p over $n_p(2N_r + 1)^2$ cells on a 3D Cartesian grid. See equations (30), (48), and (52).

field is larger than that of the "averaged" random field, by a factor of $C_T > 1$. In more general cases where p'_{cell} is modeled as a colored noise, C_T can take a different value. We note that a method to obtain C_T for a field of spatially isotropic, fluctuating variables was discussed by Brunt et al. (2010), with applications to isotropic turbulence in the interstellar medium.

Our goal is to recover p'_{cell} at the location of each bubble, from the value of $T_z p_{cell}$ in a two-dimensional simulation. To that aim, we estimate $E[(T_z p_{cell_{i,j}})'^2]$ by sampling the values of $T_z p_{cell}$ in the neighboring cells:

$$E[(T_z p_{cell_{i,j}})'^2] \approx S[(T_z p_{cell_{i,j}})^2] - S[T_z p_{cell_{i,j}}]^2. \tag{3.54}$$

S is an operator that takes volume-weighted average in a window of cells:

$$S[(\cdot)_{i,j}] = \frac{\sum_{m=i-N_s}^{i+N_s} \sum_{n=j-N_s}^{j+N_s} (\cdot)_{i,j} V_{m,n}}{\sum_{m=i-N_s}^{i+N_s} \sum_{n=j-N_s}^{j+N_s} V_{m,n}}, \tag{3.55}$$

where the sampling window is given by $(2N_r + 1) \times (2N_r + 1)$. Then we can obtain $E[p'^2_{cell}]_{i,j}$ from $E[(T_z p_{cell_{i,j}})'^2]$ using relation (3.53).

Rigorous approaches to integrating PDE with stochastic source term (Langevin equation) are available (Delong et al., 2013). Yet, compatibility of such approaches with the other components of the present method, such as the high-order WENO scheme and the stiff dynamics of bubbles, is not guaranteed, and is beyond a focus of the present study. We therefore solve a deterministic equation by modeling the source as a (smooth) sum of Fourier components with randomized phase (Bechara et al., 1994). Following the method, we express p' as:

$$p'_{i,j}(z,t) = \int A(k) \mathrm{e}^{i(kz - \omega t + \phi_k)} dk, \tag{3.56}$$

where k is the wave number, $\omega = kc$ is the angular frequency, A is the amplitude, and $\phi_k \in [0, 2\pi]$ is the random phase associated with k, given a priori. In the present study, we use a Gaussian spectral power distribution in terms of the wavelength $\lambda = 2\pi/k$:

$$A^2(\lambda) = \frac{C_A}{\sigma_\lambda \sqrt{2\pi}} e^{-\frac{(\lambda - \lambda_c)^2}{2\sigma_\lambda^2}}, \tag{3.57}$$

where C_A is a normalization constant that satisfies

$$\int A^2(k)dk = E[p'^2_{cell}]_{i,j}. \tag{3.58}$$

Given the physical assumption that a dominant structural length scale of p', and thus the pressure fluctuation inside the parallelepiped cell that contains multiple bubbles, corresponds to the mean inter-bubble distance, we take $\lambda_c = 1/n_b^{1/3}$, where n_b is the local density of the bubble, and $\sigma_\lambda = \lambda_c/2$. For numerical representation, we express p'_{cell} as

$$p'_{cell,i,j}(z,t) \approx \sum_{i=1}^{N_\phi} \tilde{A}(k_i)\cos(k_i z - \omega t + \phi_{k_i})\Delta k_i.^3 \tag{3.59}$$

$N_\phi = 100$ and uniform $\Delta k : \Delta k = k_{max}/N_\phi = \pi/N_\phi\Delta$ give a satisfactory result. ϕ_{k_i} is randomly calculated with $E[\phi_{k_i}] = \pi/2$.

Axi-symmetric volume averaged equations

To model axi-symmetric flows, we define an azimuthal averaging operator T_θ:

$$T_\theta(\cdot) = \frac{1}{2\pi r}\int_0^{2\pi}(\cdot)r d\theta. \tag{3.60}$$

Following the two-dimensional case, we apply T_θ to three-dimensional volume averaged equations:

$$\frac{\partial(T_\theta \boldsymbol{q}_l)}{\partial t} + \nabla\cdot\boldsymbol{f}(T_\theta\boldsymbol{q}_l) = \boldsymbol{g}(T_\theta\beta, T_\theta\boldsymbol{q}_l) - \nabla\cdot\boldsymbol{f}_{res} + \boldsymbol{g}_{res}, \tag{3.61}$$

where

$$\boldsymbol{g}_{res} \approx T_\theta\left(\beta'\frac{d\beta'}{dt}\right) + (2T_\theta\beta + 1)T_\theta(\beta'\nabla\cdot(\boldsymbol{f} - \boldsymbol{u}_l\boldsymbol{q}_l)'). \tag{3.62}$$

In order to obtain β' and $\dot{\beta}'$, we define a regularization kernel that maps the volume of bubbles onto the axi-symmetric grid:

---

[3] Note that the energy given by the statistical mean $< p'p' >$ is set equal to the variance: $< p'_{cell}p'_{cell} >_{i,j} = \frac{1}{2\pi}\int_0^{2\pi} p'_{cell,i,j}p'_{cell,i,j}dk = E[p'^2_{cell}]_{i,j}$.

$$\delta_{axi} = \frac{1}{2\pi r}\int_0^{2\pi} \delta r d\theta \approx \frac{1}{2\pi}\sum_{k=1}^{n_p} \Delta\theta_k \delta(d_p(\boldsymbol{x}_p, \boldsymbol{x}_{i,j,k}), h). \tag{3.63}$$

Here $\boldsymbol{x}_{i,j,k}$ is the coordinate of the cell center of finite volume grid cell $I_{i,j,k}$ on three-dimensional cylindrical coordinate:

$$I_{i,j,k} = [z_{i-1/2}, z_{i+1/2}] \times [r_{j-1/2}, r_{j+1/2}] \times [\theta_{k-1/2}, \theta_{k+1/2}], \tag{3.64}$$

where i, j, and k are the indices in $z-$, $r-$, and $\theta-$ directions, and $z_{i\pm1/2}$, $r_{j\pm1/2}$, and $\theta_{k\pm1/2}$ are the positions of cell faces.

The total contribution of the volume of bubble n on $\beta_{axi_{i,j}}$ is represented by an overlapping region of an axi-symmetric finite volume cell $I_{i,j}$ with a shape of a cylindrical ring, and the ball within that V_n is smeared over (figure 3.1 (c)).

p' can be recovered in the same procedure as that used for two-dimensional grids.

For numerical integration of the axi-symmetric volume averaged equations, we spatially discretize equation (3.61) in the following form:

$$\frac{\partial(T_\theta \boldsymbol{q}_l)}{\partial t} + \frac{\partial \boldsymbol{f}^z(T_\theta \boldsymbol{q}_l)}{\partial z} + \frac{\partial \boldsymbol{f}^r(T_\theta \boldsymbol{q}_l)}{\partial r} = \boldsymbol{s}(T_\theta \boldsymbol{q}_l) + \boldsymbol{g}(T_\theta \beta, T_\theta \boldsymbol{q}_l) + \boldsymbol{g}_{res}, \tag{3.65}$$

where $\boldsymbol{s}$ is the geometrical source term. This formulation is convenient since we can integrate the equations on finite volume grid cells defined on two-dimensional Cartesian coordinates (E. F. Toro, 2013):

$$I_{i,j} = [z_{i-1/2}, z_{i+1/2}] \times [r_{j-1/2}, r_{j+1/2}]. \tag{3.66}$$

We note that special kernel functions similar to (3.51) and (3.63) were previously derived for smoothed particle hydrodynamics (SPH) to simulate a single phase flow with spherical or cylindrical symmetries by integrating a standard three-dimensional kernel over the direction of symmetry (Omang et al., 2006).

3.4 Numerical results

Single bubble oscillation

We verify the method on three-dimensional grids by simulating a single bubble oscillation under pressure excitation. First, we consider a bubble with an initial radius of $R_0 = 50$ μm excited by a single cycle of sinusoidal pressure wave with a frequency of $f = 150$ kHz and an amplitude of $p_a = 2.0$ atm. This problem was addressed by Fuster and Colonius (2011), hereafter denoted as FC, in order to verify the model of p_{out} expressed in equation (3.31). The purpose of the simulation here is to study the effect of WENO schemes on the radial evolution of the bubble as well as to verify the model of p_{out}, by comparing the results with the analytical solution of the Keller-Miksis equation and the result of FC. The domain is $x, y, z \in [-10, 10]$ mm. The flow field is initially ambient and quiescent. We utilize a $116 \times 116 \times 116$ non-uniform computational grid to evolve the initial condition. Approximately nonreflecting, characteristic boundary conditions are applied along the domain boundaries (Thompson, 1987). The grid size in the regions around the bubble: $x \in [-5, 5]$ mm, is uniform with $\Delta_x = \Delta_y = \Delta_z = 100$ μm. The bubble is located at the origin. A plane acoustic source is placed at $x = -1$ mm to send the pressure wave in $+x$ direction. In figure 3.3 (a) we compare the results of the present method with various orders of WENO scheme, the analytical solution, and FC. The amplitude of oscillation predicted by WENO1 is slightly lower than those of analytical solution and FC, while the higher-order methods give satisfactory results. The discrepancy from the result of FC and the improvement by using a higher order WENO can be explained by the dissipative property of WENO. FC employed a non-dissipative numerical method (Honein and Moin, 2004). Compared to such solvers, WENO-based schemes are inherently dissipative (Pirozzoli, 2006), but stable for capturing shocks and materials interfaces (Coralic and Colonius, 2014). In figure 3.3 (b) we compare the results of WENO5 with and without the model of p_{out}. With the model, the numerical solution agrees with the analytical solution, while without it, both the amplitude of the oscillation and the timing of the second rebound deviate from the analytical solution.

Next, we simulate the dynamics of a bubble with an initial radius of $R_0 = 10$ μm excited by a single cycle of a sinusoidal pressure wave with a frequency of $f = 300$ kHz and an amplitude of $p_a = 1$ atm. We use the same simulation domain, boundary conditions and acoustic source as the previous case. We track the evolution of the pressure at $[-1.0, -1.0, -1.0]$ mm during simulations that are evolved with various grid spacings in order to assess the effect of the grid size on the pressure waves scattered by the bubble. Figure 3.4 (a) shows the results using $\Delta = 100$ and 200 μm in the region of the bubble, and an analytical solution of the evolution of the bubble radius derived by solving the Keller-Miksis equation. The pressure evolution is captured well, even with the grid size much larger than the

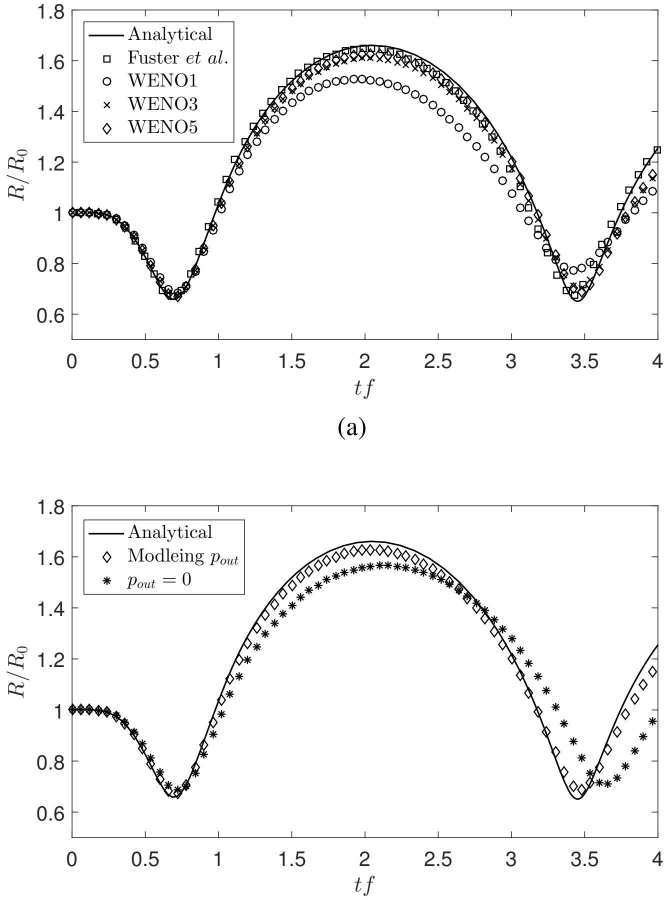

(a)

(b)

Figure 3.3: Evolution of a single, isolated bubble with an initial radius of 50 μm under excitation by a single cycle of a sinusoidal pressure wave with a frequency of 150 kHz and an amplitude of 2 atm, as a function of the non-dimensional time tf. (a) Results of FC and the present study using various orders of WENO are compared. (b) Results using WENO5 with and without modeling p_{out} are compared.

bubble size. The simulated value of the peak pressure, due to the second collapse of the bubble, approaches the analytical value on the finer grid. Figure 3.4 (b) shows the error

$$L_n = \frac{[\int_0^3 |p(t)|^n dt]^{1/n} - [\int_0^3 |p_{KM}(t)|^n dt]^{1/n}}{[\int_0^3 |p_{KM}(t)|^n dt]^{1/n}} \tag{3.67}$$

for $n = 1{,}2$ and ∞, where p_{KM} denotes the analytical solution derived using the Keller-Miksis equation. The results demonstrate convergence, but we note that some saturation of the error is evident. This may be related to errors in the Keller-

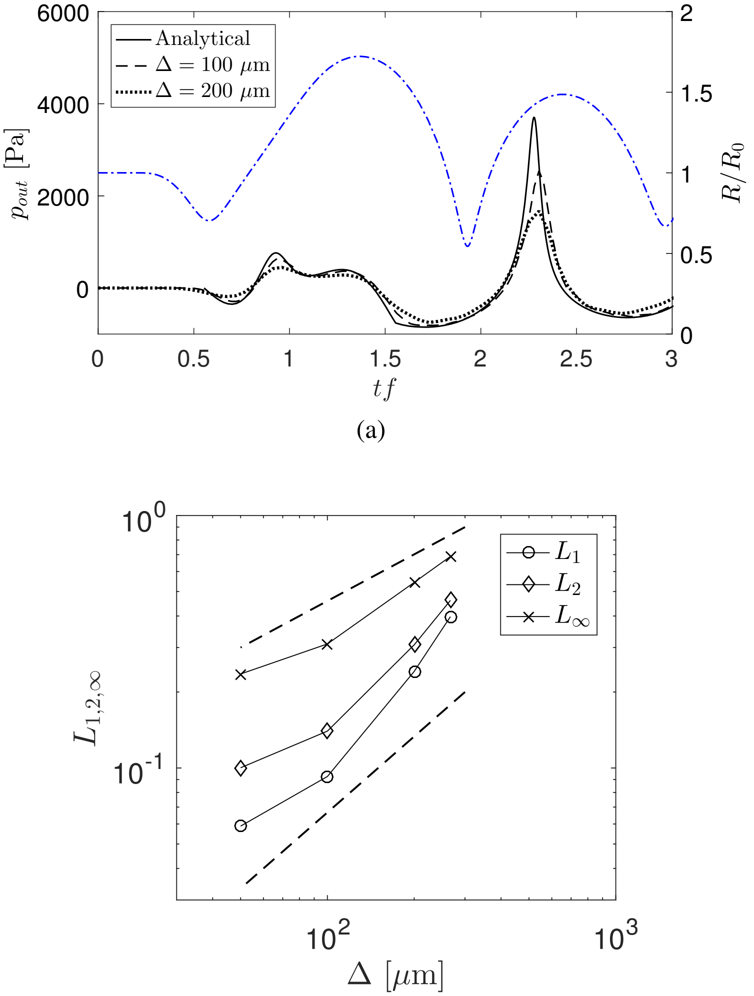

(a)

(b)

Figure 3.4: Scattered pressure wave from a single, isolated bubble with an initial radius of 10 μm under excitation with a single cycle of sinusoidal pressure wave with a frequency of 300 kHz and amplitude of 1 atm. (a) Evolution of the pressure at [-1.0, -1.0, -1.0] mm. Results using a grid size of Δ = 100 and 200 μm in the bubble are compared with analytical solution. Analytical solution of the evolution the bubble radius is also plotted with a dashed-dotted line. (b) The error norm as a function of the grid size. Reference slopes for first- and half-order convergence are included.

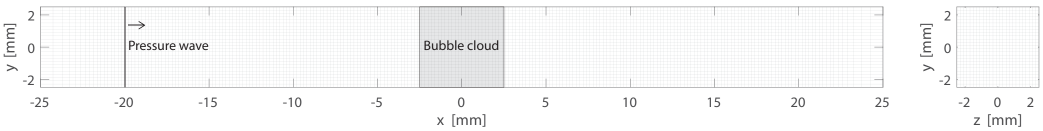

Figure 3.5: Schematic of the initial condition and the three-dimensional computational grid (only one of every two cells shown) for the bubble screen problem.

Miksis solution which makes a weakly-compressible assumption for the liquid. Nevertheless, the results shown in this section confirm that radial evolutions of a bubble as well as the bubble-scattered pressure waves are correctly captured.

Bubble screen problem

In order to verify the reduced model that uses two-dimensional volume-averaged equations, we simulate interactions of a bubble screen with a single cycle of plane, sinusoidal pressure wave using both the two- and three-dimensional models, and compare the results.

Figure 3.5 shows the schematic of the simulation setup. The domain is $x \in [-250, 250]$, $y, z \in [2.5, -2.5]$ mm. We utilize a $572 \times 50 \times 50$ and 572×50 non-uniform computational grids for three-dimensional and two-dimensional simulation to evolve the initial condition, respectively. A periodic boundary condition is applied along the domain boundaries perpendicular to the y and z axes. Non-reflective boundary conditions are implemented on the boundaries perpendicular to the x axis. Grid is smoothly stretched away from the bubble screen to prevent contamination by reflections. The grid in the bubble screen region, $x \in [-25, 25]$ mm, is uniform with $\Delta_x = \Delta_y = \Delta_z = 100$ μm. The region of bubble screen is $x, y, z \in [-2.5, 2.5]$ mm. Bubbles with an initial radius of 10 μm are randomly, homogeneously distributed in the region of the screen, with a given initial void fraction, β_0. The flow field is quiescent and at ambient pressure at the initial condition. A plane acoustic source is located at $x = -25$ mm to excite a single cycle of a sinusoidal pressure wave with an amplitude of 1 MPa and a frequency of 300 kHz in $+x$ direction. The resulting bubble oscillations are nonlinear and distinct from the results of classical bubble screen problems that considers excitations of linear oscillations of bubbles using a weak pressure wave (Commander and Prosperetti, 1989).

Figure 3.6 (a) shows the time evolution of the void fraction of the screen with various values of β_0 : $\beta_0 = [0.5, 1.0, 2.0, 4.0, 8.0] \times 10^{-5}$. For all cases, β rapidly grows after

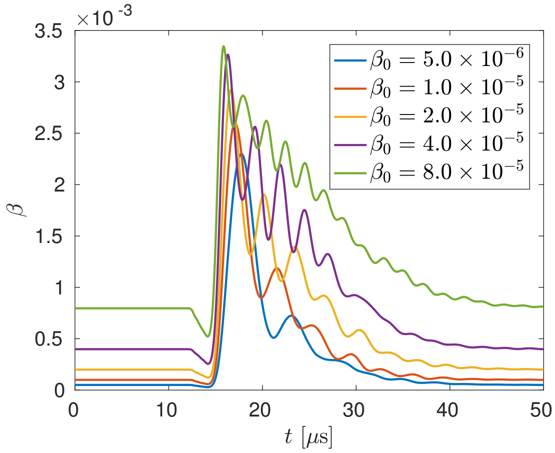

(a)

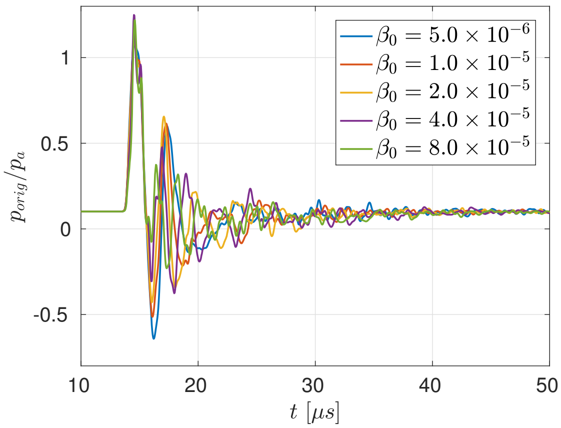

(b)

Figure 3.6: (a) Evolution of the void fraction of the screen with various values of $\beta_0 : \beta_0 = [0.5, 1.0, 2.0, 4.0, 8.0] \times 10^{-5}$. (b) Evolution of the pressure at the origin during the same set of simulations, normalized by the incident wave amplitude p_a=1 [MPa].

the passage of the wave, then smoothly decays with oscillations. The oscillations are induced by reverberations of the pressure waves trapped inside the screen. In figure 3.6 (b), we plot the time evolution of the pressure at the origin during the same set of simulations. p_{orig} grows and decays during the passage of the wave, then presents rapid fluctuations induced by the oscillations of surrounding bubbles.

Figure 3.7 shows the time evolution of the pressure and the void fraction contours on $x - y$ plane for the case with $\beta_0 = 4.0 \times 10^{-5}$. The pressure wave is partially reflected by the screen. The tensile part of the wave causes growth of the bubbles and subsequent radial oscillation. The complex structure of the scattered waves is

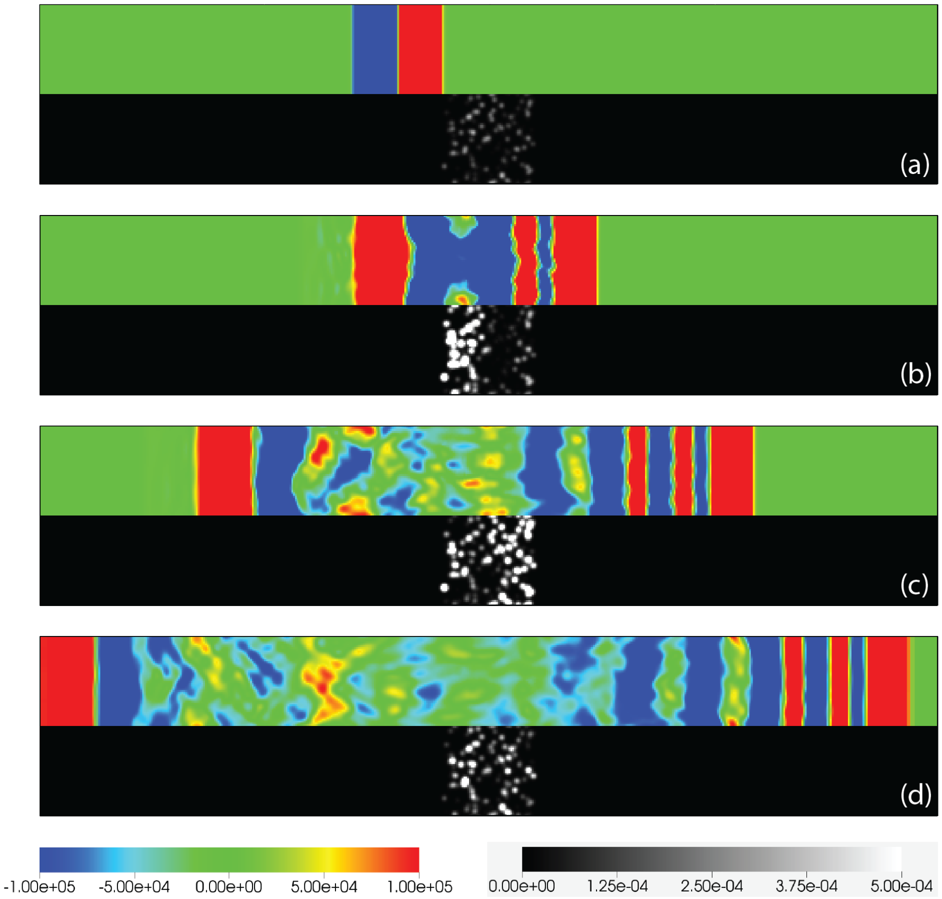

Figure 3.7: Snapshots of the pressure (top half) and the void fraction (bottom half) contours on $x-y$ plane in the range of $x \in [-25, 25]$ mm and $y \in [-2.5, 2.5]$ mm for three-dimensional simulation with $\beta_0 = 4.0\times 10^{-5}$. Note that the pressure is plotted at levels much smaller than the amplitude of the initial wave in order to highlighted the bubble-generated and scattered fields. (a) $t = 12$ μs, (b) 18 μs, (c) 24 μs and (d) 30 μs, respectively.

due to the oscillation of bubbles that last longer than the passage of the wave.

In order to verify relation (3.53), we compute $E[p'^2_{cell}]/E[(T_z p_{cell})'^2]$ on $x-y$ plane by post-processing the three-dimensional simulation data at each cell and take an average of the values over the region of $x, y \in [-2.0, 2.0]$ mm to obtain the empirical values of C_T:

$$C_{T_{Emp}} = \frac{1}{L_x L_y}\int_{-2}^{2}\int_{-2}^{2}\frac{E[p'^2_{cell}]}{E[(T_z p_{cell})'^2]}dxdy, \tag{3.68}$$

where $L_x = L_y = 4$ mm.

Figure 3.8 (a) shows the time evolution of the ratio of $C_{T_{Emp}}$ to its theoretical value

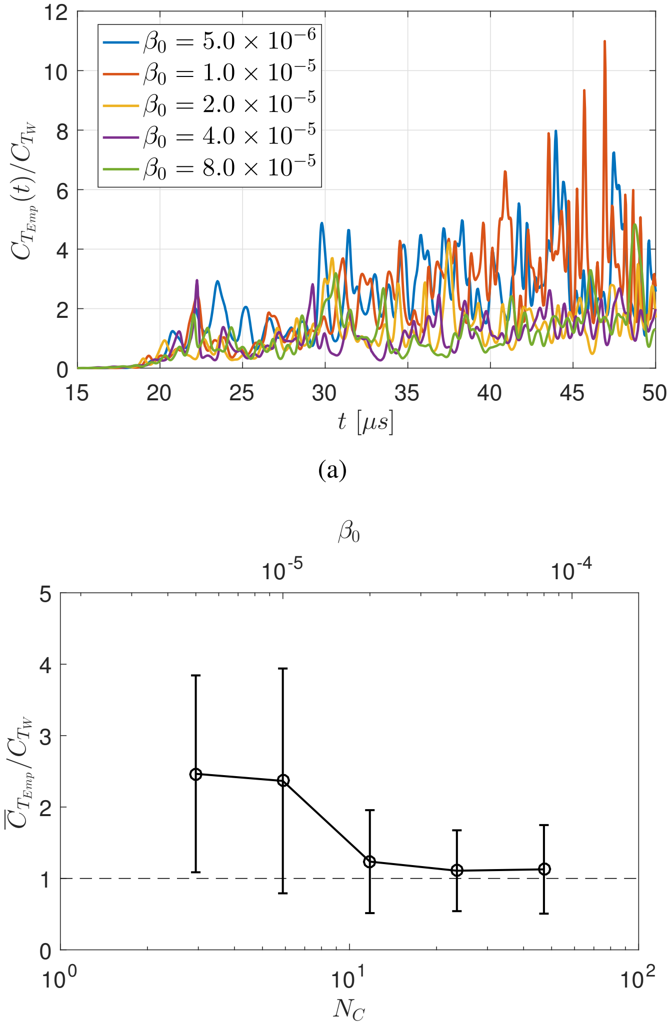

(a)

(b)

Figure 3.8: (a)Evolution of $C_{T_{Emp}}/C_{T_W}$ obtained from the three-dimensional simulations with $\beta_0 = [0.5, 1.0, 2.0, 4.0, 8.0] \times 10^{-5}$. (b)$\overline{C}_{T_{Emp}}/C_{T_W}$ obtained from the same simulations, as a function of β_0 and N_C.

obtained from the white noise model $C_{T_w} = C_T$, for simulations with various β_0. For all cases of β_0, $C_{T_{Emp}} = 0$ until around at $t = 20\mu$s, since there are no pressure fluctuations along the z axis in the domain. After the passage of the wave, $C_{T_{Emp}}$ grows due to the bubble dynamics. In the cases with $\beta_0 = 5.0\times10^{-6}$ and 1.0×10^{-5}, $C_{T_{Emp}}/C_{T_w}$ fluctuates rapidly and grows to a value of 10, while in the cases with higher values of β_0, the fluctuation is smaller and the value stays close to 1. Figure 3.8 (b) shows the averaged value of $C_{T_{Emp}}/C_{T_w}$ within the interval of $t = [20, 50]$ μs as a function of β_0 and N_C, where N_C is the averaged number of bubbles contained in the region that the operator S averages over (see equation (3.55)). In accordance with figure 3.8 (a), with $\beta_0 = 5.0 \times 10^{-6}$ and 1.0×10^{-5}, $\overline{C}_{T_{Emp}}/C_{T_w}$ takes a value much larger than 1, while with β_0 higher than 2.0×10^{-5} it takes a value close to 1. This transition corresponds to the value of N_C exceeding $O(10)$. The results indicate that with $N_c < O(10)$ the distribution of p'_{cell} is not locally isotropic in the averaging window, while with $N_c > O(10)$, the distribution of p'_{cell} becomes locally isotropic and p'_{cell} is well modeled by white noise, and thus relation (3.53) holds.

In order to assess the improvement by the stochastic closure used for the two-dimensional volume-averaged equations, we simulate the bubble screen problem with $N_{ens} = 15$ distinct initial distributions of bubbles in the screen, with a fixed value of $\beta_0 : \beta_0 = 4.0\times10^{-5}$, using the three-distinct models: the three-dimensional model, two-dimensional model, and two-dimensional model with $p'_{cell} = 0$, respectively. Then, for each method, we empirically obtain the ensemble-averaged solution by averaging the results of simulations:

$$< f(\boldsymbol{x}, t) >= \frac{1}{N_{ens}} \sum_{i=1}^{N_{ens}} f_i(\boldsymbol{x}, t), \tag{3.69}$$

where f_i is an arbitrary quantity computed in i-th simulation and $< \cdot >$ denotes the ensemble average. The purpose of comparing the ensemble-averaged solutions is to eliminate the incoherence among the distinct simulations that originates from the differences in the spatial distributions of bubbles, so that we can isolate the effect of the differences in the models on the resulting solutions.

In figure 3.9 we plot the evolution of the ensemble-averaged values of the void fraction and those of the normalized maximum radius of bubbles during the simulations. Interestingly, the choice of the model makes no visible difference in the void fraction. Meanwhile, the maximum bubble radius is significantly under-estimated after $t = 20$ μs unless the closure is applied.

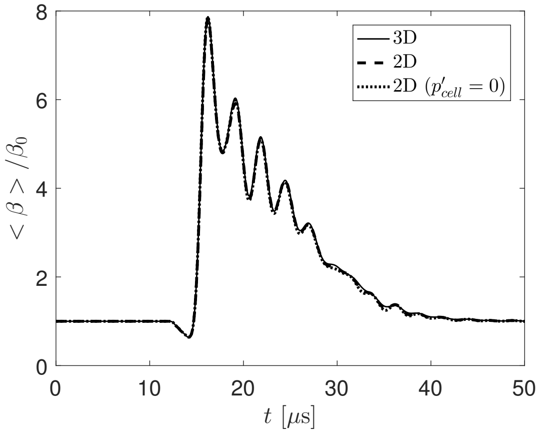

(a)

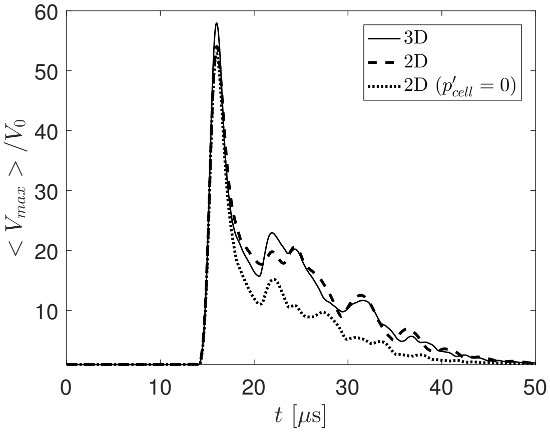

(b)

Figure 3.9: Evolution of the ensemble averaged values of (a)void fraction and (b) maximum bubble radius in the screen. Results using the three-dimensional model, two-dimensional model and two-dimensional model with $p'_{cell} = 0$ are compared.

Figure 3.10 shows the time integral of V_{max} within the interval of $t = [0, 50]$ μs obtained from the each solution of the N_{ens} simulations, normalized by its ensemble averaged value $< V_{max} >$ obtained from the three-dimensional model:

$$I_N = \int_0^{t_f} V_{N,max} dt, \tag{3.70}$$

where subscript N denotes N-th simulation. Both the value of I_N and the magnitude of fluctuations among distinct simulations are smaller in the two-dimensional simulations with $p'_{cell} = 0$, compared to those in the three-dimensional simulations. Meanwhile, the result obtained with the two-dimensional model with p'_{cell} agrees the three-dimensional simulations relatively well. We also note that with all the mod-

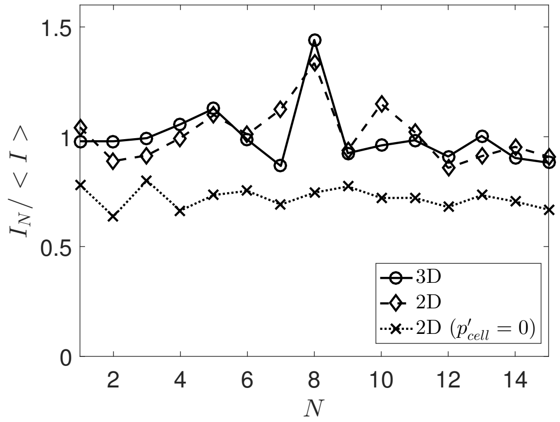

Figure 3.10: Fluctuations in I_N through 15 simulations with distinct initial conditions of bubbles: $I_N/< I >$: $N \in [1, 15]$. Results using three-dimensional model, two-dimensional model and two-dimensional model with $p'_{cell} = 0$ are compared.

els $< I >$ converges with $N_{ens} = 15$, and the ensemble averaged values obtained with the two-dimensional model with the closure is sufficiently close to that of the three-dimensional model, while that obtained without closure is smaller by 28%. Particularly in the present test case, the sub-grid pressure fluctuations influence only the maximum volume, but not the averaged void fraction. A physical interpretation of this result is that, even though the mean response of the volume of bubbles to the sub-grid pressure fluctuations is statistically close to zero, the coherence in the volumetric oscillations of the bubbles is lowered by the action of the random noise, and therefore the local maximum of the volume of bubbles is increased.

Cloud cavitation in a high-intensity ultrasound wave

Lastly, we simulate interactions of a spherical bubble cloud with plane, multiple-cycles of a sinusoidal pressure wave using the three-dimensional and axi-symmetric models and compare the results with a high-speed image of a cavitation bubble cloud obtained in an experiment. The purpose of this case is to further demonstrate the feasibility of the proposed method for cloud cavitation in ultrasound-based lithotripsy, where we observe a bubble cloud with a size of $O(1)$ mm interacting with ultrasound waves with a frequency of $O(0.1-1)$ MHz and amplitude of $O(1-10)$ MPa (Maeda, Kreider, et al., 2015). This problem is particularly challenging for previous approaches since the wavelength of the incident pressure wave is close to the size of the bubble cloud, thus the pressure field needs to be resolved at a scale smaller the cloud. Moreover, the amplitudes of the bubble-scattered pressure waves are strong so that a fully compressible liquid is needed. Figure 3.11 shows

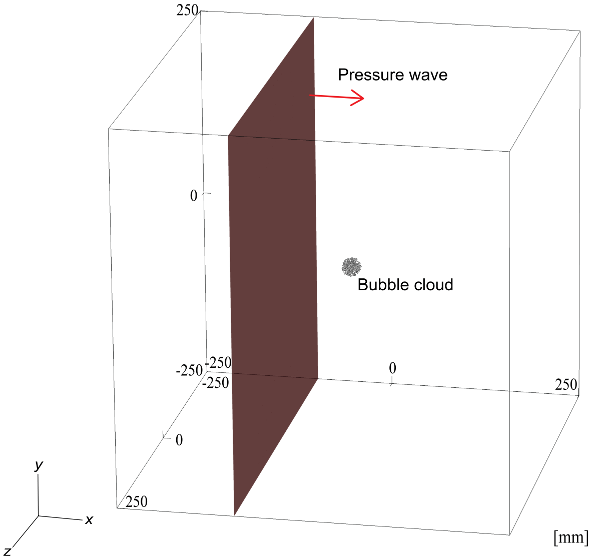

Figure 3.11: Schematic of the simulation setup for the wave-cloud interaction problem. We excite a plane, 10 cycles of a sinusoidal pressure wave with an amplitude of 1.0 MPa and a frequency of 300 kHz from a source plane located at $x = -20$ mm in the $+x$ direction. A bubble cloud with a radius of 2.5 mm is located at the origin. 625 Bubbles are randomly distributed in the region of the cloud. The radii of bubbles follow Gaussian distribution with a mean of 10 μm and a standard deviation of 2.5 μm. The initial void fraction of the cloud is $\beta_0 = 4.87 \times 10^{-5}$.

the schematic of the simulation setup. In the three-dimensional simulation, the simulation domain is $x, y, z \in [-250, 250]$ mm. The bubble cloud with a radius of 2.5 mm is located at the origin, immersed in water. The pressure of the domain is uniformly ambient and the flow field is quiescent at the initial condition. A plane acoustic source is located at $x = -20$ mm to send 10 cycles of sinusoidal pressure waves with a frequency of 300 kHz and an amplitude of 1 MPa in $+x$ direction toward the cloud. The pressure wave begins with compression and ends with tension. We utilize a $572 \times 572 \times 572$ non-uniform computational grid to evolve the initial condition. Non-reflective boundary conditions are applied along the domain boundaries. The grid size in the regions around the bubble: $x, y, z \in [-25, 25]$ mm, is uniform with $\Delta_x = \Delta_y = \Delta_z = 100$ μm. Grid is smoothly stretched away from the wave-cloud interaction region to prevent pollution from reflections. 625 bubbles are randomly distributed in the cloud. The radii of bubbles are selected from a Gaussian distribution with a mean of 10 μm and a standard deviation of 2.5 μm. The initial void fraction of the cloud is 4.87×10^{-5}. In the axi-symmetric simulation, the domain is $z \in [-250, 250]$ and $r \in [0, 250]$ mm. Grid size and stretching on $r - z$

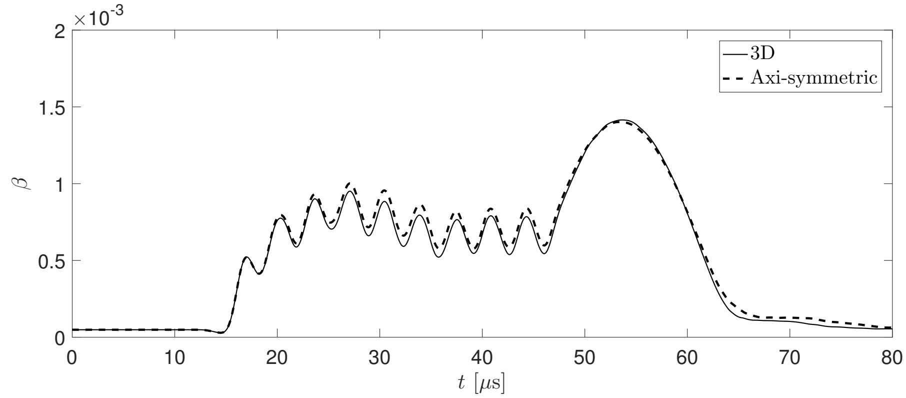

Figure 3.12: Evolution of the void fraction during cloud-wave interaction.

plane follow those on $x - y$ plane in the three-dimensional simulation. The same initial condition of bubbles is used as the three-dimensional simulation.

Figure 3.12 shows the time evolution of the void fraction. The results obtained with the two models agree very well with each other. The pressure front reaches the surface of the cloud at $t = 15.3$ μs and the tail of the wave leaves the cloud at $t = 52.5$ μs. During the passage of the wave, the void fraction oscillates between $0.5{\times}10^{-3}$ and $1.0{\times}10^{-3}$ due to excitations by the alternate compression and tension in the wave. After the passage of the wave, the bubbles continue to expand and the void fraction reaches its maximum value: 1.41×10^{-3} at $t = 53.6$ μs, before decaying to its initial value by $t = 80$ μs.

Figure 3.13 shows the images of the bubble cloud obtained with the three-dimensional model, at various stages during the evolution as well as measured probability distribution functions (PDFs) of the bubble radii in the proximal ($x < 0$) and distal ($x > 0$) half of the cloud at the corresponding times. During the passage of the wave, it is clearly seen that the bubbles in the proximal half of the cloud are larger than the bubbles in the distal half. This is confirmed in the PDF of the bubble radius in that the proximal half presents much larger peak value and broader distribution than that in the distal half. Meanwhile, around the time of maximum void fraction and subsequent collapse, the PDF is more uniform across the halves. The radial distributions of the bubbles in the two halves are similar to each other. Though the proximal half has larger radii than the distal one. Fig3.13d captures the pressure waves generated by the bubbles during the collapse.

In order to further quantify the anisotropy of the bubble cloud, in figure 3.14 we plot the evolution of the void fraction and the component of the kinetic energy,

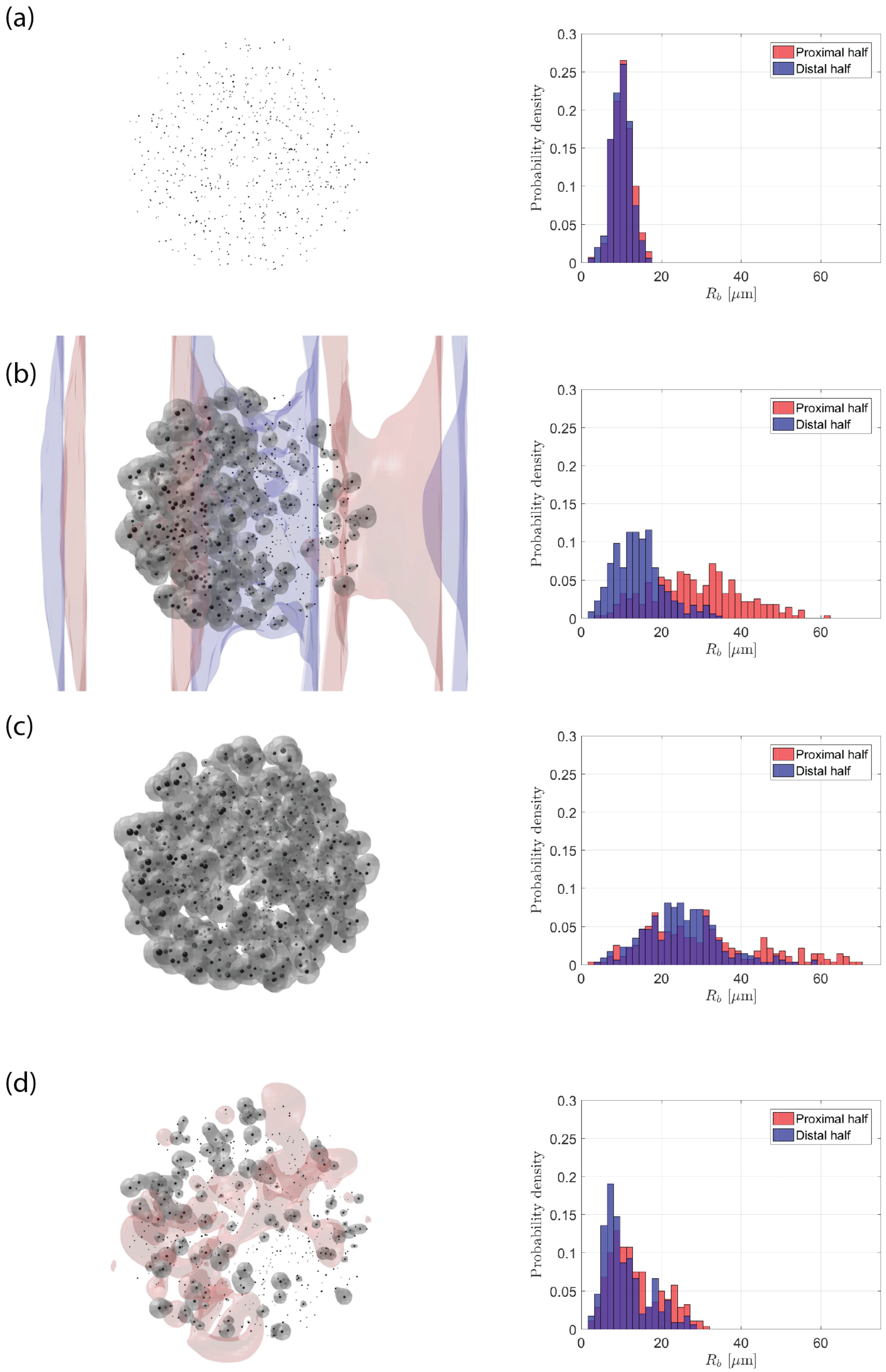

Figure 3.13: Snapshots of the bubble cloud during the simulation using the three-dimensional model. The bar charts at right show the distribution of bubble size in the proximal and distal halves of the cloud at the corresponding times.

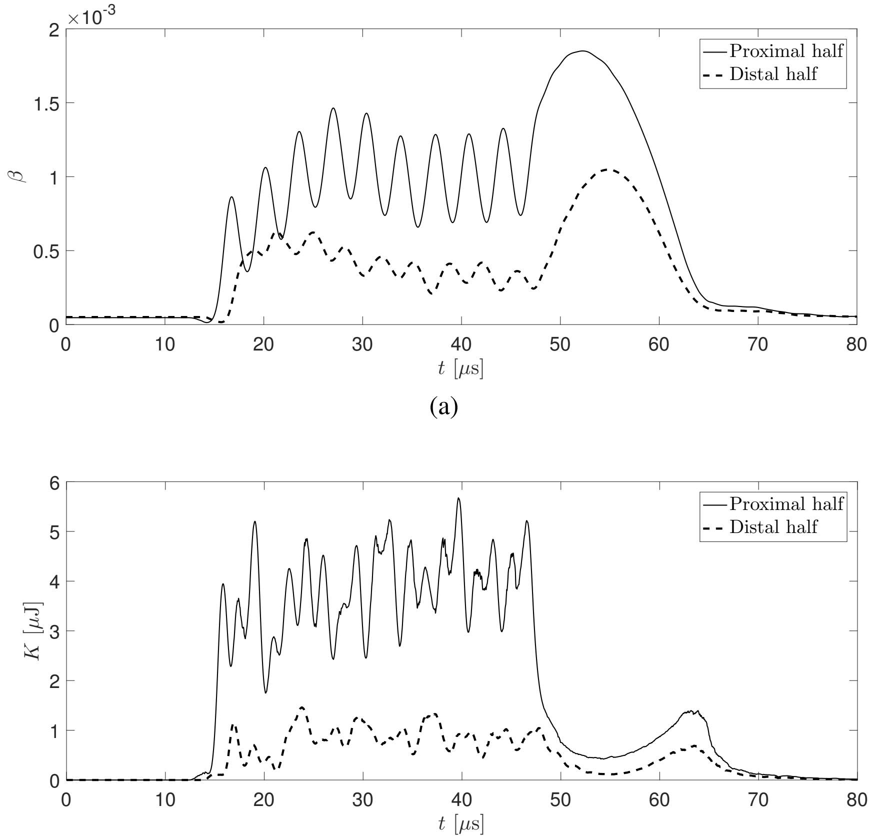

(a)

(b)

Figure 3.14: Evolution of (a) the void fraction and (b) the kinetic energy of liquid induced by the bubbles in the proximal and distal halves of the cloud.

induced by the radial oscillations of bubbles, in the proximal and distal halves of the cloud, respectively. The energy, K, is obtained by superposing the component of the kinetic energy in an incompressible flow outside each of the radially oscillating bubbles that reside in the proximal or distal half of the cloud, respectively (Caflisch et al., 1985):

$$K = 2\pi\rho \sum R_n^3(\boldsymbol{x}_n, t)\dot{R}_n^2(\boldsymbol{x}_n, t) \begin{cases} x_n < 0, & \text{Proximal half} \\ x_n > 0, & \text{Distal half} \end{cases} \tag{3.71}$$

As shown in figure 3.14 (a), during the passage of the wave, the void fraction in the proximal half oscillates around a value of 1.0×10^{-3}, while that of the distal half stays around at 0.5×10^{-3}, with a smaller amplitude of the oscillation. The phase of the oscillation in the distal half is delayed from the proximal half, due to the delay in the arrival of the incoming wave. Both of the halves experience growth and decay after the passage of the wave, yet the growth in the distal half is smaller by approximately 50%. During the passage of the wave, the value of the kinetic energy oscillates around at 4.0 μJ in the proximal half, while it oscillates around at 1.0 μJ in the distal half, with milder oscillations. The cloud's structure is the result of a shielding of the distal bubbles by the proximal ones. In other words, the proximal bubbles absorb and scatter acoustic energy such that the incident pulse is attenuated before it interacts with the distal bubbles. After the passage of the wave, the kinetic energy in both halves decay to the local minimum at around $t = 55$ μs. This decay corresponds to the decay in the radial velocity of the bubbles, when the volumetric oscillations of bubbles transit from growth to collapse. Subsequently, the kinetic energy in the both halves grows to take the local peak at around $t = 63$ μs, then decays back to zero. This simultaneous peaking corresponds to the coherent collapse of the cloud observed in figure 3.14.

During the treatment of lithotripsy, the energy shielding of kidney stones caused by bubble clouds may result in a decreased efficacy of stone comminution, and thus is a critical factor for the success of the treatment. Direct observation of the anisotropy of an acoustic cavitation bubble cloud due to the energy shielding in the numerical simulation has not, to our knowledge, been achieved in previous studies. The present method can be potentially useful to quantify the energy shielding for applications to lithotripsy and other ultrasound therapies.

3.5 Summary

In this chapter, a two-way coupled Eulerian-Lagrangian method was constructed for simulation of cloud cavitation in an intense ultrasound field. The mixture-averaged equations are discretized on an Eulerian grid, while individual bubbles are tracked as Lagrangian particles. The strong, bubble-scattered pressure waves propagating in the continuous phase are accurately captured on the grid by using a WENO-based flow solver, while the radial oscillations of bubbles are evolved by solving the Keller-Miksis equation at the sub-grid scale. Dimensional reduction of the model was achieved for cases where the bubbly mixture possesses spatial homogeneities, by descritizing the field into two-dimensional or axi-symmetric grids, and modeling the resulting missing bubble-induced pressure fluctuations at the sub-grid scale as white noise. The method is capable of capturing the multi-scale dynamics of cloud cavitation, including the pressure fluctuations at the scale of single bubble and fine structures of a bubble cloud excited by a strong ultrasound wave. Such features of the method can be useful in various applications, such as evaluation of the damage potential on materials due to the bubble collapse as well as computations of the effective, total acoustic energy delivered to a target under the presence of cavitation bubbles, during ultrasound therapies.

Chapter Appendices

3.A Numerical algorithm

In this appendix, the numerical procedure is summarized. The sequence of steps in pre-processing and simulation using the proposed method is outlined as follows.

1. Pre-processing

(a) Initialize $\boldsymbol{q}_{l,i,j,k}$ on a grid given the initial condition.

(b) If two-dimensional or axi-symmetric simulation: generate random phase $\phi_{k_{i,j}}$.

(c) Initialize Lagrangian variables R_n, $\dot{R}_n$, p_{Bn}, and m_n, given the initial condition.

2. Simulation
During each RK-step:

(a) Compute RHS of equation (3.19) using the WENO scheme.

(b) Smear V_n and $\dot{V}_n$ on the grid to obtain β and $\dot{\beta}$ using the kernel.

(c) Compute $\boldsymbol{g}_{i,j,k}$.

(d) Obtain p_{cell} (Tp_{cell} in case of two-dimensional or axi-symmetric simulation) at the coordinate of each bubble.

(e) If three-dimensional simulation: compute p_∞ at the coordinate of each bubble.

(f) If two-dimensional or axi-symmetric simulation: compute p'_{cell} at each coordinate of the bubble.

(g) Compute $\dot{R}_n$, $\ddot{R}_n$, $\dot{p}_{Bn}$, and $\dot{m}_{Vn}$.

(h) Update $\boldsymbol{q}_{l,i,j,k}$.

(i) Update R_n, $\dot{R}_n$, p_{Bn}, and m_{Vn}.

3.B Scaling and performance of the flow solver

In this appendix, the parallel scalability and performance of the WENO flow solver used to integrate the Eulerian variables are described. Test runs are considered to solve the homogeneous Euler equation in three-dimensional space with various number of finite volume cells without Lagrangian bubbles. WENO5 and third-order TVD Runge-Kutta (RK) scheme are employed for spatial reconstruction and

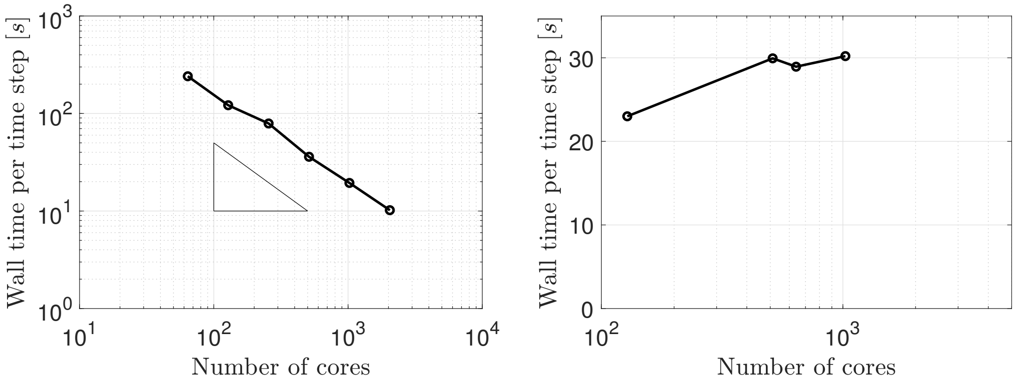

(a) (b)

Figure 3.15: (a) The strong scaling performance of the solver for 500^3 cells. The triangle denotes a linear slope. (b) The weak scaling performance for 50^3 cells per core.

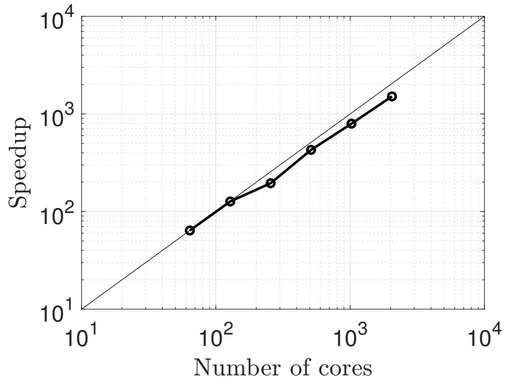

Figure 3.16: The speedup performance of the solver for 500^3 cells.

time integration, respectively. Other numerical conditions follow those used in the previous sections. The Eulerian grid is decomposed into sub-domains that are allocated to distinct processors using a Message Passing Interface (MPI) protocol. The overhead and data output costs are excluded from the measurement of the wall clock time per time step. The test runs were conducted on the Stampede2 (phase1) system at the Texas Advanced Computing Center at the University of Texas at Austin.

Figure 3.15 and figure 3.16 show the strong and weak scaling performance, and the speedup performance of the solver. The results are reasonably close to linear scaling and confirm the good scalability properties and performance of the solver.

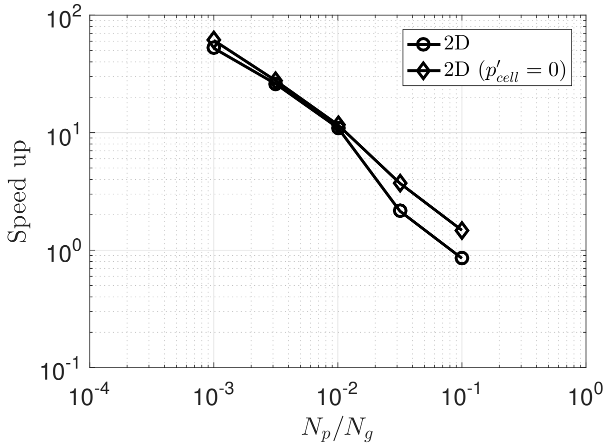

Figure 3.17: Speed up by using the two dimensional model, with and without modeling p'_{cell}.

3.C Speedup with the reduced model

In this appendix, the reduction in the computational cost by using the reduced models from the three-dimensional model is quantified. In a test problem, we solve for the dynamics of N_P bubbles distributed in a domain with a size of $x, y, z \in [-2.5, 2.5]$ mm. The domain is descritized into $N_G = 50^3$ finite volume cells for three-dimensional simulations, and $N_G = 50^2$ cells for two-dimensional simulations. For $N_P/N_G \in [10^{-3}, 10^{-1}]$, we measure the wall time required to march the governing equations by a single time step by using the three-dimensional model, the two-dimensional model, and the two-dimensional model with $p'_{cell} = 0$, namely T_{3D}, T_{2D}, and T_{2D_0}, respectively. Then we compute the speed-up in the wall time: T_{3D}/T_{2D} and T_{3D}/T_{2D_0}. For all the test problems, we use a single CPU core of Intel Xeon E2670v3 processor.

Figure 3.17 shows the results. The speed-up is $O(1 - 10^2)$. In all the cases, the total cost of the simulation is the summation of the cost to compute the Eulerian field and that of the Lagrangian bubbles. With $p'_{cell} = 0$ the speed-up is expected to be globally larger than 1 (the two-dimensional model is always faster), since the cost of time marching the Lagrangian bubbles is the same between the three-dimensional and two-dimensional models except for the smearing procedures, while the cost of the Eulerian field is globally smaller in the two-dimensional model. By increasing the number of particles, the speed-up decreases, since the cost of the Lagrangian bubbles becomes dominant in the total cost, and the reduction in the cost of the Eulerian phase contributes less to the total cost. The speed-up with the two-dimensional model with p'_{cell} follows a similar trend as $p'_{cell} = 0$. However, with the same N_P/N_G, the speed-up with modeling p'_{cell} is smaller than that with $p'_{cell} = 0$. This difference corresponds to the overhead to compute p'_{cell}. With $N_P/N_G = 10^{-1}$, the speed-up is smaller than 1 (the two-dimensional model is slower). This result indicates that the magnitude of the cost reduction in the Eulerian field is smaller than the overhead of modeling p'_{cell} when $N_P/N_G > O(10^{-1})$, with the particular grid of the test problem. The result also implies that the two-dimensional model with $p'_{cell} = 0$ would be useful in terms of speed-up and cost-reduction, when p'_{cell} does not alter solutions to within an accuracy of interest.

The results also hold in a parallel environment, in which a computational domain, including both the Eulerian field and the Lagrangian particles, is decomposed into sub-domains using the MPI protocol. In that case, the global speed-up is bounded by the speed-up of the sub-domain that has the largest value of N_P/N_G.

3.D Details of the sub-grid modeling to obtain p_∞ for the three-dimensional model

In this appendix, we describe the detailed derivation of the expression of p_{out} (3.31) used in the bubble dynamic closure for the three-dimensional model. The original sub-grid closure of the Keller-Miksis equation was proposed by FC, in a regime in which multiple-bubbles reside in a single finite volume cell (Fuster and Colonius, 2011). Here we revisit the derivation in a regime where we have at most single bubble in a finite volume cell. To the aim, we consider a bubble with radius R_n in the control volume V_{cell}. At the sub-grid scale, it can be assumed that the liquid is incompressible and the flow field is irrotational. Thus at an arbitrary coordinate in the liquid in V_{cell}, the following Bernoulli's equation holds:

$$\frac{\partial \phi}{\partial t} = \frac{1}{2}(\nabla \phi)^2 + \frac{p - p_0}{\rho}, \tag{3.72}$$

where ϕ is the velocity potential. ϕ can be decomposed into the velocity potential of the in-coming pressure wave and the out-going wave emitted by the bubble oscillation:

$$\phi = \phi_\infty + \phi_n. \tag{3.73}$$

Note also that, without the presence of the bubble, the Bernoulli's equation can be simplified as

$$\frac{\partial \phi_\infty}{\partial t} = \frac{p_\infty - p_0}{\rho}. \tag{3.74}$$

By using equations (3.72-3.74), we obtain

$$\frac{p - p_\infty}{\rho} = -\frac{\partial \phi_n}{\partial t} + \frac{1}{2}(\nabla \phi_n)^2. \tag{3.75}$$

Though we do not know the value of p_∞ a-priori, it is approximately constant over V_{cell}. The other terms are functions of the distance from the center of the bubble r. In order to eliminate p_∞, we derive two expressions.

First, we write

$$\frac{1}{V_{l,cell}} \int_{V_{cell}} \frac{p - p_\infty}{\rho} dv_l = \frac{1}{V_{l,cell}} \int_{V_{cell}} \left[-\frac{\partial \phi_n}{\partial t} + \frac{1}{2}(\nabla \phi_n)^2 \right] dv_l, \tag{3.76}$$

where $V_{l,cell} = \int_{V_{cell}} dv_l$. Notice that

$$\frac{1}{V_{l,cell}} \int_{V_{cell}} p dv_l = p_{cell}, \tag{3.77}$$

and thus the relation can be re-written as

$$\frac{p_{cell} - p_\infty}{\rho} = -\frac{1}{V_{l,cell}} \int_{V_{cell}} \frac{\partial \phi_n}{\partial t} dv_l + \frac{1}{V_{l,cell}} \int_{V_{cell}} \frac{1}{2}(\nabla \phi_n)^2 dv_l. \tag{3.78}$$

In order to explicitly express the right hand side, we approximate the integrals by assuming that the control volume V_{cell} is a sphere with a radius of $R_{cell} = (3/4\pi V_{cell})^{1/3}$ and the bubble resides at the center of the sphere. By doing so, we can approximate the integral operator:

$$\int_{V_{cell}} (\cdot) dv_l \approx \int_{R_n}^{R_{cell}} (\cdot) 4\pi r^2 dr. \tag{3.79}$$

We naturally have $V_{l,cell} = \frac{4}{3}\pi(R_{cell}^3 - R_n^3)$. The integrands of the RHS of equation (3.78) can be expressed in terms of r and the states at the surface of the bubble:

$$\frac{\partial \phi_n(r)}{\partial t} = \frac{R_n}{r} \frac{\partial \phi_b(R_n)}{\partial t}, \ \ \nabla \phi_b(r) = \frac{R_n^2 \dot{R}_n}{r^2}. \tag{3.80}$$

Substituting these expressions, we obtain

$$\frac{1}{V_{l,cell}} \int_{V_{cell}} \frac{\partial \phi_n}{\partial t} dv_l \approx \underbrace{\frac{3}{2} \frac{R_n(R_{cell}^2 - R_n^2)}{R_{cell}^3 - R_n^3}}_{C_1(R_n, R_{cell})} \frac{\partial \phi_b(R_n)}{\partial t}, \tag{3.81}$$

$$\frac{1}{V_{l,cell}} \int_{V_{cell}} \frac{1}{2}(\nabla \phi_b(R_n))^2 dv_l \approx \underbrace{\frac{3}{4} \frac{R_n^3}{R_{cell}^3 - R_n^3} \left(1 - \frac{R_n}{R_{cell}}\right)}_{C_2(R_n, R_{cell})} \dot{R}_n^2. \tag{3.82}$$

Finally, we can re-write the relation (3.78) as

$$\frac{p_{cell} - p_\infty}{\rho} \approx -C_1 \frac{\partial \phi_n(R_n)}{\partial t} + C_2 R_n^2. \tag{3.83}$$

This equation represents the averaged contribution of the bubble dynamics to the pressure in V_{cell}.

The second equation needed to estimate p_∞ is simply equation (3.75) evaluated at the surface of the bubble:

$$\frac{p_n - p_\infty}{\rho} = -\frac{\partial \phi_n(R_n)}{\partial t} + \frac{1}{2} R_n^2, \tag{3.84}$$

where we used $p(R_n) = p_n$ and $\nabla\phi(R_n) = \dot{R}_n$. This equation represents the contribution of the bubble dynamics to the pressure at the surface of the bubble.

Now that we have two unknown variables, $\partial\phi(R_n)/\partial t$ and p_∞, in two equations. It is straightforward to eliminate the unknowns to obtain

$$\frac{1}{V_{l,cell}} \int_{V_{cell}} p_{out} dv_l = p_{cell} - p_\infty \approx \frac{1}{1 - C_1} \left[p_{cell} - p_n - \left(C_2 - \frac{1}{2} \right) \rho \dot{R}_n^2 \right]. \tag{3.85}$$

Chapter 4

DYNAMICS OF BUBBLE CLOUDS IN AN ULTRASOUND FIELD

A part of this chapter has been accepted for publication in the proceedings of The ASME 5th Joint US-European Fluids Engineering Summer Conference (FEDSM2018) and submitted to Journal of Fluid Mechanics.

4.1 Overview

In the previous chapter, the three-dimensional simulation of a cavitation bubble cloud identified an anisotropic structure in the cloud during a passage of the strong ultrasound wave. The dynamics of cavitation bubble cloud in the regime have not been previously addressed and mechanisms leading to the structure are elusive. In this chapter, the dynamic of bubble cloud are investigated through laboratory experiments and numerical simulations.

Early studies on cloud cavitation focused on assessment of cavitation noise and erosion on materials in cavitating flows. Mørch (1980) and Mørch (1982) theoretically modeled the inward-propagating collapse of spherical bubble clusters by a shockwave and quantified the resulting collapse pressure. Omta (1987) studied acoustic emission from the spherical bubble cloud excited by step change of the pressure in the surrounding liquid. d'Agostino and Brennen (1989) formulated the linearized dynamics of monodisperse, spherical bubble clouds under weak, long wavelength pressure excitation and identified that the cloud interaction parameter, $B = \beta R_c^2/R_{b0}^2$, dictates the linear dynamics of the cloud, where β is the void fraction, R_c and R_{b0} are the initial radius of the cloud and the bubbles, respectively. Wang and Brennen (1994) and Wang and Brennen (1999) extended the study to the nonlinear regime, further characterizing the strong collapse of bubble clouds accompanied by a shockwave. Shimada et al. (2000) used a similar approach to assess the effect of the polydispersity of nuclei on the nonlinear dynamics of spherical bubble clouds.

Later, numerical studies of cavitation have gained interest for medical applications. Tanguay and Colonius (2003) extended the mixture-averaging approach to simulate and characterize the dynamics of cavitation bubble clouds induced in extra-corporeal shock wave lithotripsy (ESWL). Matsumoto and S. Yoshizawa (2005) extended the method of Shimada et al. (2000) to quantify amplifications in the pressure due to bubble cloud collapse under excitation by resonant HIFU waves and discussed applications of the collapse energy to kidney stone comminution as an alternative method of ESWL.

In experiments, Reisman et al. (1998) used high-speed imaging to observe cloud cavitation collapse on a finite-span hydrofoil, and analyzed acoustic signals from the cloud collapse, and associated the results with the inward propagating shockwave predicted in the aforementioned studies. Arora et al. (2007) observed collapse in bubble clouds of controlled nuclei concentration, and observed an inward-propagating collapse with high nuclei concentrations.

Many of the aforementioned studies focus on bubble clouds in an otherwise incompressible liquid so that the wavelength of the pressure excitation is much larger than the size of the cloud. In practical conditions of ultrasound therapies, however, the scale separation invoked above does not often hold. As noted in Chapter 1, Maeda, Kreider, et al. (2015) observed bubble clouds with a size of $O(1)$ mm *in vitro* during the passage of a strong ultrasound wave with a wavelength as short as the cloud size. In a similar regime, numerical simulation revealed the anisotropic structure in the cloud. These dynamics are significantly different from bubble clouds in the long wavelength regime.

Advanced interface capturing methods are capable of simulating detailed dynamics of each bubble in a cloud in a compressible liquid at fine spatial scales, and have been applied to bubble cloud collapse in a free field by Rossinelli et al. (2013) and Rasthofer et al. (2017) and near a wall by Tiwari et al. (2015). Yet, such methods are still computationally intensive and applications are limited to the dynamics within a short time scale, typically that of a single cycle of bubble collapse. For more complex problems, modeling assumptions have to be made to reduce the computational cost. Therefore, as claimed, the Eulerian-Lagrangian method developed in the previous chapter is a critical tool to accurately simulate the cloud cavitation in HIFU with a reasonable computational expense.

In order to further confirm the physical fidelity of the method, preliminary simulations are conducted to reproduces the aforementioned spherical cloud collapse accompanied by inward propagating shockwave. Figure 4.1 shows the evolution of bubbles with an initial radius of 10 μm that are randomly distributed in a ball with a radius of 2.5 mm to make an initial void fraction of 8.0×10^{-5} and excited by a single cycle of a plane sinusoidal wave with a frequency of 50 kHz, thus a wavelength of

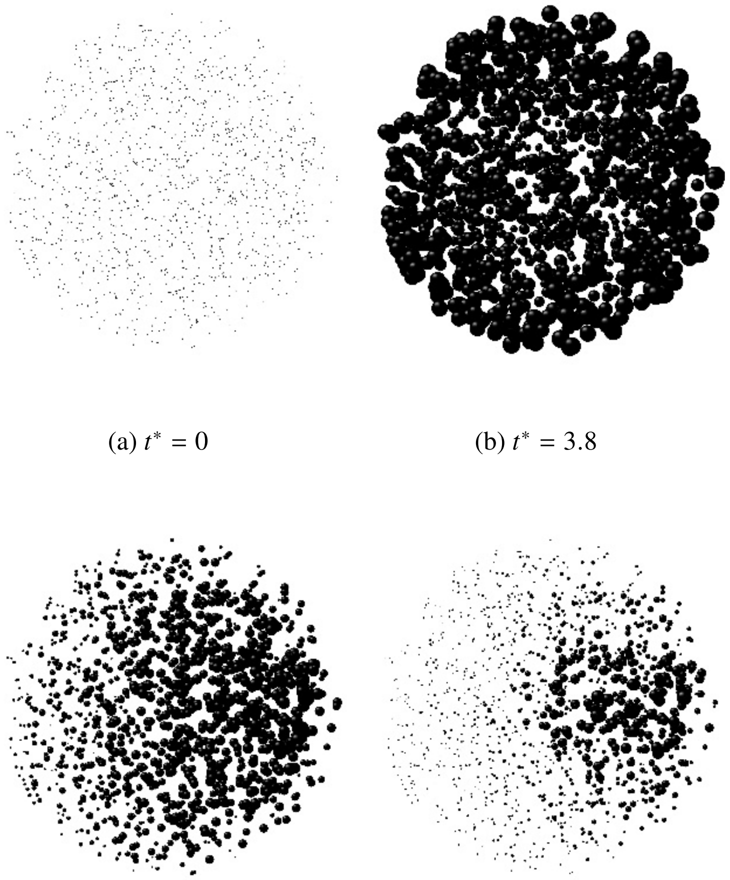

(a) $t^* = 0$ (b) $t^* = 3.8$

(c) $t^* = 6.9$ (d) $t^* = 7.3$

Figure 4.1: Evolution of a bubble cloud excited with a single cycle of sinusoidal wave with a frequency of $f = 50$ kHz. t^* denotes non-dimensional time $t^* = tf$.

50 mm, and an amplitude of 1 MPa. The wavelength is much longer than the cloud size, that effectively satisfies the scale separation. Figure 4.2 shows the evolution of the radii of representative bubbles that are initially located at three distinct radial coordinates of the cloud: cloud center, mid-point between the center and the cloud periphery, and periphery. The peripheral bubble grows to a larger maximum radius and collapse faster than the other bubbles, while the inner bubbles are subsequently collapsed during the arrival of the inward propagating bubbly shockwave. The result qualitatively reproduces the numerical simulation of Wang and Brennen (1994) and Wang and Brennen (1999) as well as the experimental observation of Arora et al. (2007). Further details of the preliminary simulation can be found in chapter appendix.

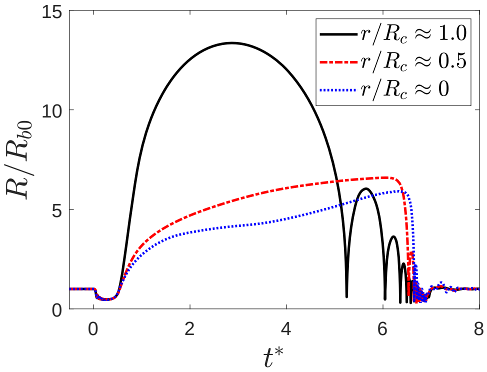

Figure 4.2: Evolution of the radii of representative bubbles at distinct radial coordinates in the cloud.

Motivated by the success of the preliminary simulation, the dynamics of cavitation bubble clouds are further investigated through experimental high-speed imaging and numerical simulations. The remainder of this chapter is organized as follows. § 4.2 describes an experimental setup for high-speed imaging of a bubble cloud excited by a focused ultrasound wave in water. In § 4.3 we introduce metrics to quantify the dynamics of bubble clouds, including the cloud interaction parameter introduced by d'Agostino and Brennen (1989), and the moments of the volume and the kinetic energy. In § 4.4 we simulate the dynamics of bubble clouds excited by a focused ultrasound wave with various polydispersities and populations of nuclei in a setup that mimics the experimental condition. We quantitatively compare results with the experimental high-speed images shown in figure 4.5 and evaluate the anisotropic structure. To further elucidate the dynamics in more generalized conditions, in § 4.5 we conduct a parametric study of bubble clouds excited by a plane ultrasound wave, varying the nuclei populations and the amplitudes of the wave. In § 4.5 we quantitatively analyze the anisotropic structure, and in § 4.5 we propose a new scaling parameter to characterize the dynamics of the clouds by generalizing the cloud interaction parameter of d'Agostino and Brennen (1989). In § 4.5 we collapse the moments of bubble-induced kinetic energy in terms of the proposed parameter and identify the mechanisms by which energy is localized in the proximal side of the cloud. In § 4.5 the amplitude and directionality of the scattered acoustic field are evaluated and collapsed by the proposed parameter. The energy localization and the scattered acoustics are directly correlated. In § 4.6 we discuss implications of the numerical results to the effects of cloud cavitation on outcomes of HIFU-based lithotripsy. In § 4.7 we state a chapter summary.

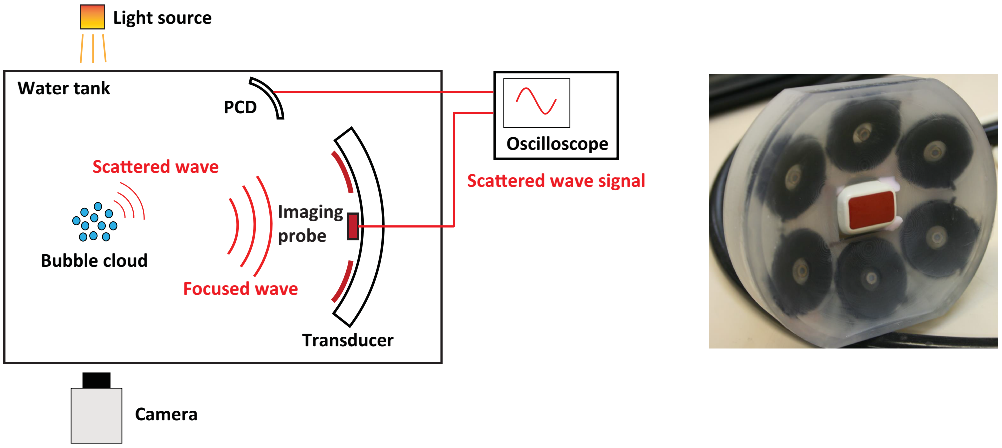

(a) (b)

Figure 4.3: (a) Schematic of the experimental setup. (b) Piezo-ceramic medical transducer used in the experiment.

4.2 Experimental high-speed imaging

Experimental setup

Figure 4.3a shows the schematic of the setup. The experiment, extended from a setup documented in Maeda, Kreider, et al. (2015), is designed to characterize the dynamics of bubble clouds in BWL. The setup is designed to capture the evolution of a single, isolated cavitation bubble cloud excited in a focused, traveling ultrasound wave. The temperature and pressure are ambient. The water is degassed by a vacuum pump to realize the oxygen level of 75%. A medical transducer composed of six piezo-ceramic array elements (figure 4.3b) is immersed in water. The transducer has an aperture of 110×104 mm, and a focal length of 120 mm. An imaging probe is attached at the center of the transducer. We excite burst waves at the transducer with a pulse-repetition-frequency (PRF) of 200 Hz. A high-speed camera captures a rectangular region with a dimension of 15.3×12.5 mm around the focal point of the transducer. The camera captures 14 consecutive frames with a frame rate of 6 μs and an exposure time of 50 ns, with a resolution of 1200×980 pixels with a pixel size of 13×13 μm. A focused passive cavitation detector (PCD) with Polyvinylidene difluoride (PVDF) membrane, with ROC of 150 mm and an aperture of 50mm, is positioned confocal to the transducer. We use acoustic signals captured by the imaging probe and the PCD to map the location of cavitation site to confirm that the bubble cloud captured by the camera is isolated and no other cloud is present outside the window of the camera. All the high-speed images presented here are vertically reflected for consistency with the simulations. This alters no quantities

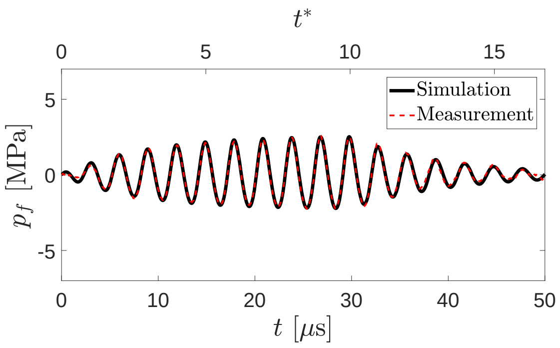

Figure 4.4: Measurement of the focal pressure evolution used for calibration of the modeled transducer in the simulation.

presented.

With the input of N_C cycles of a sinusoidal voltage, the output of the transducer is modeled by the following formula:

$$p_{trans} = p_a \cos(2\pi f t)[(1 - e^{-t/\tau_u}) - (1 - e^{-(t-N_c/f)/\tau_d})H(t - \frac{N_c}{f})], \tag{4.1}$$

where τ_u and τ_d are the ring-up and ring-down time, respectively. In the simulations of focused waves, we excite this expression of the pressure at the source plane, with $\tau_u = 4.0$ and $\tau_u = 8.0$ μs. Figure 4.4 shows the simulated focal pressure evolution and the experimental measurement using a fiber-optic hydrophone. The result of the simulation agrees very well with the measurement. Details of the numerical setup is described in § 4.4.

In figure 4.5 we show the evolution of a representative bubble cloud nucleated in a pulse of focused ultrasound containing sinusoidal form of pressure waves with a frequency of $f = 335$ kHz, thus a wavelength of $\lambda = 4.4$ mm. The peak maximum and negative focal amplitudes are adjusted to 6.0 and -4.5 MPa, respectively. The observed cloud has a nearly spherical profile with $R_C \approx 2.5$ mm, but possesses an anisotropic structure in that proximal bubbles grow to larger radius than distal bubbles.

4.3 Theory and scaling for the dynamics of bubble clouds

Cloud interaction parameter

d'Agostino and Brennen (1989) (hereafter DB) studied the linear response of monodisperse, spherical bubble clouds subjected to harmonic, long wavelength pressure excitation. DB deduced that the response of the bubble cloud with a low

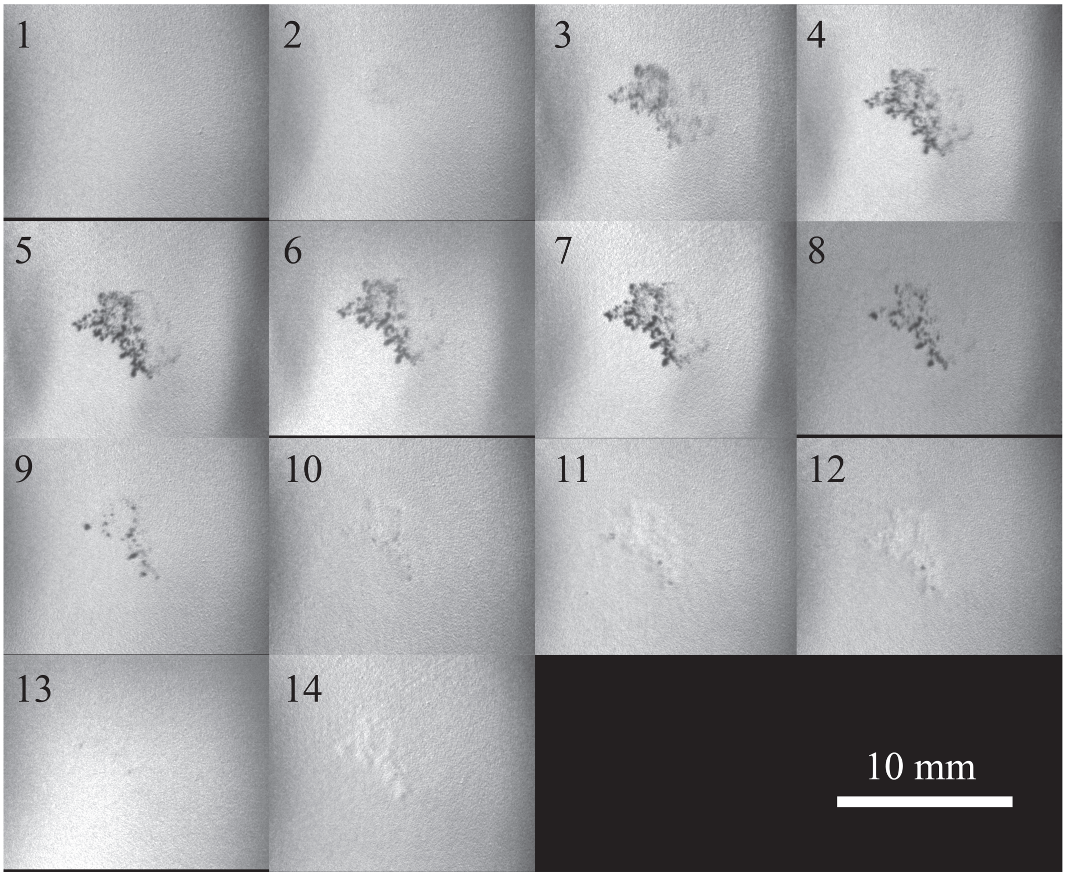

Figure 4.5: High-speed images showing evolution of the bubble cloud excited by a focused ultrasound wave.

void fraction is characterized by a non-dimensional parameter,

$$B_0 = \frac{\beta_0 R_c^2}{R_{b0}^2}, \tag{4.2}$$

termed as the *cloud interaction parameter*. DB found that, when $B_0 \ll 1$, the effect of inter-bubble interaction is weak and each bubble in the cloud behaves like a single, isolated bubble. When $B_0 \gg 1$, inter-bubble interactions cause bubbles to oscillate coherently at a lower frequency than an isolated single bubble. Wang and Brennen (1999) simulated the dynamics of a spherical bubble cloud with various values of B_0 in the nonlinear regime.

The cloud interaction parameter can be interpreted in different ways. Substituting $\beta = N_b R_{b0}^3 / R_c^3$ into equation 4.2, B_0 can be rewritten as

$$B_0 = \frac{N_b R_{b0}^3}{R_c^3} \frac{R_c^2}{R_{b0}^2} = \frac{N_b R_{b0}}{R_c}, \tag{4.3}$$

where N_b is the number of bubbles in the cloud. We notice that this scaling parameter can be independently derived from the Lagrangian mechanics of spherical bubbles under mutual interactions. The global kinetic energy of the potential flow of an incompressible liquid induced by volumetric oscillations of N_b spherical bubbles can be expressed using a multipole expansion (Takahira et al., 1994; Ilinskii et al., 2007) as

$$K = 2\pi\rho\left[\sum_{i}^{N_b} R_i^3\dot{R}_i^2 + \sum_{i}^{N_b}\sum_{j}^{N_b}\frac{R_i^2R_j^2\dot{R}_i\dot{R}_j}{r_{i,j}} + O\left(\frac{R^7\dot{R}^2}{r^4}\right)\right], \tag{4.4}$$

where $r_{i,j}$ is the distance between the centers of bubble i and bubble j. The first term in the bracket represents the kinetic energy induced by direct contributions from each bubble and the second term represents the energy induced by the inter-bubble interactions. When bubbles have an approximately uniform size distribution and experience simultaneous change in pressure, we can assume that each bubble takes the same characteristic radius and the velocity, R and $\dot{R}$. The characteristic inter-bubble distance can be scaled as $r \sim R_c$. Then K can be scaled as

$$K \sim N_bR^3\dot{R}^2\left(1 + \frac{N_bR}{R_c}\right). \tag{4.5}$$

In the limit of small amplitude oscillations we have $R \approx R_{b0}$, and therefore we obtain

$$K \sim N_bR_{b0}^3\dot{R}^2\left(1 + B_0\right). \tag{4.6}$$

We see that the interaction parameter dictates the kinetic energy induced by bubbles. With $B_0 = 0$ the kinetic energy is that of an isolated bubble, while with $B_0 > 1$ there is an additional contribution from the inter-bubble interactions. Based on equation (33), an extended R-P equation for the dynamics of the bubbles can be derived (Takahira et al., 1994; Doinikov, 2004; Bremond et al., 2006; Ilinskii et al., 2007; Zeravcic et al., 2011). In fact, the scaling of kinetic energy in terms of N_bR_b/R_c was mentioned by Ilinskii et al. (2007), but was not associated with the parameter derived by DB.

In what follows we specify the size distribution of nuclei to be log-normal distribution given by $\ln(R_b/R_{b,ref}) \sim N(0,\sigma^2)$. Therefore we employ the following expression for B_0:

$$B_0 \approx \frac{N_bR_{b0,ref}}{R_c}. \tag{4.7}$$

Moments

In order to quantify the anisotropic structure and associated bubble dynamics, we use the moments of either bubble volume or kinetic energy of the liquid, both measured

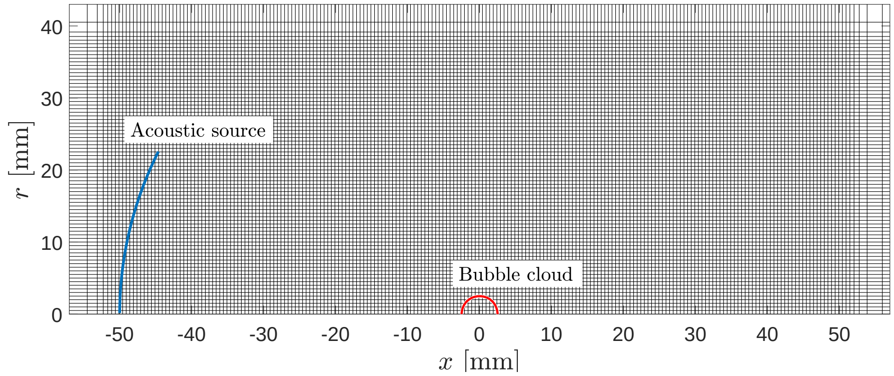

Figure 4.6: Schematic of the numerical setup. Every fifth point is plotted in the computational mesh.

with respect to the initial center of the cloud (hereafter denoted as the moment of volume and moment of kinetic energy, respectively). The n-th moments of the bubble volume and the bubble-induced kinetic energy of liquid are thus respectively defined as

$$\mu_{Vcn} = \frac{\sum_{bubble} \frac{4\pi}{3} R_b^3 \left(\frac{x_b}{R_c}\right)^n}{\sum_{bubble} \frac{4\pi}{3} R_b^3} \quad and \quad \mu_{Kcn} = \frac{\sum_{bubble} 2\pi\rho R_b^3 \dot{R}_b^2 \left(\frac{x_b}{R_c}\right)^n}{\sum_{bubble} 2\pi\rho R_b^3 \dot{R}_b^2}. \tag{4.8}$$

We will treat the first moment ($n = 1$), unless otherwise noted. The moments are normalized to vary within the range of $[-1, 1]$. In an extreme case, when monodisperse bubbles are distributed in a left hemisphere ($-x$) and oscillate with the same radial velocity, the 1st moments satisfy $\mu_{Vcn} = \mu_{Kcn} = -0.375$. Therefore, moments smaller than this value indicate a large bias in the volume or kinetic energy toward the proximal side of the cloud.

4.4 Cloud cavitation in a focused ultrasound wave

Setup

In order to investigate the dynamics of bubble clouds, we conduct numerical simulations that mimics the laboratory setup. Figure 4.6 shows the schematic of numerical setup. The size of the simulation domain is 500×250 mm, which has been verified to be sufficiently large to effectively mimic free space. For the initial condition, we randomly distribute bubble nuclei in a spherical region of with radius 2.5 mm with its center located at the origin of $x - r$ axi-symmetric coordinates. The grid size is uniform near the region of bubble cloud with a characteristic grid size of 100 μm. Symmetry boundary condition is used on the axis of symmetry. The grid is smoothly stretched toward the other domain boundaries, where characteristic boundary con-

Run	B_0	σ
F1	0.625	0
F2	1.25	0
F3	2.5	0
F4	5.0	0
F5	0.625	0.7
F6	1.25	0.7
F7	2.5	0.7
F8	5.0	0.7

Table 4.1: List of parameters used 8 runs for simulations of bubble cloud dynamics in the focused ultrasound wave.

ditions are used to reduce spurious reflections of waves. The transducer used in the experiment is modeled by an acoustic source uniformly distributed on a portion of spherical surface with an aperture of 30 mm and a radius of 50 mm concentric with the bubble cloud. The axis of the spherical surface is aligned with the axis of symmetry of the coordinates. As shown in figure 4.4, the modeled acoustic source is calibrated by comparing the focal pressure evolution with an experimental measurement. In the simulations of bubble clouds, following the experiment, the peak maximum and negative amplitudes are adjusted to 6.0 and -4.5 MPa, respectively.

The parameters of bubble clouds used in the simulations are summarized on Table 4.1. It is challenging to measure the population and the initial size distribution of nuclei in the experiment. Therefore, we empirically assess the effects of the nuclei population on the resulting bubble cloud dynamics by varying the value of B_0 within a range of $B_0 \in [0.625, 5]$. To assess the effect of polydispersity, for each value of B_0 we simulate monodisperse and polydisperse clouds. For the polydisperse case, the initial radii of bubbles follow a log-normal distribution given as $\ln(R_{b0}/R_{b,ref}) \sim N(0, \sigma^2)$ (Ando et al., 2011), where $R_{b,ref}$ is the most probable bubble size, chosen as $R_{b,ref} = 10$ μm. In the monodisperse and polydisperse cases, we use $\sigma = 0$ and 0.7, respectively. $\sigma = 0.7$ models highly polydisperse bubble clouds. This is in order to obtain an upper bound of the variability in the resulting bubble dynamics due to polydispersity. We neglect fission/break-up of bubbles during the simulations. In order to assess the variability of the bubble cloud dynamics due to the initial reference radius of bubbles, we also simulated monodisperse and polydisperse clouds with $R_{b0,ref} = 5$ μm with various values of $B_0 : B_0 \in [0.625, 5]$. The results did not show a significant difference from cases

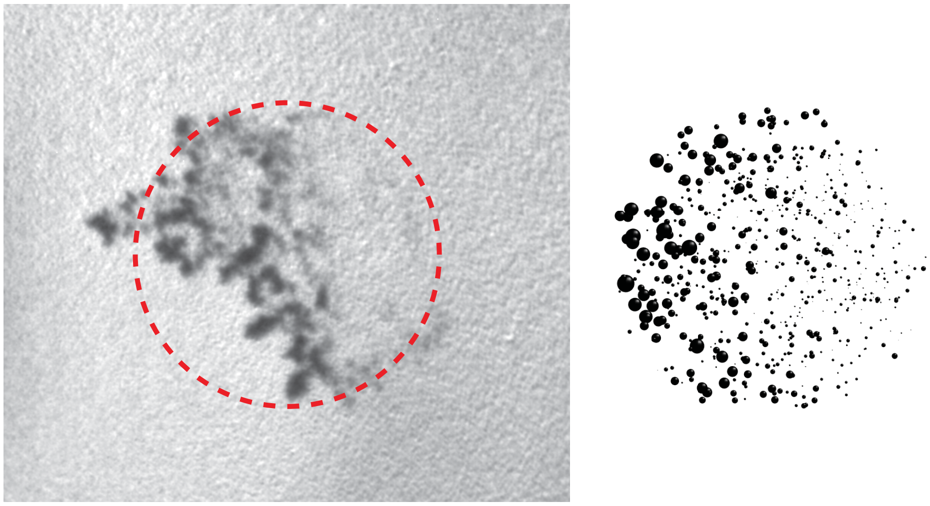

Figure 4.7: Images of the bubble cloud obtained in the experiment and simulation (F8) at $t^* = 13.6$. The red, dotted line shows a circle with radius 2.5 mm.

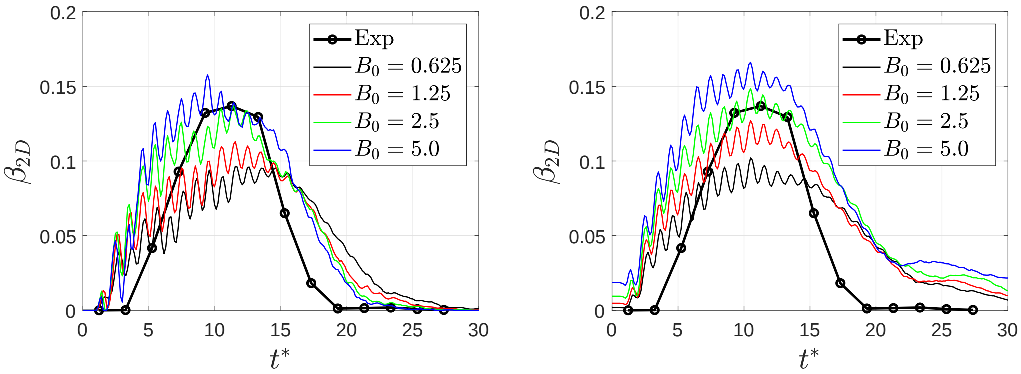

(a)

(b)

Figure 4.8: Comparisons of the evolutions of the two dimensional void fraction of bubbles during the experiment and the simulations.

with $R_{b0,ref} = 10$ μm, thus they are omitted in this paper.

Comparisons with the high-speed image

Figure 4.7 compares the high-speed image (the 7th image of figure 4.5) and the image of bubbles obtained in run-F7 at $t^* = 10$. A similar anisotropic structure is evident in the simulated cloud; the proximal bubbles are larger than the distal bubbles.

Figure 4.8 (a) and (b) compare the evolutions of the two-dimensional void fraction of bubbles in the experiment, and the simulation of initially monodisperse (run

F1-4) and polydisperse (run F5-8) clouds, respectively. The two-dimensional void fraction is obtained as

$$\beta_{2D} = \frac{A}{\pi R_c^2}, \tag{4.9}$$

where A is the area occupied by the bubbles on the two-dimensional images. In all the cases, the projected area steadily grows and reaches its maximum value within the range of 0.1-0.15 at around $t^* = 10 - 15$ then decays. Overall, trends in the evolution of the void fraction are similar between the monodisperse and polydisperse clouds, though the polydisperse clouds present slightly higher peak values than the monodisperse clouds with the same values of B_0. The magnitudes of the slope of the void fraction during the growth and the decay are larger in the experiment than the simulation. The discrepancies could be due to experimental uncertainties, including the size distribution of nuclei in the simulation, non-sphericity of the cloud in the experiment, and the finite resolution and/or the noise of the high-speed images. Nevertheless, the results confirm that the simulated bubble clouds quantitatively reproduce the experimental observation with reasonable accuracy.

For quantification of the anisotropic structure, we compute evolutions of the moments of volume and the kinetic energy in each cloud during the course of simulations. Figure 4.9 shows the result. In all the clouds, the moment of volume oscillates around -0.25 during the passage of the wave until around $t^* = 17$ then grows back to zero. This suggests that the size of the proximal bubbles are larger than the distal bubbles for all t^* and the structural anisotropy is the most significant around at $t^* = 17$. After the initial transient, the moment of kinetic energy oscillates between -0.25 and -0.5 for all t^*. This indicates that the proximal bubbles experience a larger amplitude of pressure excitation and oscillate more actively than the proximal bubbles.

The results above indicate that the bubble dynamics are relatively insensitive to both the population and initial polydispersity of the clouds. Therefore, the anisotropic structure is expected to be observed over a wide range of the nuclei distribution and population.

4.5 Parametric simulations using plane ultrasound waves

Setup

In the setup considered in the previous section, bubbles are forced by the pressure wave with a complex waveform generated by a specific transducer. This hinders further generalization of the obtained results, including the anisotropic structure and

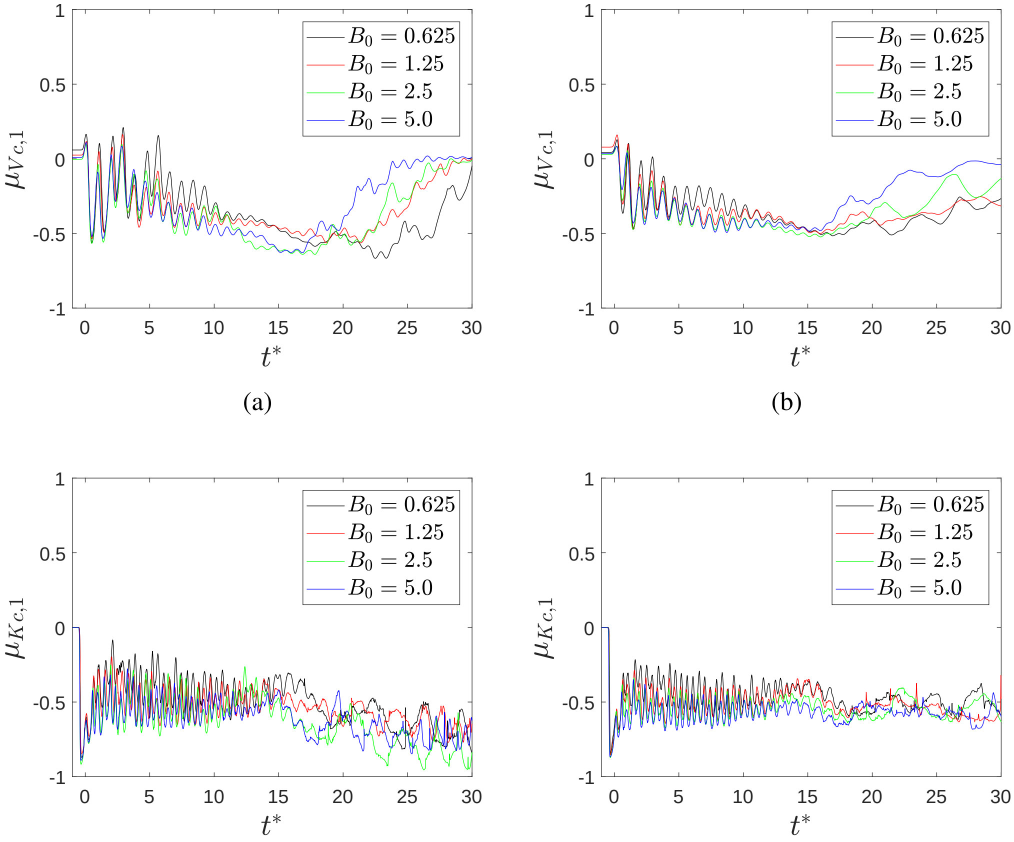

(a) (b)

(c) (d)

Figure 4.9: Evolution of the moment of volume, $\mu_{Vc,1}$, (top row) and the kinetic energy, $\mu_{Kc,1}$, (bottom row) in the simulated clouds. Results of (a,c) monodisperse and (b,d) polydisperse clouds are shown.

the bubble-induced kinetic energy, to the bubble cloud dynamics excited in other geometries of pressure fields. For generalization, analysis using a wider range of parameters, but with a simpler geometry of acoustic source, is desirable. To this end, as an idealized problem, we conduct parametric simulations of bubble cloud dynamics excited by plane ultrasound waves of various amplitudes.

The set of parameters addressed in the simulations is summarized in table 4.2. The radius of clouds and variations of B_0 follows the previous section. It is realistic to assume that the radial distribution of bubbles is polydisperse rather than monodisperse in practical conditions. Thus we assume that the distribution of the initial radius of nuclei follows a log normal distribution with $R_{b0,ref} = 10$ μm and $\sigma = 0.7$, but we expect only small differences with monodisperse clouds in the present cases.

The mesh size follows the previous section. We excite 10 cycles of a plane, sinusoidal

Run	A
A1v[1-4]	$10^{-1.5}$
A2v[1-4]	$10^{-1.0}$
A3v[1-4]	$10^{-0.5}$
A4v[1-4]	1
A5v[1-4]	$10^{0.5}$
A6v[1-4]	10

Table 4.2: List of parameters used in the parametric study. The numbering after the symbol v denotes values of nuclei densities, corresponding to $B_0 = 0.625, 1.25, 2.5, 5$, respectively. For each set of (A, B_0), 5 bubble clouds with distinct initial coordinates of bubbles are simulated.

pressure wave from a source plane located at $x = -20$ mm to the positive x direction, that gives the pressure at the origin, without bubble cloud, of

$$p_a = p_0[1 + H(10 - t^*)A\sin(2\pi t^*)], \tag{4.10}$$

where H is the Heaviside step function. The frequency of the wave is $f = 300$ Hz, thus the wavelength is 4.9 mm and approximately equal to the diameter of the bubble clouds. In order to assess the variability of the bubble cloud dynamics due to spatial distribution of bubbles, with each set of (A, B_0) we simulate $N_s = 5$ clouds with distinct, random spatial distributions of nuclei. In what follows, we denote quantities obtained by averaging N_s bubble clouds with the same set of (A, B_0) as those of *ensemble averaged cloud*. We denote the ensemble average of arbitrary quantity f as

$$f_{ens} = \frac{1}{N_s}\sum_{i=1}^{N_s} f_i, \tag{4.11}$$

where f_i is obtained from i-th realization of the bubble cloud. In the present simulations, $N_s = 5$ is sufficient to obtain ensemble averaged quantities.

Anisotropic structure

Here we analyze the volumetric evolution and the anisotropic structure of the clouds. We begin by looking at the highest amplitude case, $A = 10$, in detail.

Figure 4.10 (a) shows evolutions of the moment of volume of bubble clouds from run A6v during the course of simulation. The moment of volume oscillates between -0.3 and 0 for all values of B_0 after initial transient until $t^* = 10$. After $t^* = 10$ the range of moment takes on a wider spread in values. In order to assess variability

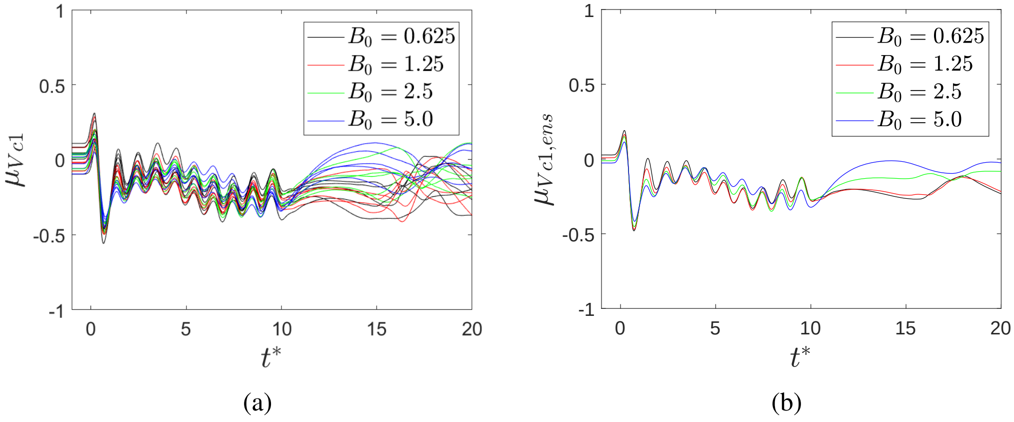

(a) (b)

Figure 4.10: Evolution of the moment of volume with $A = 10$ in (a) each realization (b) ensemble averaged clouds.

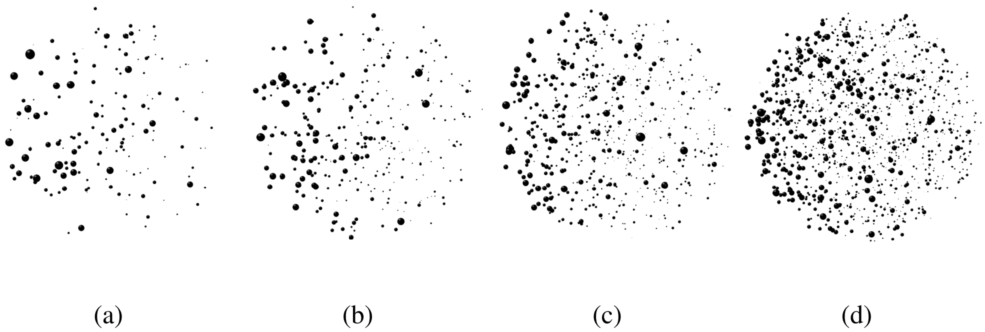

(a) (b) (c) (d)

Figure 4.11: Images of the bubble clouds with various values of B_0 at $t^* = 5.7$ from runs (a) A6v1, (b) A6v2, (c) A6v3, and (d) A6v4.

associated with the random position of bubbles, figure 4.10 (b) shows the same quantities of the ensemble averaged clouds. The similarity of the moments in the two plots indicates small incoherence among the dynamics of bubble clouds of distinct realizations. The clouds share the same anisotropic structure regardless of the initial population and spatial distribution of nuclei.

Figure 4.11 shows images of bubble clouds at $t^* = 5.7$, obtained from one of the realizations from runs A6v1 - A6v4. As expected, the anisotropic structure is similar to the clouds excited by HIFU.

We now consider the effect of varying the excitation amplitude, A. In order to simplify the discussion, we concentrate on the dynamics during the excitation phase where $2 < t^* < 9$, and time-average (denoted by $\overline{(\cdot)}$) the corresponding moments.

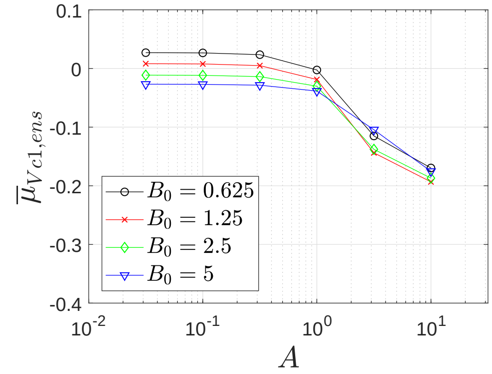

Figure 4.12: Correlations of the time averaged moment of volume of ensemble averaged clouds and the normalized amplitude of the incident wave.

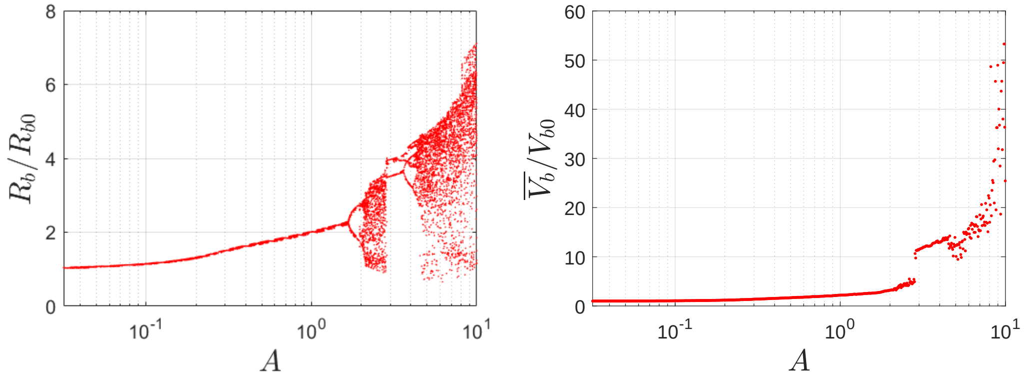

(a)

(b)

Figure 4.13: (a) Bifurcation diagram of the bubble radius and (b) averaged volume of a single, spherical bubble under periodic pressure excitation with varying amplitude.

Figure 4.12 shows the time averaged moment of volume plotted against the normalized amplitude of the incident wave. Regardless of B_0, the moment of volume is small and nearly constant with A up to around $A = 1$. For $A > 1$ the moment decreases, indicating larger anisotropy. Thus anisotropy is observed with high amplitude excitation.

To understand this dependency of the structure on the pressure amplitude, we use the Keller-Miksis equation to examine the nonlinear response of a single, isolated spherical bubble with an initial diameter of 10 μm under periodic far-field pressure excitation with a frequency of 300 kHz. Figure 4.13 (a) shows a bifurcation diagram

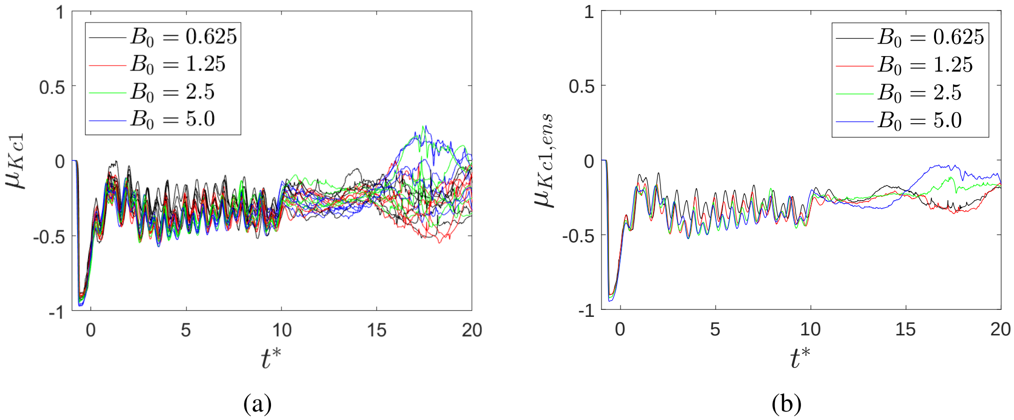

(a) (b)

Figure 4.14: Evolution of the moment of kinetic energy for (a) all the clouds and (b) ensemble averaged clouds.

of the radius of the bubble sampled at every period of forcing pressure with a slowly increasing forcing amplitude within the range addressed in the parametric study. The computed radius monotonically grows with A and experiences a sub-harmonic bifurcation at $A \approx 1.65$, then transits to a chaotic regime with a growing amplitude of radius. The bifurcation diagram in this range of the excitation amplitude was also reported by Preston et al. (2007). At $A \approx 2.85$, the radius returns to a quasi-periodic behavior, and then at $A \approx 4$ it re-transits to a chaotic regime with an amplitude growing with A.

Figure 4.13 (b) shows the time averaged volume of the same bubble during the period of forcing. The growth of the averaged volume follows a similar trend to that of the radius, but with a larger slope. The volume smoothly grows to $\overline{V}_b/V_{b0} \approx 5$ with A then discontinuously grows to $\overline{V}_b/V_{b0} \approx 12$ at $A \approx 2.85$. Then it grows with much faster rate with A, toward $\overline{V}_b/V_{b0} \approx 50$ at $A = 10$. The nonlinear growth of the volume with $A > 1$ corresponds to cavitation.

Figure 4.14 (a) shows the evolution of the moment of kinetic energy of clouds A6v. After the initial transient until $t^* = 10$, the moments of kinetic energy oscillate between -0.5 and 0 around an approximately constant level, after which oscillations with larger amplitudes occur. Figure 4.14 (b) shows the same quantities of the ensemble-averaged clouds. The result is similar to figure 4.14 (a), further confirming that the trend of the moment results from the coherent dynamics of the cloud. The plots indicate that the oscillations of proximal bubbles are more energetic than the distal bubbles during the course of excitation, regardless of the initial nuclei population. Since the moment of volume and the moment of kinetic energy reach quasi-stationary states during the 10 cycles of pressure excitation, increasing the number of cycles of the pressure excitation may not largely affect the structure of the clouds. When the number of cycle is as small as 1, however, the bubble dynamics do not reach the stationary state, as shown in $t^* \in [0, 1]$ in figure 4.14, and the structure may not be observed.

The results of single bubble dynamics in figure 4.13 and the moment of energy in figure 4.14 may explain the mechanism of the anisotropic structure. The bubbles nearest the source are exposed to an incoming pressure wave, while the distal bubbles experience smaller amplitudes of pressure fluctuations due to the scattering of the wave by the proximal bubbles. This results in larger amplitude of oscillations of bubbles locally in the region near the proximal surface of the cloud, seen as the bias in the moment of kinetic energy. With a pressure amplitude larger than $A > 1$, the proximal bubbles can grow to much larger radius than the distal bubbles due to local cavitation, which results in the bias in the center of volume, and becomes visible as the anisotropic structure.

Dynamic cloud interaction parameter

In order to further quantify the bubble cloud dynamics, we seek to generalize the definition of the cloud interaction parameter introduced by DB. The critical difference in the bubble cloud dynamics in the present study and those considered by DB lies in the wavelength and the amplitude of the pressure excitation. As discussed in § 4.3, the original interaction parameter can be interpreted as a scaling parameter of the global kinetic energy of liquid induced by a small amplitude oscillations of bubble cluster under weak pressure excitation with long wavelength. Meanwhile, in the bubble clouds considered in the present study, the wavelength is as small as the size of a cloud. Due to the strong amplitude of the pressure, bubbles experience cavitation growth and their radii can deviate from their initial values. The radius of bubbles can also vary in space.

Figure 4.15 shows the evolutions of the spatial mean of the radius of bubbles in the cloud with $B_0 = 1.25$, normalized by its initial value, with various values of the excitation amplitude: $A = [10^{-0.5}, 1.0, 10^{0.5}, 10]$. For $A > 1$, the mean radius grows rapidly on arrival of the wave, then oscillates around an approximately constant value larger than 1 until $t^* = 10$, while with $A < 1$ the mean radius oscillates around 1. After $t^* > 10$ the radius decays to the initial value in all cases. This indicates

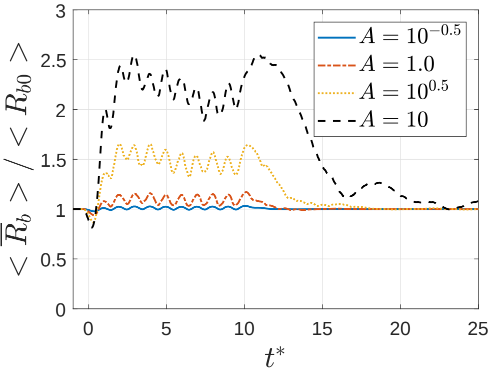

Figure 4.15: Evolution of the mean radius of bubbles in the cloud.

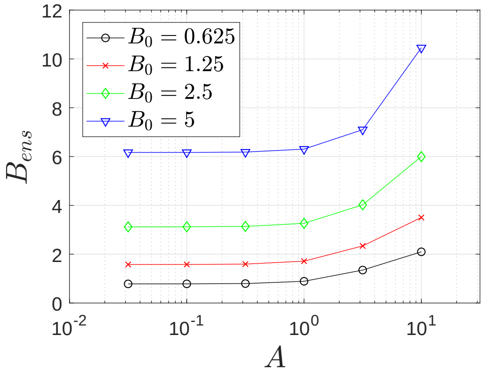

Figure 4.16: Dynamic interaction parameter plotted against the amplitude of pressure excitation for various values of B_0.

that the spatial mean of the bubble radius oscillates around their quasi-stationary equilibrium whose value is unique to the pressure amplitude during the course of excitation.

Motivated by this result, we extend the definition of the cloud interaction parameter as

$$B = \frac{N_b < \overline{R}_b >}{R_{c,L}}, \tag{4.12}$$

where $\overline{R}_b$ is the time averaged radius of bubble during the pressure excitation. Hereafter we denote this parameter as *dynamic cloud interaction parameter*. A detailed discussion motivating the specific form of B is given in appendix B.

In figure 4.16, we plot the average value of B (over the ensemble) obtained for all the runs in Table 1. For all the values of B_0, B monotonically grows and deviates from B_0 for $A > 1$. This is due to the deviation of $< \overline{R}_b >$ from $R_{b,ref}$ and thus

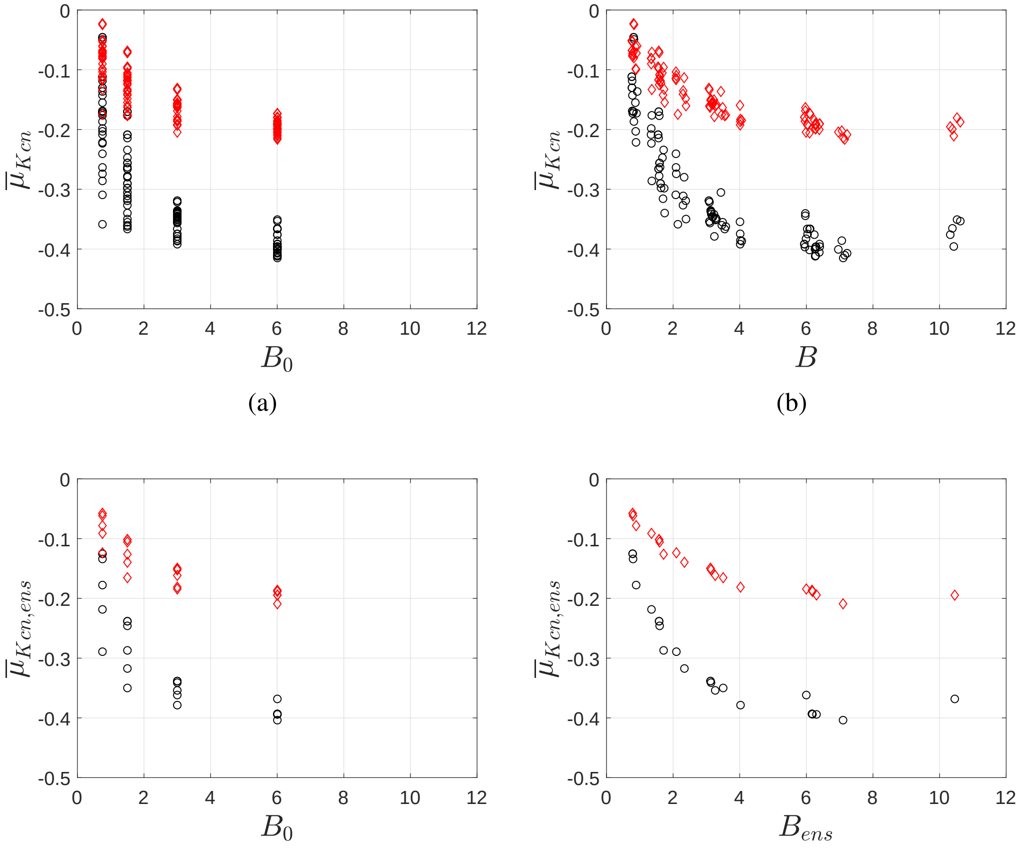

(a) (b)

(c) (d)

Figure 4.17: Scattered plots of the time averaged moments of kinetic energy against B_0 and B. The top row show all realizations while the bottom row shows the ensemble-averaged values. Circle and diamond denote the first and the third moments, respectively.

can be associated with the cavitation growth of the mean bubble radius in the cloud shown in figure 4.16 with $A > 1$.

Scaling of the moment of kinetic energy

The dynamic interaction parameter is proposed as an appropriate scaling parameter for bubble cloud dynamics excited in the short wavelength regime. In this section, to examine the extent to which B controls the dynamics, we correlate the moment of kinetic energy against both B and the original cloud interaction parameter, B_0, and compare the results.

Figure 4.17(a) and (b) show scatter plots of the time-averaged, first and third moments of kinetic energy against B_0 and B, respectively. The 1st and 3rd moments show negative correlations against both B_0 and B, while the data points are vertically more spread against B_0 than against B. The dynamic parameter does a somewhat better job of collapsing the dynamics than the original one. However, once we ensemble-average the data in figure 16 (c) and (d), we see that much of the variation is associated with the randomized positions of the bubbles, and, in general, the dynamic interaction parameter collapses the moment of kinetic energy of the clouds. This confirms that the moments of kinetic energy can been seen as monotonic, decreasing functions of B. Overall, the results indicate that B is a more appropriate parameter to scale the moments than B_0. The similarity of figure 4.17 (b) and (d) indicates small variability of the spatial bias in the energy due to initial spatial distribution of bubbles.

The moments in figure 4.17 (d) approach zero for small B, which confirms that in the limit of $B = 0$ inter-bubble interactions are negligible and the resulting spatial bias in the mean kinetic energy is statistically zero, since bubbles experience the same amplitude of pressure excitation at any location in the cloud. The plots also indicate that as B increases, the slope of the curve monotonically decreases and thus the moment saturates. This indicates that the distribution of energetic bubbles in the cloud becomes more localized in the proximal side of the cloud with increasing the pressure amplitude, while the magnitude of energy localization eventually becomes invariant to the amplitude.

Overall, the results of the parametric simulation further elucidate the underlying mechanism of the anisotropic structure. When the inter-bubble interaction becomes dominant, the energy localization occurs to the cloud, and this happens regardless of the amplitude of pressure excitation. Meanwhile, the anisotropic structure becomes visible only when the energetic, proximal bubbles cavitate and reach a large radius is a nonlinear function of the amplitude of pressure excitation. It is notable that, in fact, the moment of volume is not collapsed by the dynamic cloud interaction parameter. Figure 4.18 shows scatter plots of the time-averaged moment of volume against the dynamic cloud interaction parameter. For the entire range of B, the moment is scattered between -0.3 and 0.1 for both all realizations and the ensemble-averaged values.

Scaling of the far-field, bubble-scattered acoustics

Given the successful scaling of the moments of kinetic energy in terms of the dynamic interaction parameter, we are motivated to explore scaling of the far-field,

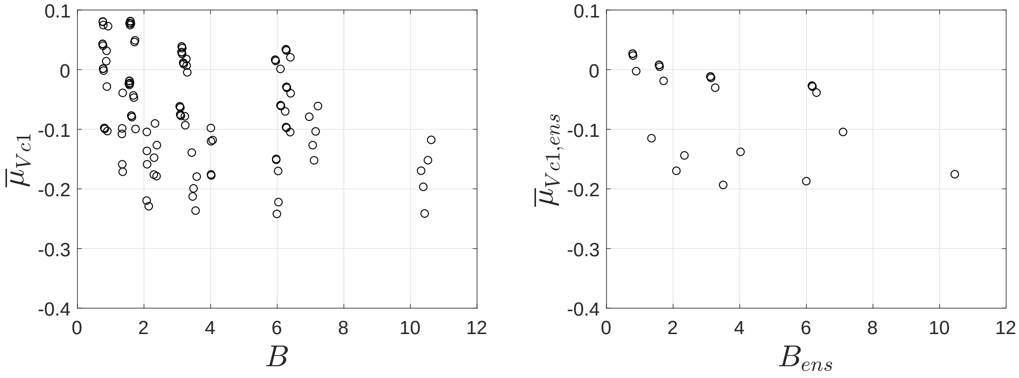

(a) (b)

Figure 4.18: Scattered plots of the time averaged moments of volume against B. (a) shows all realizations while (b) shows the ensemble-averaged values.

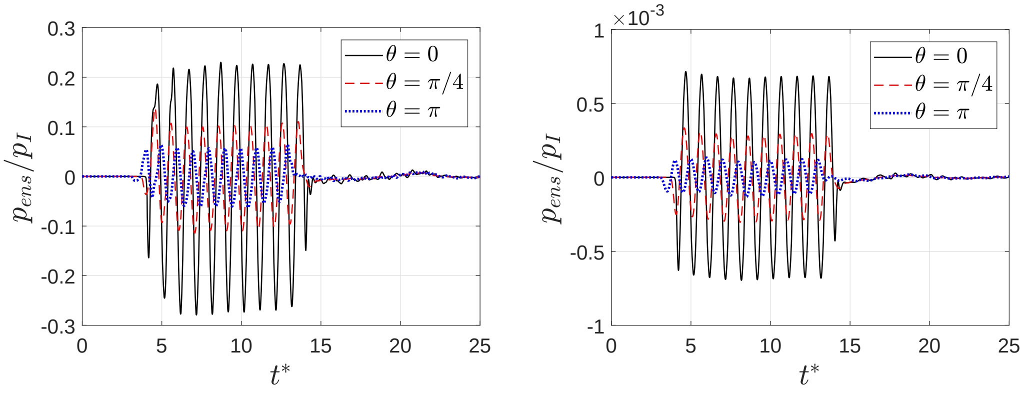

(a) (b)

Figure 4.19: Evolution of the scattered pressure field at a distance $r = 8R_c$ from ensemble averaged clouds from runs (a) A6v4 and (b) A1v1.

bubble-scattered acoustics that result from the bubble cloud dynamics.

Figure 4.19 shows the evolution of the far-field sound at different angles to the direction of incident radiation. The pressure has been normalized by the amplitude of the incident wave. These are plotted for two cases: figure 4.19 (a) shows the densest cloud excited by the highest amplitude wave (thus obtaining the largest value of B), while figure 4.19 (b) shows the most dilute cloud with the lowest amplitude of excitation (lowest value of B). The scattered pressure shows sinusoidal oscillations at a retarded time associated with the incident wave scattered to the sampling location.

The amplitude of the scattered pressure from the dense cloud is an order of magnitude larger than than the dilute one for all t^*. The small, rapid fluctuations at large t^*

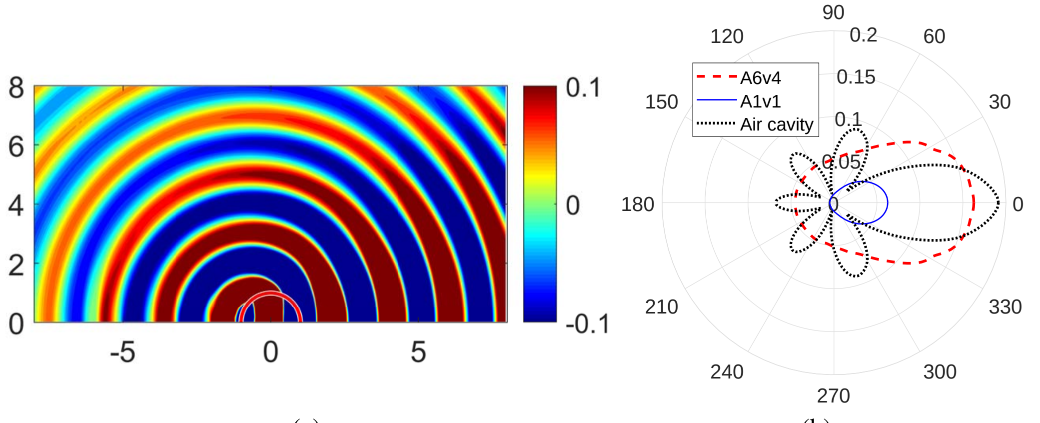

(a) (b)

Figure 4.20: (a) Contours of the scattered pressure field at $t^* = 9.6$, normalized by the amplitude of the incident wave, obtained from run A6v4. The length unit is $R_c = 2.5$ mm. (b) Polar plots of the root-mean-square pressure sampled on spherical surface with $r/R_c = 8$. Results from runs A6v4 and A1v1 are compared to the scattering of a single spherical air bubble of the same size as the cloud.

are due to the bubble oscillations after the passage of the incident wave. The small amplitude of these fluctuations indicate the absence of a strong, coherent cloud collapse.

Figure 4.20 (a) shows an contour plot of the bubble-scattered component of the pressure field at $t^* = 9.6$ from the dense cloud. The scattered component is obtained by subtracting the contribution of the incident pressure wave from the total pressure field. The scattered wave propagates radially outward from the bubble cloud. Figure 4.20 (b) shows a polar plot of the scattered waves from both clouds averaged over the period of direct scattering. The linear scattering from a single spherical air cavity with the same radius as the clouds is also shown for reference. With both clouds, scattering is dominant over angles in the forward direction. The amplitude of scattering is larger at all angles from the dense cloud than the dilute one.

Figure 4.21 is the analog to figure 4.17 but with the root-mean-square pressure plotted versus the original and dynamic cloud interaction parameters. Shown by the different colors are the 3 scattering angles considered in figure 4.19. The scattered pressure shows positive correlations with both B_0 and B. The data points are widely spread against B_0, but collapse better with B. As was the case with the kinetic energy moment, ensemble averaging of the clouds remove additional scatter associated with the randomized bubble positions and distribution. Overall, the results confirm that

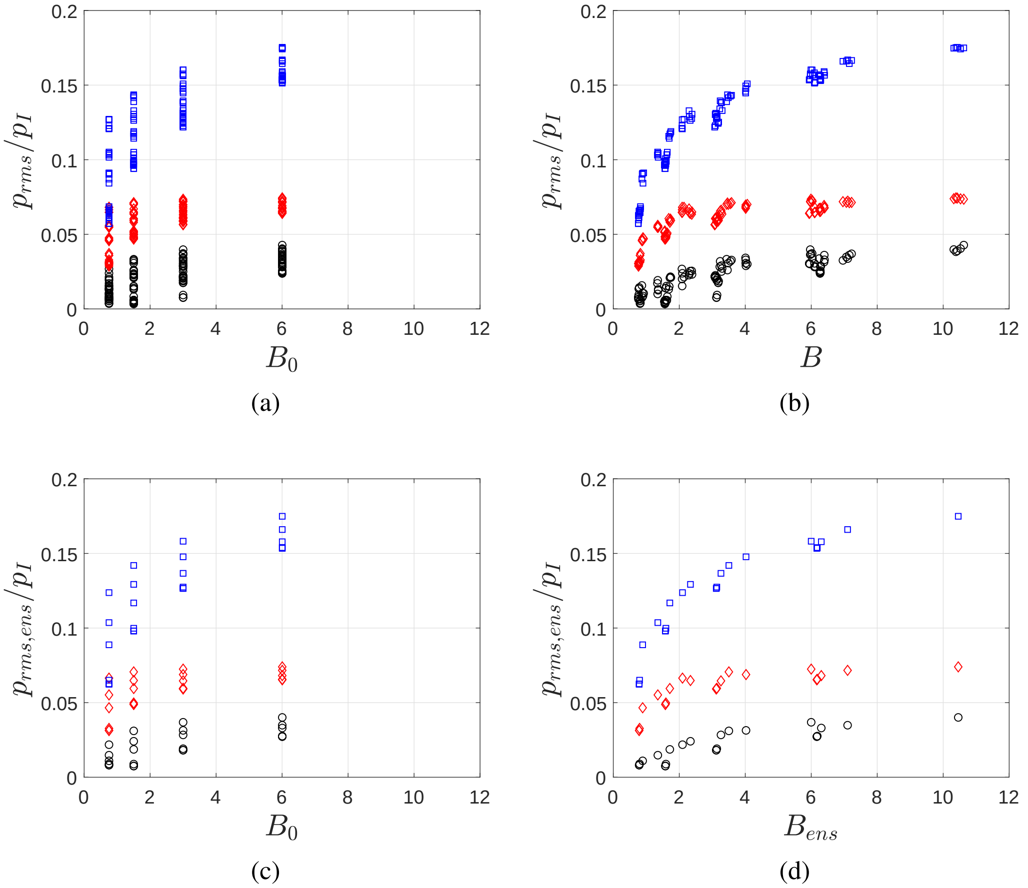

Figure 4.21: Scatter plots of the root-mean-square pressure against B_0 and B at various angles. The top row show all realizations while the bottom row shows the ensemble-averaged values. Circle, diamond, and square denote $\theta = 0$, $\theta = \pi/4$, and $\theta = \pi$, respectively

the proposed interaction parameter scales the amplitude of the bubble-scattered acoustics better than the original parameter.

The polar plots shown in figure 4.20 may help explain the saturation of both the moments of kinetic energy and the amplitude of bubble-scattered acoustics with a large value of the dynamics interaction parameter. Due to the large mismatch in the acoustic impedance across the air-water interface, a cavity can scatter the most portion of the incident wave energy. The dense cloud gives a similar magnitude of scattering as a single large bubble. A subsequent increase in either the excitation amplitude or cloud volume fraction (thus increasing B), yields no further effect; the scattered acoustics saturate at a level similar to a single bubble of the cloud dimension. The smaller directionality of the scattered acoustics by the cloud than

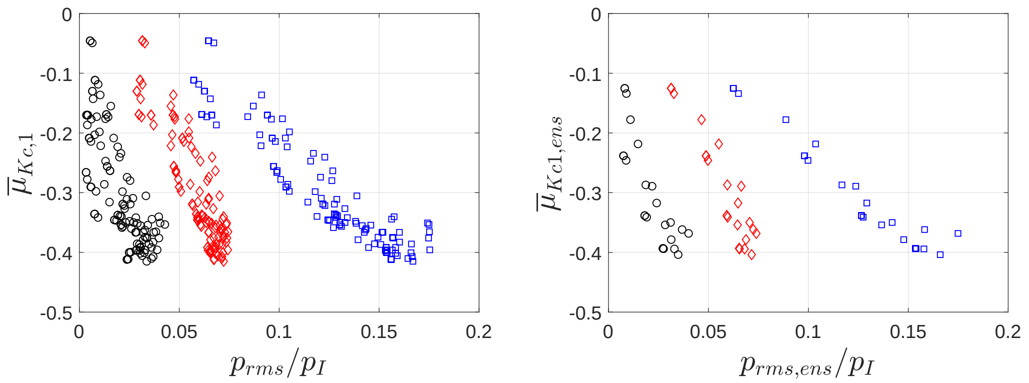

(a)	(b)

Figure 4.22: Scatter plots of the moments of kinetic energy against p_{rms} for (a) all clouds and (b) ensemble averaged clouds. Symbols follow figure 4.21

by the air cavity is associated with the spatially random distributions of bubbles. In multiple scattering theory, scatters with a random, disordered distribution may act as a rough surface and result in randomized angles of scattering of the incoming wave, compared to a smooth surface like that of the air cavity (Ishimaru, 1978).

Overall, it has been shown that the dynamic interaction parameter scales both the amplitude of the scattered acoustic field, as well as the moment of kinetic energy. Furthermore, this indicates direct correlations between the far-field acoustics and the moment. Figure 4.22 (a) and (b) show data for all clouds considered at the 3 observer angles, with and without ensemble averaging, resepectively. For applications, the result indicates that the measurement of the far-field, bubble-scattered pressure waves can be used as a surrogate for the magnitude of the energy localization in the bubble cloud as well as a means to estimate the value of B.

4.6 Implications for cavitation in lithotripsy

As the central application and motivation of the present study, it is worth discussing implications of the present results of numerical experiments to HIFU-based lithotripsy.

In ESWL, bubbles in a cloud experience a nearly identical amplitude of pressure excitation during the passage of the tensile component of the wave since the tensile tail typically has a much larger width than the cloud size. The dynamics of the bubble cloud consist of spherically symmetric structures, similar to what was shown in figure 4.1. The inward-propagating shockwave causes violent cloud collapse, that

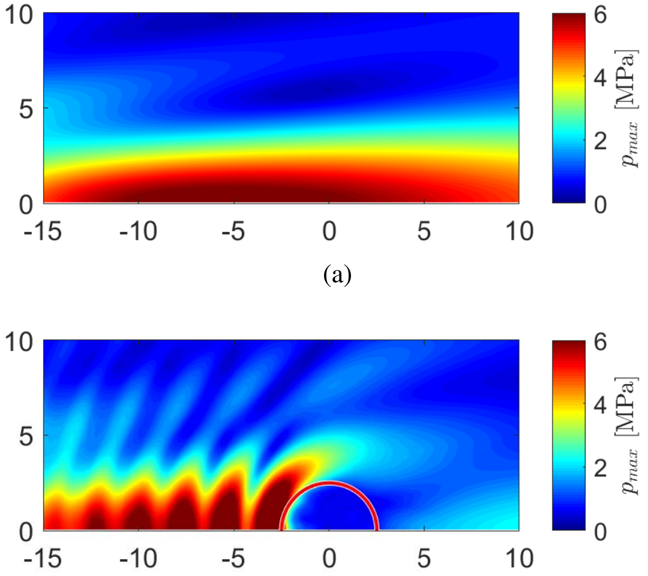

(a)

(b)

Figure 4.23: Contours of the maximum pressure over the course of the simulations (a) without and (b) with the bubble cloud from run F8. The length unit is mm.

results in erosion of surrounding materials. This injurious effect has been seen as a major disadvantage of ESWL (McAteer et al., 2005; Bailey et al., 2006).

The use of HIFU for lithotripsy has been proposed as an alternative to ESWL due to their potentials for safer and more efficient stone comminution (Ikeda, S. Yoshizawa, Masataka, et al., 2006; Shin Yoshizawa et al., 2009; Maxwell et al., 2015). Cavitation bubble clouds in the HIFU-based lithoripsy, by contrast to those in ESWL, have a cloud size commensurate with the ultrasound wavelength. The resulting energy localization of the cloud and scattering of the incoming waves identified in the previous sections indicate that the bubble clouds with a size at an order of the incident pressure wavelength can result in strong scattering of the incident wave, with strong implications for HIFU-based lithotripsy.

Figure 4.23 compares contours of the maximum pressure on the cross plane over the course of the simulations with and without the bubble cloud. Without the bubble cloud, the region of high-pressure (>5 MPa) is localized to the focal region of $x \in [-10, 5]$ mm, while with the bubble cloud, the region of high pressure does not penetrate into the cloud except near the proximal surface. This can be interpreted that the energetic proximal bubbles scatter the incoming wave to prevent the wave from penetrating into the cloud and suppress excitation and oscillation of the distal bubbles. There exists *energy shielding* of the distal bubbles by the proximal bubbles.

The small values of the maximum pressure within the cloud shown in figure 4.23 (b) also indicate that strong cloud collapse does not occur during or after passage of the wave. This agrees with the absence of strong acoustic signals from bubble clouds after the passage of an incident plane wave confirmed in the numerical experiment, shown in figure 4.16. The results are reminiscent of a bubble screen (Carstensen and Foldy, 1947; Commander and Prosperetti, 1989) that provides a similar shielding effect.

In practical conditions of HIFU-based lithotripsy, cavitation bubble clouds can be nucleated on the surface of a kidney stone. It can be conjectured that such bubble clouds may have both positive and negative effects on outcomes of the therapy; they can be less injurious due to the absence of violent cloud collapse, but they could reduce lower the efficacy of stone comminution by scattering the incident radiation. Meanwhile, it is apparent that a presence of kidney stones may complicate the resulting bubble cloud dynamics. For instance, non-spherical bubble collapse may occur on the surface of a stone to cause erosion (Tomita and Shima, 1986; Johnsen and Colonius, 2009), an effect not considered in the present study. For future research, simulations of bubble cloud dynamics in the presence of a stone are desirable.

4.7 Summary

We investigated the dynamics of cavitation bubble clouds excited by strong ultrasound waves, in a regime where the cloud size is similar to the ultrasound wavelength. In a first set of simulations, we excite bubble clouds by a focused ultrasound wave to mimic the laboratory setup of HIFU-based lithtoripsy. An anisotropic cloud structure was observed in both experiments and simulations. The proximal bubbles grow to larger radius than the distal bubbles. In a second series of simulations, we elucidated the underlying mechanisms leading to the anisotropy of the observed structure and dynamics. In these simulations, we varied the amplitude of (plane-wave) excitation and the number density of bubbles, and we considered an ensemble of five runs for each case with different locations and populations of bubbles. Based on the kinetic energy of liquid induced by oscillations of a bubble cluster, we proposed a new scaling parameter, namely a dynamic cloud interaction parameter, that scales the observed anisotropy and dynamics. The parameter is generalized from the cloud interaction parameter introduced by d'Agostino and Brennen (1989) for linearized bubble cloud dynamics in the long wavelength regime. We likewise showed that the scattered acoustic field collapses with the same dynamic interaction parameter, and thus can serve as a surrogate measure for the extent of energy localization in the cloud.

Chapter Appendices

4.A Local cloud interaction parameter

In this appendix we provide a rationale for defining the dynamic cloud interaction parameter. To treat a bubble cloud in that bubbles experiences non-uniform forcing pressure due to the short wavelength, we introduce the notion of *local* kinetic energy. The local energy is defined as the kinetic energy of liquid induced by bubbles in a spherical region around coordinate $\boldsymbol{x}$ with a radius of $R_{c,L}$ that experiences approximately uniform pressure excitation, namely local-cloud:

$$K_{Local}(\boldsymbol{x}) = 2\pi\rho\left[\sum_{i}^{N_{b,L}} R_i^3\dot{R}_i^2 + \sum_{i}^{N_{b,L}}\sum_{j}^{N_{b,L}} \frac{R_i^2R_j^2\dot{R}_i\dot{R}_j}{r_{i,j}} + O\left(\frac{R^7\dot{R}^2}{r^4}\right)\right] \tag{4.13}$$

$$\sim N_{b,L}R_L^3(\boldsymbol{x})\dot{R}_L^2(\boldsymbol{x})(1 + \frac{N_{b,L}R_L}{R_{c,L}}). \tag{4.14}$$

As discussed in §3, with a strong pressure excitation, the mean bubble radius can largely deviate from its initial value. In case of periodic pressure excitation, a natural choice of R_L can be its time averaged value during the course of excitation:

$$R_L \approx \overline{R}_{b,L}. \tag{4.15}$$

This leads us to define the following *local* cloud interaction parameter:

$$B_L(\boldsymbol{x}) \approx \frac{N_{b,L}\overline{R}_{b,L}(\boldsymbol{x})}{R_{c,L}}. \tag{4.16}$$

The local interaction parameter characterizes the kinetic energy of the *local* cloud. We take a summation of this parameter over all the local clouds:

$$\sum_{i=1}^{N_c} B_L(\boldsymbol{x}) = N_c < B_L >= \frac{N_b < \overline{R}_b >}{R_{c,L}}, \tag{4.17}$$

where $< \cdot >$ denotes the spatial average over the global bubble cloud. By multiplying a factor $R_{c,L}/R_c$, we obtain

$$\frac{N_cR_{c,L}}{R_c} < B_L >= B. \tag{4.18}$$

The relation indicates that if the spatial distribution of B_L in distinct bubble clouds are identical, the clouds also possess the same B and show a similar dynamic

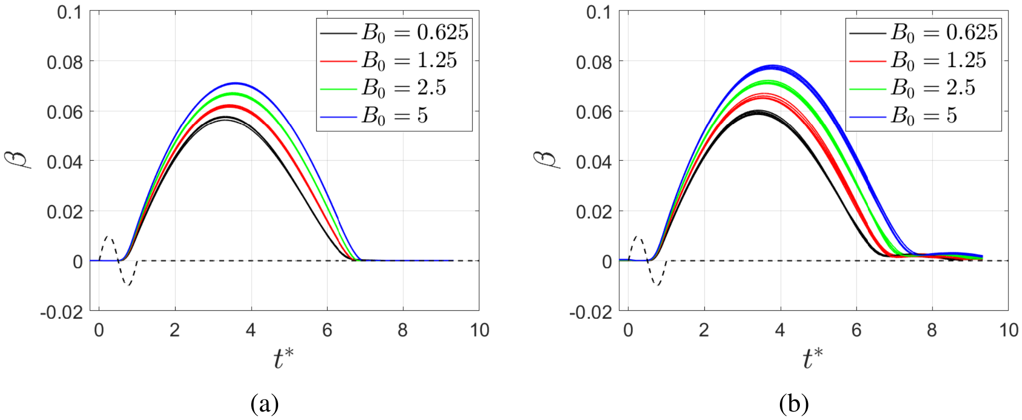

(a)

(b)

Figure 4.24: Evolutions of the void fractions of (a) monodisperse and (b) polydisperse clouds with various values of B_0.

response. Conversely, if distinct clouds possess the same value of B, we could expect a similar spatial distribution of B_L, thus that of the local kinetic energy, though this is in general not a necessary condition.

The scaling of the kinetic energy (4.14) implies that the bubble cloud with larger values of B tends to induce a larger amount of kinetic energy in the liquid, with the same values of $(R_L, \dot{R}_L)$. Conversely, bubble clouds with a larger value of B need smaller values of $(R_L, \dot{R}_L)$ to induce the same amount of kinetic energy. This qualitatively implies that, with the same amplitude of pressure excitation, bubbles in a bubble cloud with a larger B (or B_0) tend to grow less, compared to a single, isolated bubble and bubble clouds with smaller values of B. The suppression of bubble/bubble cloud growth with a large value of B, thus inter-bubble interactions, has been observed in numerical simulation by Wang and Brennen (1999) and in experiment by Bremond et al. (2006), and also qualitatively agrees with the results of the present simulations, in that bubble clouds present smaller differences in their moments compared to differences in their values of B_0 (figs. 4.9, 4.10 and 4.14).

4.B Simulation of the bubble cloud dynamics in the long wavelength regime

In order to simulate the bubble cloud dynamics under far-field pressure exciation, we send 1 cycles of a plane, sinusoidal pressure wave with an amplitude of 1 MPa and a frequency of 50 kHz, thus wavelength of 29.5 mm, from an acoustic source plane to a spherical bubble cloud with a radius of 2.5 mm. The numerical setup, and the population and the initial size distribution of nuclei in the clouds follow section § 4.5.

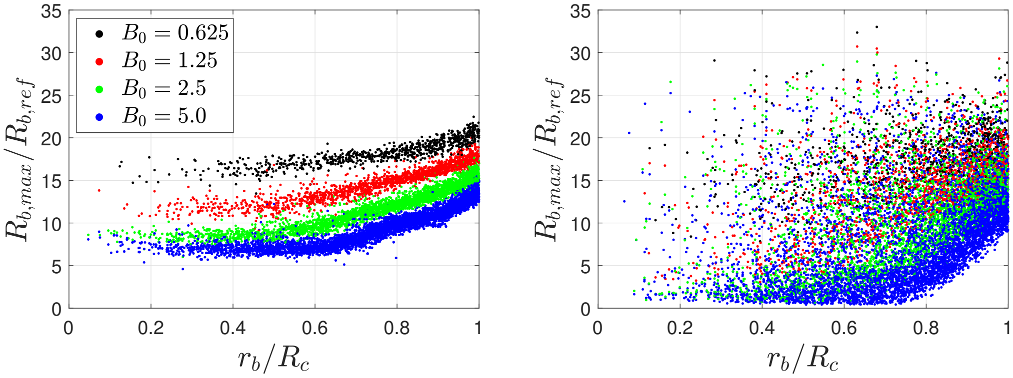

(a) (b)

Figure 4.25: Scatter plot of the maximum bubble radius about the initial bubble.

Figure 4.24 (a) and 4.24 (b) show the evolutions of the void fraction for several different values of B_0 for the monodisperse (case 1) and polydisperse (case 2) clouds, respectively. In all clouds, after the passage of the incident wave, the void fraction steadily grows to reach its maximum value around 0.05 – 0.08 at around $t^* = 3.5 - 4$, then collapses to zero at around $t^* = 7$. Slight rebounds are observed in the clouds in case2 after the collapse. The spread in the curves with the same value of B (same colors), resulting from the randomness of the coordinates of bubbles, is small in both cases. Interestingly, the results of case 1 and 2 do not show significant differences, suggesting that the effect of polydispersity is small. As shown in figure 4.1, the structures of the clouds possess nearly spherical symmetry, as bubbles experience uniform back-ground pressure during the passage of the incident wave due to its long wavelength. At its maximum void fraction, bubbles near the periphery of the cloud are larger than those near the center (figure 4.1 (b)). This can be explained by a shielding of the inner bubbles by the outermost layer; the outer bubbles scatter/absorb the acoustic energy of the incident wave to mitigate its penetration into the center. During the collapse, it is observed that the bubbles near the periphery collapse earlier, followed by the inner bubbles. This inward propagation of the collapse corresponds to the bubble cloud collapse can be associated with the bubbly-shockwaves observed in the previous studies. The geometric center of the collapse is slightly offset to the right from the cloud center of the cloud in the present result. This offset can be explained by the slight delay in the arrival of the incident wave at the right side of the cloud due to the finite wavelength and the sound speed that were not considered in the previous studies.

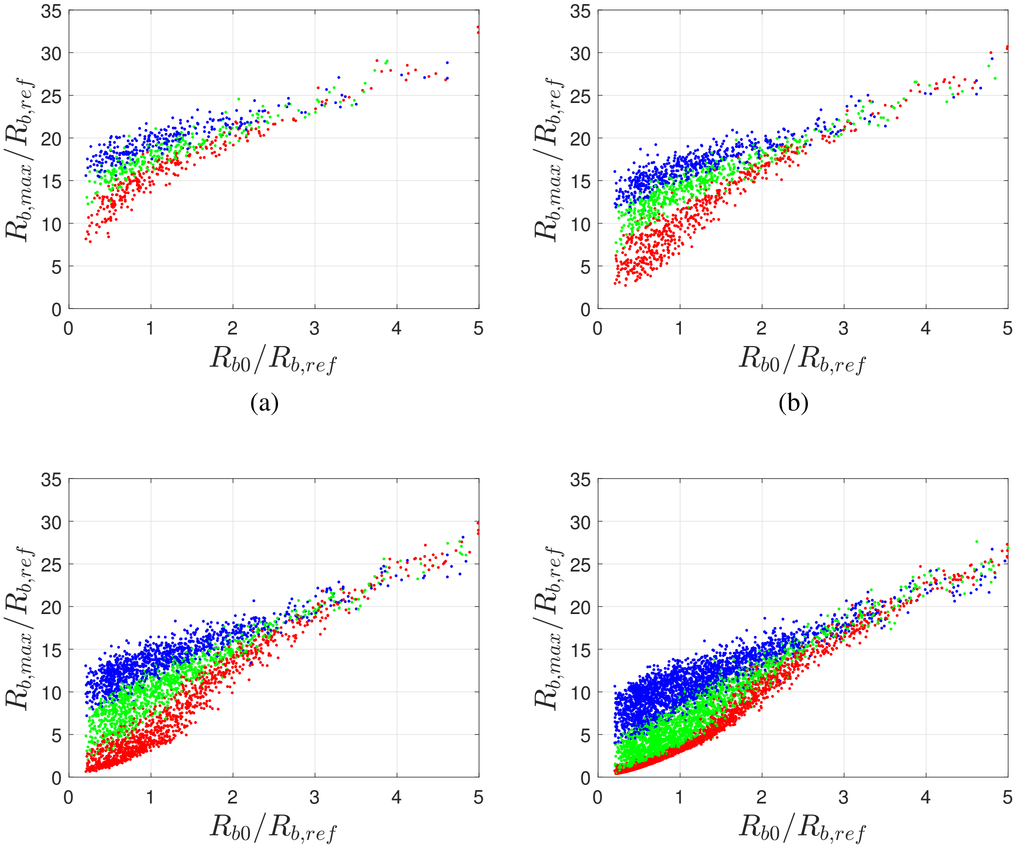

(a) (b)

(c) (d)

Figure 4.26: Scattered plots of the maximum radius of each bubble about its initial radius separately for distinct values of B_0, with distinct colors based on bubble's radial coordinate.

In order to quantify the anisotropy in the growth of bubbles in the cloud, in figure 4.25 we plot the maximum radius of the bubbles as a function of their radial coordinates (distance from the origin) for each value of B_0, for the monodisperse and polydisperse cases, respectively. In the monodisperse case (figure 4.25 (a)), the maximum radius has a clear monotonic, positive correlation with the radial coordinate. The slope of the correlation is increased with B_0, though the values of the radius tend to decrease with B_0. As discussed in § 4.A, this results suggest that with increasing the inter-bubble interaction, the bubble growth is suppressed and anisotropy in the bubble growth is enhanced. In the polydisperse case (figure 4.25 (b)), we do not observe clear correlations except for $B_0 = 5$, indicated by a blue scattered points, due to higher dispersions in the bubble radius.

For a better analysis of the polydisperse clouds, in figure 4.26 we scatter the data points of the maximum radius of each bubble as a function of its initial radius separately for distinct values of B_0, with distinct colors based on bubble's radial coordinate: $r/R_c \in [0, 0.7]$ (center); $r/R_c \in [0.7, 0.87]$ (mid-shell); $r/R_c \in [0.87, 1.0]$ (outer shell). Note that these three regions have approximately the same volume. The results show that for each value of B_0, the bubbles attain the largest radii in the outer shell, followed by the middle shell. The maximum radius tends to decrease by increasing B_0. Thus, it is indicated that the correlations observed in the monodisperse clouds hold true in the polydisperse case.

Chapter 5

QUANTIFICATION OF THE ENERGY SHIELDING OF KIDNEY STONES BY CAVITATION BUBBLE CLOUDS

A part of this chapter is published in the proceedings of The 10th International Symposium on Cavitation (CAV2018).

5.1 Overview

In Chapter 4, it was indicated that bubble clouds nucleated near a kidney stone can cause energy shielding of the stone by scattering incoming ultrasound waves. For application to BWL, it is further informative to quantify the energy shielding. To that aim, in this chapter, experiments and numerical simulations of the dynamics of bubble clouds nucleated on the surface of a stone model under ultrasound radiation are presented. In the experiment, an epoxy stone model is insonified by a burst wave with an amplitude of 7 MPa and a frequency of 340 kHz generated by a focused ultrasound transducer in water. We visualize the evolution of bubble clouds using a high-speed camera and measure the back-scattered acoustics from the bubbles with transducer array elements. In the simulation, we combine numerical methods developed in Chapters 2 and 3 for modeling the interactions among bubbles, the stone, and the burst wave. Simulated evolution of the bubble cloud and bubble scattered acoustics quantitatively agree with the results of the experiment. We vary the initial void fraction and size of bubble cloud to assess the magnitude of the shielding as well as its correlation with the bubble-scattered acoustics. Results of the study indicate that the magnitude of the shielding reaches up to 90% of the total acoustic energy of the incident burst wave. We further discovered a strong correlation between the magnitude of the shielding and the amplitude of the back-scattered acoustics, independent of the initial condition of the cloud. The results of the study can be used to further identify appropriate parameters and improve the efficacy of stone comminution in BWL.

5.2 Experimental setup

Figure 5.1 (a) shows a schematic of the experimental setup. We generate pulses of 10 cycles of a sinusoidal pressure wave with a frequency of 340 kHz and a peak focal pressure of 7.0 MPa from a multi-element array focused transducer with an aperture

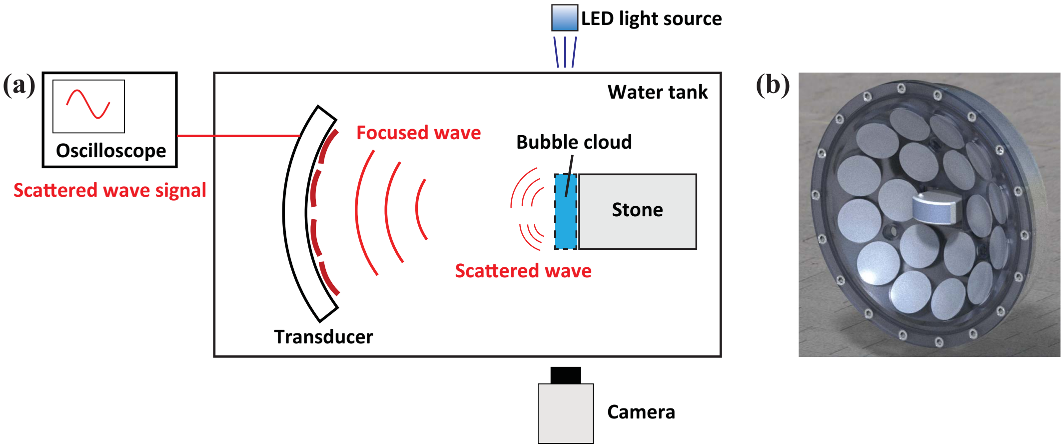

Figure 5.1: (a) Schematic of the experimental setup. (b) Multi-element array medical transducer (same as that modeled in Chapter 2).

of 180 mm and focal length of 150 mm (figure 5.1 (b)) toward a cylindrical shape of epoxy stone model with its axis aligned on the acoustic axis of the transducer. The pulse repetition frequency is 100 Hz. The focal point of the transducer is located at the center of the stone. The height and radius of the stone are 10 and 6.25 mm, respectively. The water is degassed to approximately 65% O_2 saturation to model the environment of the liquid filling the collecting space of the kidney. A high-speed camera captures a thin layer of bubbles forming a cloud nucleated on the proximal base of the stone. We concurrently sample the back-scattered acoustics from the bubble cloud and the stone by using the transducer array elements.

5.3 Simulation setup

In simulations, we formulate the dynamics of the multi-component mixture using the compressible, multi-component, Navier-Stoke equation. We model the stone as an elastic solid with zero shear modulus with a density of 1200 kgm^{-3} and a longitudinal sound speed of 2440 ms^{-1}. The coupled dynamics of the stone and the surrounding water are modeled using an interface capturing method (Perigaud and Saurel, 2005; Coralic and Colonius, 2014). We model the transducer as a portion of a spherical surface with an aperture of 60 mm and a radius of 50 mm with its center located at the origin of $z-r$ axi-symmetric coordinates. We generate burst waves at the modeled surface by using the source term approach developed in Chapter 2. The axis of the cylindrical stone is aligned on the z-axis, with its mid-point located at the origin. For modeling bubbles, we utilize the Eulerian-Lagrangian method developed in Chapter 3. The governing equations are discretized on an axisymmetric grid. The grid size is uniform with a radial and axial width of 100

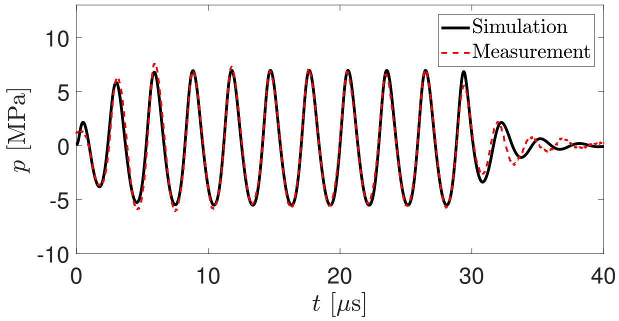

Figure 5.2: Evolution of the focal pressure.

μm in the stone-wave interaction region. We initially distribute spherical bubble nuclei with a radius of 10 μm in the cylindrical region that faces the proximal base of the stone, then track the radial evolution of the bubbles at the sub-grid scale and resolve the bubble-scattered acoustics on the grid. For the parametric study, we run simulations varying the thickness of the bubbly layer, h, and the initial void fraction, β_0, of the cylindrical cloud, within ranges of $h \in [0.25, 1.0]$ mm and $\beta_0 \in [1.0, 8.0] \times 10^{-5}$, respectively. The ranges of the parameters were estimated from preliminary experiments. We capture the evolution of the bubbles and sample the back-scattered acoustics at points on the acoustic source surface corresponding to the angles of the centers of the transducer array elements used in the experiment.

5.4 Results and discussion

Figure 5.2 compares the evolution of the focal pressure during the passage of the burst wave obtained from the experiment and a simulation without the stone. The head of the wave arrives at the focal point at $t = 0$. The simulated waveform and the peak pressure agree well with those of the measurement, except for the small oscillations due to ring down after $t = 30$ μs.

Figure 5.3 compares the evolution of the area occupied by the bubbles projected on a 2D plane, A mm^2, obtained in the experimental visualization and the simulation with $h = 0.75$ mm and $\beta_0 = 1.0 \times 10^{-5}$. Each data point of the measurement is obtained by averaging 440 independent realizations of the bubble clouds. The shaded area corresponds to the standard deviation resulting from the randomness in the clouds. The result of the simulation shows that the cloud experiences a transient growth with rapid oscillations during the passage of the wave, up to about $t = 30$ μs, followed by a smooth decay after the passage of the wave. The result of the measurement cannot capture the oscillations, even though they may be present in the experiments, as the

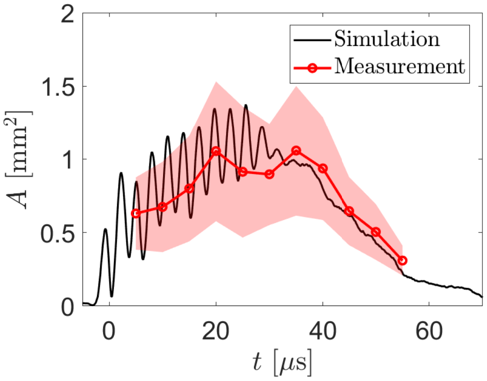

Figure 5.3: Evolution of the projected area of bubble cloud. Result of the simulation with $h = 0.75$ mm and $\beta_0 = 1.0 \times 10^{-5}$ is shown.

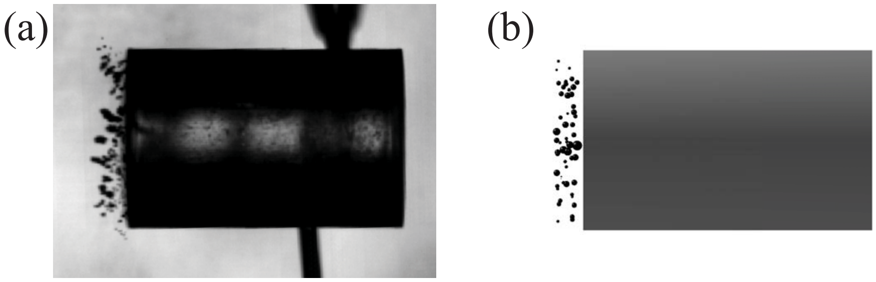

Figure 5.4: Images of representative bubble clouds obtained at $t = 21$ μs in the (a) experiment and (b) simulation.

present sampling frequency was lower than that of the oscillation, while its growing trend until around at $t = 30$ μs and decay after the passage of the wave agree well with the result of the simulation.

Figure 5.4 shows representative images of bubble cloud obtained from the experimental visualization and the simulation at $t = 21$ μs. A layer of dispersed bubbles is present on the proximal base of the stone in both images

Figure 5.5 shows pressure contours at different instants in time during the simulation. A burst wave is generated and focused toward the stone (figure 5.5 (a)). A bubble cloud is excited during the passage of the wave (figure 5.5 (b)). A portion of the wave is scattered back from the bubbles and the stone, and the rest of the wave transmits through the stone and is scattered forward (figure 5.5 (c)). After the passage of the incident wave, weak reverberation of the pressure wave is observed in the stone (figure 5.5 (d)). Strong collapse of bubble cloud is not observed. This may be due to the small void fraction and size of the cloud.

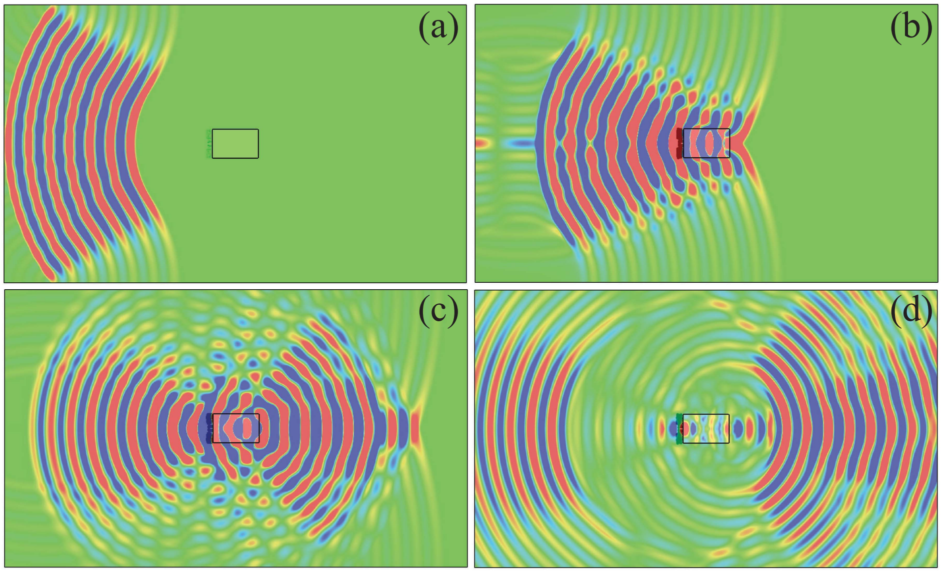

Figure 5.5: Snapshots of the pressure contour during the simulation with $h = 1.0$ mm and $\beta_0 = 1.0 \times 10^{-5}$ at (a) $t = 10$, (b) 20, (c) 30, and (d) 40 μs. Stone and the void fraction of bubbles are indicated with black line and shading, respectively.

In order to quantify the amplitude of the back-scattered acoustics, we compute a cross-correlation based, daylight imaging functional using the acoustic signals sampled in both the experiment and the simulation, following algorithms reported by Garnier and Papanicolaou (2009). Given $u(t, \boldsymbol{x}_i)$, where $i = 1, ..., N_{sensor}$, as a set of signals sampled at coordinates $\boldsymbol{x}_i$ over the time interval $[0, T]$. The cross correlation between signals $u(t, \boldsymbol{x}_i)$ and $u(t, \boldsymbol{x}_j)$ is defined as

$$C_T(\tau, \boldsymbol{x}_j, \boldsymbol{x}_l) = \frac{1}{T} \int_0^T u(t, \boldsymbol{x}_i) u(t + \tau, \boldsymbol{x}_i) dt. \tag{5.1}$$

The imaging functional at coordinate z is defined as:

$$\mathcal{I}(z) = \sum_{j,l=1}^{N_{sensors}} C_T^{sym}(\tau(z, \boldsymbol{x}_l) + \tau(z, \boldsymbol{x}_j), \boldsymbol{x}_j, \boldsymbol{x}_l), \tag{5.2}$$

where

$$C_T^{sym}(\tau, \boldsymbol{x}_j, \boldsymbol{x}_l) = C_T(\tau, \boldsymbol{x}_j, \boldsymbol{x}_l) + C_T(-\tau, \boldsymbol{x}_j, \boldsymbol{x}_l). \tag{5.3}$$

C_T^{sym} is the symmetric component of the cross-correlation. C_T^{sym} is used instead of C_T to remove the influence of the component of signals that are not scattered by the stone and the bubble cloud from the functional. Further details of the algorithms to obtain the functional can be found in Garnier and Papanicolaou (2009).

Figure 5.6 (a) and 5.6 (b) show normalized contours of the imaging functional obtained in the experiment and the simulation. Coordinates with a large value of

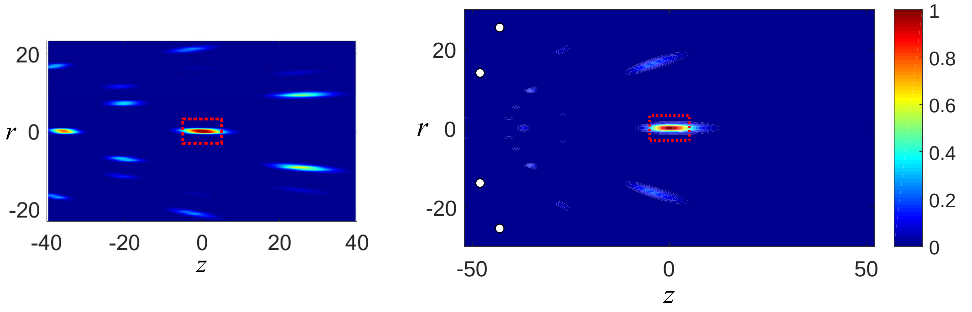

(a)

(b)

Figure 5.6: (a) Normalized contour of the imaging functional obtained from the (a) experiment and (b) simulation. The stone is indicated by a dotted line. The length unit is mm. Sensor locations are indicated by white dots.

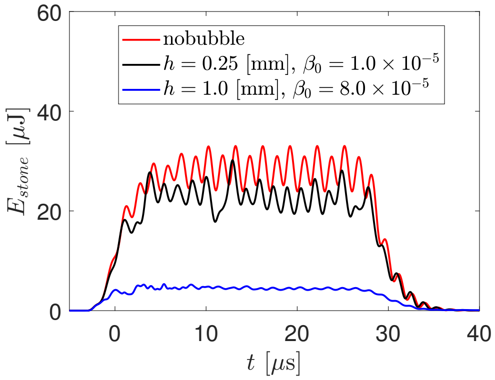

Figure 5.7: Evolution of the kinetic energy in the stone induced by the burst wave.

the imaging functional correspond to estimated locations of the acoustic source. In both plots, a region of a large value of the imaging functional is localized within the area of the stone. This result suggests that the acoustics scattered from the stone (and the bubbles) are captured in both the experiment and the simulation, and their magnitude can be quantified by the imaging functional.

Figure 5.7 shows the evolution of the kinetic energy in the stone induced by the burst wave during three distinct simulation cases: without bubbles, with a thin and dilute cloud (h = 0.25 mm and $\beta_0 = 1.0 \times 10^{-5}$), and with a thick and dense cloud (h = 1.0 mm and $\beta_0 = 8.0 \times 10^{-5}$). In all the cases, the energy steadily grows after arrival of the wave until around at t = 10 μs, then oscillates around a constant value during the passage of the wave until around at t = 30 μs. After the passage of the wave, the

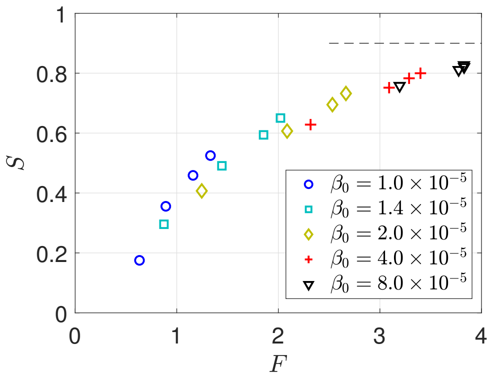

Figure 5.8: Correlation between the shielding factor and the scattering factor. The dotted line indicates $S = 0.9$.

energy steadily decays and reaches zero around at $t = 40$ μs. The energy is highest for all t when there are no bubbles. The energy level is slightly decreased with the thin and dilute cloud, while it is drastically reduced with the thick and dense cloud. This result indicates that the energy shielding by bubbles is enhanced by increasing the thickness and/or the void fraction of the cloud.

To quantify the correlation between the shielding and the scattered acoustics, in figure 5.8 (d) we plot the shielding factor S as a function of the scattering factor F. The shielding factor is defined as

$$S = 1 - \frac{P}{P_{\text{ref}}}, \tag{5.4}$$

where P is the total work done by the acoustic energy to the stone during each simulation: $P = \int E_{\text{stone}} dt$. P_{ref} is the reference value of P obtained in the case without bubbles. Note that $S = 0$ and $S = 1$ indicates no shielding and perfect shielding (no energy transmission into the stone), respectively. The scattering factor is defined as

$$F = \frac{\max[\mathcal{I}]}{\max[\mathcal{I}_{ref}]}, \tag{5.5}$$

where $\mathcal{I}_{ref}$ is the reference value of imaging functional obtained in the case without bubbles. F quantifies the amplification of the scattered acoustics due to bubbles compared to the case without bubble. Note that $F = 1$ indicates no effect of the scattering due to bubbles. The maximum value of the shielding factor in the plot is approximately 0.9, indicating that up to 90% of the total energy of the incident burst wave can be absorbed/scattered by bubbles that otherwise transmits into the stone. Interestingly, the plot also indicates a strong correlation between the shielding factor and the maximum imaging functional within the global range of the shielding factor, independent of the initial condition of bubbles. This correlation suggests that the scattered acoustics can be directly used to estimate the magnitude of the shielding regardless of the bubble dynamics, at least within the range of parameters of bubble cloud addressed in the simulations.

In the present study, single realization of layer of initially monodisperse bubbles is simulated for each set of the thickness and void fraction of the bubble layer. Given the relatively small influence of the spatial distribution of bubbles and polydispersity of bubbles on the dynamics of spherical bubble clouds in the parametric simulation studied in Chapter 4, the effects of the spatial randomness and polydispersity of bubble nuclei are expected to be likewise small in the present case.

5.5 Summary

In this chapter, the energy shielding of kidney stones by a bubble cloud nucleated on the stone surface during the passage of a burst wave was quantified through a combined experimental and numerical approach. Simulated evolution of the bubble cloud and the bubble-scattered acoustics showed quantitative agreements with the results of experimental high-speed imaging and acoustic measurements. The numerical results revealed that the magnitude of the energy shielding by a thin layer of bubble cloud can reach up to 90% of the total energy of the burst wave, indicating a large potential loss of efficacy in the treatment of BWL due to cloud cavitation. Furthermore, we discovered a strong correlation between the magnitude of the shielding and the amplitude of the back-scattered acoustics. This correlation could be used, for example, for quantification of the magnitude of the shielding in a human body by ultrasound imaging in real time in BWL and adjusting the wave parameters to control the shielding.

Chapter 6

CONCLUDING REMARKS

6.1 Conclusions

This thesis has reported a series of studies on modeling, numerical simulation and experimental analysis of the dynamics of cavitation bubble clouds excited by strong ultrasound waves for quantification of the effects of cavitation on outcomes of burst wave lithotripsy.

In Chapter 2 and 3, an acoustic source model and an Eulerian-Lagrangian method were developed as numerical tools for simulation of focused ultrasound generated by medical transducer and cloud cavitation excited by the ultrasound, respectively. For better comparisons with experiment and engineering prediction, the numerical model and the method were designed to mimic and visualize the physical process of acoustic cavitation in BWL; ultrasound generation at vibrating piezo-ceramic arrays of the transducer are modeled, and the dynamics of individual bubbles are tracked and visualized. In the Eulerian-Lagrangian method, special emphasis was placed upon development of sub-grid modeling for accurate simulation of bubble dynamics and upon reduced order models for speedup of simulations. The set of numerical tools were capable of simulating multi-scale dynamics of cloud cavitation, including the oscillations of individual bubbles and strong bubble-scattered acoustic, coherent dynamics of bubbles in a cloud, with a high accuracy that was not attainable by existing methods. Excitation of cloud cavitation by an ultrasound wave was demonstrated in the regime where the cloud size becomes close to the ultrasound wavelength. A non-trivial anisotropic structure was identified in the cloud, in that the proximal bubbles grow to larger radius than the distal bubbles.

In Chapter 4, using the numerical framework developed in the previous chapters, bubble cloud dynamics in an intense ultrasound field were investigated to elucidate the aniostopic structure and the associated physics. Experimental high-speed imaging and a set of numerical simulations were used to further quantify the anisotropic structure of the cloud. A scaling parameter was proposed to characterize the non-linear dynamics of bubble clouds. The parameter generalizes the cloud interaction parameter introduced by d'Agostino and Brennen (1989) for linearized dynamics of bubble clouds in the long wavelength regime. The following are identified through the simulation: The kinetic energy of liquid induced by bubbles becomes larger in the proximal side than in the distal side with the increase of the parameter, regardless of the nuclei population, the energetic bubbles are locally cavitated under a large amplitude of pressure excitation and this results in the anisotropic structure. The amplitude of the far-field, bubble scattered acoustics is likewise scaled with the proposed parameter, and thus potentially lowering both the comminution efficiency but also associated tissue damage in BWL as compared to ESWL. The numerical results further indicated that the short wavelength regime of bubble clouds may not experience a violent, coherent collapse, and that a large portion of the incident ultrasound is scattered, and thus can lower the efficiency in stone comminution when nucleated near a stone during BWL.

In chapter 5, a combined experimental and numerical study was conducted to quantify the energy shielding of a kidney stone caused by cloud cavitation. In the experiment, a cylindrical stone model was immersed in water and exposed to a burst wave, in that a thin layer of bubble clouds is nucleated on the surface of the stone. Interactions among the burst wave, cavitation bubbles and the stone model were simulated using the numerical tools. Results of the simulation revealed that up to 90% of the wave energy was scattered by the bubble cloud. The simulated evolution of the bubble cloud and the measured back-scattered acoustics agreed with experimental measurements. A strong correlation was identified between the amplitude of the scattered waves and the magnitude of the energy shielding, indicating that the shielding can be monitored by measuring the scattered acoustics.

Cavitation or no cavitation

At the end of this thesis, it is worth discussing comparisons of BWL and another prototype method of HIFU-based lithotripsy. The lithotripsy aims to actively take advantage of cavitation damage induced by collapse of bubble cloud for efficient stone comminution by combining high frequency ultrasound of $O(1)$ MHz that induces cavitation bubble clouds and low frequency ultrasound of $O(100)$ kHz that causes the clouds to collapse (Ikeda, S. Yoshizawa, Masataka, et al., 2006; Ikeda, S. Yoshizawa, Koizumi, et al., 2016). It has been shown that the combination of high and low frequencies, denoted as cavitation control [C-C] waveform, is more effective in stone comminution than using only high or low frequency in experiment *in vitro*.

The method of lithotripsy is seemingly conflicting with the philosophy of BWL that aims to avoid cavitation to maximize the energy transmission into the stone and to minimize potential injury. However, from a larger point of view, both methods seek to improve SWL by using HIFU and could be compatible with each other.

The conclusion of chapter 5 in the present thesis revealed the strong energy shielding as another negative effect of cavitation in BWL, other than potential injury. As previously discussed, in the practical condition of lithotripsy in that stones are surrounded by a liquid with higher gas concentration than idealized experiment (Maxwell et al., 2015), it is difficult to completely suppress cavitation. Such cavitation bubbles could be to some extent used to enhance stone comminution by sending a longer wavelength of burst wave following the strategy of C-C waveform, without sacrificing the advantage of BWL.

6.2 Recommendations for future work

Modeling and numerical methods

The Eulerian-Lagrangian method developed in Chapter 3 treats spherical bubbles. In reality, bubbles experience non-spherical deformations and fission/break-up. Though simulations presented in this thesis show quantitative agreement with experiments, for more accurate modeling of bubble dynamics, such non-trivial dynamics of bubbles may be included. The method was validated considering problems of acoustic cavitation with a uniform, irrotational back-ground flow field. For applications to cavitating flow problems in that the non-uniform, fluctuating back-ground flows with non-zero vorticity can interact with the bubble dynamics, further verifying/improving the sub-grid models would be desirable, for example, by considering translational motions of bubbles induced by hydrodynamics forces (Maeda, Date, et al., 2013).

Violent non-spherical bubble collapse may cause cavitation erosion of a stone (Tomita and Shima, 1986; Johnsen and Colonius, 2009). Such effects of bubbles are not modeled in the simulation shown in Chapter 5. It remains unknown if such cavitation erosion contributes to stone comminution in BWL. For further quantification of the erosion, modeling the fluid-structure interaction would be desirable, including elasticity, plasticity, and fracture mechanics of the stone.

Feedback control of burst wave lithotripsy

The correlations between the scattered acoustics and the magnitude of the energy shielding (scattering-shielding correlation) obtained in Chapter 5 can be used to directly monitor cavitation and estimate the magnitude of the shielding by sensing ultrasound in real time during the treatment of BWL. This may realize real-time control of cavitation by modifying the pressure waveform and/or PRF, to optimize the efficacy of stone comminution by suppressing the shielding below a certain threshold. Meanwhile, a wide range of physical parameters and uncertainties are involved with the actual treatment of lithotripsy, including the anatomical structure, stone shape and composition. In this thesis, the scattering-shielding correlation was obtained for a particular combination of the waveform and a model stone with a simple geometry *in vitro*. For realization of the feedback system, a database of the shielding-scattering correlation needs to be pre-computed for various ranges of the parameters by a large set of simulations, such that a right set(s) of correlations can be referenced for stones of a given patient *in situ*. For construction of the database and optimally referencing the database, applications of data science and machine learning techniques would be of use. Such an advanced system of lithotripsy may also find applications to other types of ultrasound therapies.

BIBLIOGRAPHY

Acosta, A.J. (1958). “An experimental study of cavitating inducers”. In: *Second Symposium on Naval Hydrodynamics: Hydrodynamic Noise Cavity Flow*. Office of Naval Research-Department of the Navy.

Ando, K., T. Colonius, and C.E. Brennen (2011). “Numerical simulation of shock propagation in a polydisperse bubbly liquid”. In: *International Journal of Multiphase Flow* 37.6, pp. 596–608.

Arora, M., C-D. Ohl, and D. Lohse (2007). “Effect of nuclei concentration on cavitation cluster dynamics”. In: *The Journal of the Acoustical Society of America* 121.6, pp. 3432–3436.

Bailey, M.R, J.A McAteer, Y.A Pishchalnikov, M.F Hamilton, and T. Colonius (2006). “Progress in Lithotripsy Research”. In: *Acoustics Today* 3, pp. 18–29.

Balachandar, S and J.K. Eaton (2010). “Turbulent dispersed multiphase flow”. In: *Annual Review of Fluid Mechanics* 42, pp. 111–133.

Bechara, W., C. Bailly, P. Lafon, and S.M. Candel (1994). “Stochastic approach to noise modeling for free turbulent flows”. In: *AIAA Journal* 32.3, pp. 455–463.

Benzi, M. (2002). “Preconditioning techniques for large linear systems: a survey”. In: *Journal of Computational Physics* 182.2, pp. 418–477.

Bergamasco, L. and D. Fuster (2017). “Oscillation regimes of gas/vapor bubbles”. In: *International Journal of Heat and Mass Transfer* 112, pp. 72–80.

Bremond, N., M. Arora, C.-D. Ohl, and D. Lohse (2006). “Controlled multibubble surface cavitation”. In: *Physical Review Letters* 96 (22), p. 224501.

Brennen, C.E. (2013). *Cavitation and bubble dynamics*. Cambridge University Press.

Brenner, M.P., S. Hilgenfeldt, and D. Lohse (2002). “Single-bubble sonoluminescence”. In: *Reviews of modern physics* 74.2, p. 425.

Brunt, C.M., C. Federrath, and D.J. Price (2010). “A method for reconstructing the variance of a 3D physical field from 2D observations: application to turbulence in the interstellar medium”. In: *Monthly Notices of the Royal Astronomical Society* 403.3, pp. 1507–1515.

Caflisch, R.E., M.J. Miksis, G.C. Papanicolaou, and L. Ting (1985). “Effective equations for wave propagation in bubbly liquids”. In: *Journal of Fluid Mechanics* 153, pp. 259–273.

Canney, M.S., M.R. Bailey, L.A. Crum, V.A. Khokhlova, and O.A. Sapozhnikov (2008). “Acoustic characterization of high intensity focused ultrasound fields: A combined measurement and modeling approach”. In: *The Journal of the Acoustical Society of America* 124.4, pp. 2406–2420.

Carstensen, E.L. and L.L. Foldy (1947). “Propagation of sound through a liquid containing bubbles”. In: *The Journal of the Acoustical Society of America* 19.3, pp. 481–501.

Cash, J.R. and A.H. Karp (1990). “A Variable Order Runge-Kutta Method for Initial Value Problems with Rapidly Varying Right-hand Sides”. In: *ACM Transactions on Mathematical Software* 16.3, pp. 201–222.

Chahine, G.L. and H.L. Liu (1985). “A singular-perturbation theory of the growth of a bubble cluster in a superheated liquid”. In: *Journal of Fluid Mechanics* 156, pp. 257–279.

Chang, Q., Y.S. Wong, and H. Fu (1996). “On the algebraic multigrid method”. In: *Journal of Computational Physics* 125.2, pp. 279–292.

Church, C.C (1995). “The effects of an elastic solid surface layer on the radial pulsations of gas bubbles”. In: *The Journal of the Acoustical Society of America* 97.3, pp. 1510–1521.

Cleveland, R.O. and O.A. Sapozhnikov (2005). “Modeling elastic wave propagation in kidney stones with application to shock wave lithotripsy”. In: *The Journal of the Acoustical Society of America* 118.4, pp. 2667–2676.

Coleman, A.J., J.E. Saunders, L.A. Crum, and M. Dyson (1987). “Acoustic cavitation generated by an extracorporeal shockwave lithotripter”. In: *Ultrasound in Medicine & Biology* 13.2, pp. 69–76.

Colonius, T. (2004). “Modeling artificial boundary conditions for compressible flow”. In: *Annual Review of Fluid Mechanics* 36, pp. 315–345.

Commander, K.W. and A. Prosperetti (1989). “Linear pressure waves in bubbly liquids: Comparison between theory and experiments”. In: *The Journal of the Acoustical Society of America* 85.2, pp. 732–746.

Coralic, V. and T. Colonius (2013). “Shock-induced collapse of a bubble inside a deformable vessel”. In: *European Journal of Mechanics-B/Fluids* 40, pp. 64–74.

– (2014). “Finite-volume WENO scheme for viscous compressible multicomponent flows”. In: *Journal of Computational Physics* 274, pp. 95–121.

Cottet, G.H. and P.D. Koumoutsakos (2000). *Vortex methods: theory and practice*. Cambridge university press.

d’Agostino, L. and C.E. Brennen (1989). “Linearized dynamics of spherical bubble clouds”. In: *Journal of Fluid Mechanics* 199, pp. 155–176.

Delong, S., B.E. Griffith, E. Vanden-Eijnden, and A. Donev (2013). “Temporal integrators for fluctuating hydrodynamics”. In: *Physical Review E* 87 (3), p. 033302.

Doinikov, A.A. (2004). “Mathematical model for collective bubble dynamics in strong ultrasound fields”. In: *The Journal of the Acoustical Society of America* 116.2, pp. 821–827.

Foldy, L.L. (1945). “The multiple scattering of waves. I. General theory of isotropic scattering by randomly distributed scatterers”. In: *Physical Review* 67.3-4, p. 107.

Fouque, J.P., J. Garnier, G. Papanicolaou, and K. Solna (2007). *Wave propagation and time reversal in randomly layered media*. Vol. 56. Springer Science & Business Media.

Freund, J.B. (2008). “Suppression of shocked-bubble expansion due to tissue confinement with application to shock-wave lithotripsy”. In: *The Journal of the Acoustical Society of America* 123.5, pp. 2867–2874.

Fuster, D. and T. Colonius (2011). “Modeling bubble clusters in compressible liquids”. In: *Journal of Fluid Mechanics* 55.

Garnier, J. and G. Papanicolaou (2009). “Passive sensor imaging using cross correlations of noisy signals in a scattering medium”. In: *SIAM Journal on Imaging Sciences* 2.2, pp. 396–437.

Gaudron, R., M.T. Warnez, and E. Johnsen (2015). “Bubble dynamics in a viscoelastic medium with nonlinear elasticity”. In: *Journal of Fluid Mechanics* 766, pp. 54–75.

Gilmore, F.R. (1952). “The collapse and growth of a spherical bubble in a viscous compressible liquid”. In: *California Institute of Technology Hydrodynamics Laboratory, Report* 26-4.

Ginter, S., M. Liebler, E. Steiger, T. Dreyer, and R.E. Riedlinger (2002). “Full-wave modeling of therapeutic ultrasound: Nonlinear ultrasound propagation in ideal fluids”. In: *The Journal of the Acoustical Society of America* 111.5, pp. 2049–2059.

Hill, D.J. and D.I. Pullin (2004). “Hybrid tuned center-difference-WENO method for large eddy simulations in the presence of strong shocks”. In: *Journal of Computational Physics* 194.2, pp. 435–450.

Honein, A.E. and P. Moin (2004). “Higher entropy conservation and numerical stability of compressible turbulence simulations”. In: *Journal of Computational Physics* 201.2, pp. 531–545.

Ikeda, T., S. Yoshizawa, N. Koizumi, M. Mitsuishi, and Y. Matsumoto (2016). “Focused ultrasound and lithotripsy”. In: *Therapeutic Ultrasound*. Springer, pp. 113–129.

Ikeda, T., S. Yoshizawa, T. Masataka, J.S. Allen, S. Takagi, N. Ohta, T. Kitamura, and Y. Matsumoto (2006). “Cloud cavitation control for lithotripsy using high intensity focused ultrasound”. In: *Ultrasound in Medicine & Biology* 32.9, pp. 1383–1397.

Ilinskii, Y.A, M.F. Hamilton, and E.A. Zabolotskaya (2007). “Bubble interaction dynamics in Lagrangian and Hamiltonian mechanics”. In: *The Journal of the Acoustical Society of America* 121.2, pp. 786–795.

Ishimaru, A. (1978). *Wave propagation and scattering in random media*. Vol. 2. Academic press New York.

Jingsen, M., T.H. Chao, and Georges L.C. (2018). “Numerical study of acoustically driven bubble cloud dynamics near a rigid wall”. In: *Ultrasonics Sonochemistry* 40.Part A, pp. 944–954.

Johnsen, E. and T. Colonius (2006). “Implementation of WENO schemes in compressible multicomponent flow problems”. In: *Journal of Computational Physics* 219.2, pp. 715–732.

– (2009). “Numerical simulations of non-spherical bubble collapse”. In: *Journal of Fluid Mechanics* 629, pp. 231–262.

Johnsen, E., J. Larsson, A.V Bhagatwala, W.H. Cabot, P. Moin, B.J. Olson, P.S. Rawat, S.K. Shankar, B. Sjögreen, H.C. Yee, and others. (2010). “Assessment of high-resolution methods for numerical simulations of compressible turbulence with shock waves”. In: *Journal of Computational Physics* 229.4, pp. 1213–1237.

Kameda, M. and Y. Matsumoto (1996). “Shock waves in a liquid containing small gas bubbles”. In: *Physics of Fluids* 8.2, pp. 322–335.

Kato, H. (1975). “A consideration on scaling laws of cavitation erosion”. In: *International Shipbuilding Progress* 22.253.

Keller, J.B. and M. Miksis (1980). “Bubble oscillations of large amplitude”. In: *The Journal of the Acoustical Society of America* 68.2, pp. 628–633.

Kitagawa, A., Y. Murai, and F. Yamamoto (2001). “Two-way coupling of Eulerian–Lagrangian model for dispersed multiphase flows using filtering functions”. In: *International Journal of Multiphase Flow* 27.12, pp. 2129–2153.

Knapp, R.T. (1954). “Present Status of Cavitation Research”. In: *Mechanical Engineering* 76.9, pp. 731–734.

Krimmel, J., T. Colonius, and M. Tanguay (2010). “Simulation of the effects of cavitation and anatomy in the shock path of model lithotripters”. In: *Urological Research* 38.6, pp. 505–518.

Kuo, S.M. and D. Morgan (1995). *Active noise control systems: algorithms and DSP implementations*. John Wiley & Sons, Inc. ISBN: 0471134244.

Lauterborn, W. and E. Cramer (1981). “Subharmonic route to chaos observed in acoustics”. In: *Physical Review Letters* 47.20, p. 1445.

Lee, D., A.D. Pierce, and E.C. Shang (2000). “Parabolic equation development in the twentieth century”. In: *Journal of Computational Acoustics* 8.04, pp. 527–637.

Lele, S.K. and J. Larsson (2009). “Shock-turbulence interaction: What we know and what we can learn from peta-scale simulations”. In: *Journal of Physics: Conference Series*. Vol. 180. 1. IOP Publishing, p. 012032.

Leonard, A. (1975). “Energy cascade in large-eddy simulations of turbulent fluid flows”. In: *Advances in geophysics*. Vol. 18. Elsevier, pp. 237–248.

Liu, X-D, S. Osher, and T. Chan (1994). “Weighted essentially non-oscillatory schemes”. In: *Journal of computational physics* 115.1, pp. 200–212.

Lokhandwalla, M. and B. Sturtevant (2000). “Fracture mechanics model of stone comminution in ESWL and implications for tissue damage”. In: *Physics in Medicine & Biology* 45.7, p. 1923.

Maeda, K., M. Date, K. Sugiyama, S. Takagi, and Y. Matsumoto (2013). “On the motion of a pair of bubbles rising near-wall in a vertical channel bubbly flow”. In: *Proc. 8th International Conf. of Multiphase Flow, Paper*. 535.

Maeda, K., W. Kreider, A. Maxwell, B. Cunitz, T. Colonius, and M. Bailey (2015). “Modeling and experimental analysis of acoustic cavitation bubbles for Burst Wave Lithotripsy”. In: *Journal of Physics: Conference Series* 656.1, p. 012027.

Magnaudet, J. and D. Legendre (1998). “The viscous drag force on a spherical bubble with a time-dependent radius”. In: *Physics of Fluids* 10.3, pp. 550–554.

Matsumoto, Y. and S. Yoshizawa (2005). “Behaviour of a bubble cluster in an ultrasound field”. In: *International Journal for Numerical Methods in Fluids* 47.6-7, pp. 591–601.

Maxell, A.D. (2016). In: *Private communication*.

Maxwell, A.D., B.W. Cunitz, W. Kreider, O.A. Sapozhnikov, R.S. Hsi, J.D. Harper, M.R. Bailey, and M.D. Sorensen (2015). “Fragmentation of urinary calculi in vitro by burst wave lithotripsy”. In: *The Journal of urology* 193.1, pp. 338–344.

McAteer, J.A., M.R. Bailey, J.C. Williams Jr, R.O. Cleveland, and A.P. Evan (2005). “Strategies for improved shock wave lithotripsy”. In: *Minerva urologica e nefrologica = The Italian journal of urology and nephrology* 57.4, pp. 271–287.

Meneveau, C. and J. Katz (2000). “Scale-invariance and turbulence models for large-eddy simulation”. In: *Annual Review of Fluid Mechanics* 32.1, pp. 1–32.

Meng, J.C. and T. Colonius (2018). “Numerical simulation of the aerobreakup of a water droplet”. In: *Journal of Fluid Mechanics* 835, pp. 1108–1135.

Monaghan, J.J (2005). “Smoothed particle hydrodynamics”. In: *Reports on Progress in Physics* 68.8, p. 1703.

Mørch, K.A. (1980). “On the collapse of cavity clusters in flow cavitation”. In: *Cavitation and Inhomogeneities in Underwater Acoustics*. Springer, pp. 95–100.

– (1982). “Energy considerations on the collapse of cavity clusters”. In: *Mechanics and Physics of Bubbles in Liquids*. Springer, pp. 313–321.

Nelson, P.A. and S.J. Elliott (1991). *Active control of sound*. Academic press.

Okita, K., K. Ono, S. Takagi, and Y. Matsumoto (2011). "Development of high intensity focused ultrasound simulator for large-scale computing". In: *International Journal for Numerical Methods in Fluids* 65.1-3, pp. 43–66.

Omang, M., S. Børve, and J. Trulsen (2006). "SPH in spherical and cylindrical coordinates". In: *Journal of Computational Physics* 213.1, pp. 391–412.

Omta, R. (1987). "Oscillations of a cloud of bubbles of small and not so small amplitude". In: *The Journal of the Acoustical Society of America* 82.3, pp. 1018–1033.

O'Neil, H.T. (1949). "Theory of Focusing Radiators". In: *The Journal of the Acoustical Society of America* 21.5, pp. 516–526.

Perigaud, G. and R. Saurel (2005). "A compressible flow model with capillary effects". In: *Journal of Computational Physics* 209.1, pp. 139–178.

Peskin, C.S. (2002). "The immersed boundary method". In: *Acta Numerica* 11, pp. 479–517.

Pirozzoli, S. (2002). "Conservative hybrid compact-WENO schemes for shock-turbulence interaction". In: *Journal of Computational Physics* 178.1, pp. 81–117.

– (2006). "On the spectral properties of shock-capturing schemes". In: *Journal of Computational Physics* 219.2, pp. 489–497.

Pishchalnikov, Y.A., O.A. Sapozhnikov, M.R. Bailey, J.C. Williams Jr, R.O. Cleveland, T. Colonius, L.A. Crum, A.P. Evan, and J.A. McAteer (2003). "Cavitation bubble cluster activity in the breakage of kidney stones by lithotripter shockwaves". In: *Journal of Endourology* 17.7, pp. 435–446.

Plesset, M.S. (1949). "The dynamics of cavitation bubbles". In: *Journal of Applied Mechanics* 16, pp. 277–282.

Plesset, M.S. and A.T. Ellis (1955). "On the mechanism of cavitation damage". In: *Transactions of the ASME* 77, pp. 1055–1064.

Plesset, M.S. and A. Prosperetti (1977). "Bubble Dynamics and Cavitation". In: *Annual Review of Fluid Mechanics* 9.1, pp. 145–185.

Preston, A.T., T. Colonius, and C.E. Brennen (2007). "A reduced-order model of diffusive effects on the dynamics of bubbles". In: *Physics of Fluids* 19, p. 123302.

Prosperetti, A., L.A. Crum, and K.W. Commander (1988). "Nonlinear bubble dynamics". In: *The Journal of the Acoustical Society of America* 83.2, pp. 502–514.

Rasthofer, U., F. Wermelinger, P. Hadijdoukas, and P. Koumoutsakos (2017). "Large Scale Simulation of Cloud Cavitation Collapse". In: *Procedia Computer Science* 108.Supplement C, pp. 1763–1772.

Rayleigh, L. (1917). "VIII. On the pressure developed in a liquid during the collapse of a spherical cavity". In: *The London, Edinburgh, and Dublin Philosophical Magazine and Journal of Science* 34.200, pp. 94–98.

Reisman, G.E., Y-C Wang, and C.E. Brennen (1998). “Observations of shock waves in cloud cavitation”. In: *Journal of Fluid Mechanics* 355, pp. 255–283.

Rossinelli, D., B. Hejazialhosseini, P. Hadjidoukas, C. Bekas, A. Curioni, A. Bertsch, S. Futral, S.J. Schmidt, N.A. Adams, and P. Koumoutsakos (2013). “11 PFLOP/s simulations of cloud cavitation collapse”. In: *SC ’13 Proceedings of the International Conference on High Performance Computing, Networking, Storage and Analysis*. IEEE, pp. 1–13.

Sapozhnikov, O.A. (2012). “An exact solution to the Helmholtz equation for a quasigaussian beam in the form of a superposition of two sources and sinks with complex coordinates”. In: *Acoustical Physics* 58.1, pp. 41–47.

Shimada, M., Y. Matsumoto, and T. Kobayashi (2000). “Influence of the nuclei size distribution on the collapsing behavior of the cloud cavitation”. In: *JSME International Journal Series B Fluids and Thermal Engineering* 43.3, pp. 380–385.

Shu, C.W. (2016). “High order WENO and DG methods for time-dependent convection-dominated PDEs: A brief survey of several recent developments”. In: *Journal of Computational Physics* 316, pp. 598–613.

Smirnov, A., S. Shi, and I. Celik (2001). “Random flow generation technique for large eddy simulations and particle-dynamics modeling”. In: *Transactions of the ASME-I-Journal of Fluids Engineering* 123.2, pp. 359–371.

Takahira, H., A. Akamatsu, and S. Fujikawa (1994). “Dynamics of a Cluster of Bubbles in a Liquid : Theoretical Analysis”. In: *JSME International Journal Series B* 37.2, pp. 297–305.

Tanguay, M. (2004). “Numerical Simulation and Analysis of Shockwave Lithotripsy”. PhD thesis. California Institute of Technology.

Tanguay, M. and T. Colonius (2003). “Progress in modeling and simulation of shock wave lithotripsy (SWL)”. In: *Fifth International Symposium on cavitation (CAV2003)*.

Thoma, Clemens (2014). “Stones: Bursting through limitations of SWL”. In: *Nature Reviews Urology* 11.10, p. 540.

Thompson, K.W. (1987). “Time dependent boundary conditions for hyperbolic systems”. In: *Journal of Computational Physics* 68.1, pp. 1–24.

Titarev, V.A. and E.F. Toro (2004). “Finite-volume WENO schemes for three-dimensional conservation laws”. In: *Journal of Computational Physics* 201.1, pp. 238–260.

Tiwari, A., C. Pantano, and J.B. Freund (2015). “Growth-and-collapse dynamics of small bubble clusters near a wall”. In: *Journal of Fluid Mechanics* 775, pp. 1–23.

Tomita, Y and A Shima (1986). “Mechanisms of impulsive pressure generation and damage pit formation by bubble collapse”. In: *Journal of Fluid Mechanics* 169, pp. 535–564.

Tornberg, A.K. and B. Engquist (2003). “Regularization Techniques for Numerical Approximation of PDEs with Singularities”. In: *Journal of Scientific Computing* 19.1, pp. 527–552.

Toro, Eleuterio F (2013). *Riemann solvers and numerical methods for fluid dynamics: a practical introduction*. Springer Science & Business Media.

Towne, A. and T. Colonius (2015). “One-way spatial integration of hyperbolic equations”. In: *Journal of Computational Physics* 300, pp. 844–861.

vanWijngaarden, L. (1966). “On the collective collapse of a large number of gas bubbles in water”. In: *Applied Mechanics*. Springer, pp. 854–861.

vanWijngaarden, L (1968). “On the equations of motion for mixtures of liquid and gas bubbles”. In: *Journal of Fluid Mechanics* 33.3, pp. 465–474.

Wang, Y-C. and C.E. Brennen (1994). “Shock wave development in the collapse of a cloud of bubbles”. In: *ASME*. 194. American Society of Mechanical Engineers, pp. 15–19.

– (1999). “Numerical computation of shock waves in a spherical cloud of cavitation bubbles”. In: *Journal of Fluids Engineering* 121.4, pp. 872–880.

Whitham, G.B. (2011). *Linear and nonlinear waves*. Vol. 42. John Wiley & Sons. ISBN: 1118031202.

Williams, J.E. Ffowcs (1984). “Review lecture: Anti-sound”. In: *Proceedings of the Royal Society of London A: Mathematical, Physical and Engineering Sciences* 395.1808, pp. 63–88.

Yoshizawa, Shin, Teiichiro Ikeda, Akira Ito, Ryuhei Ota, Shu Takagi, and Yoichiro Matsumoto (2009). “High intensity focused ultrasound lithotripsy with cavitating microbubbles”. In: *Medical & biological engineering & computing* 47.8, pp. 851–860.

Yurkovetsky, Y. and J.F. Brady (1996). “Statistical mechanics of bubbly liquids”. In: *Physics of Fluids* 8.4, pp. 881–895.

Zeravcic, Z., D. Lohse, and W. Van Saarloos (2011). “Collective oscillations in bubble clouds”. In: *Journal of Fluid Mechanics* 680, pp. 114–149. DOI: `10.1017/jfm.2011.153`.

Zhang, D.Z. and A. Prosperetti (1994). “Ensemble phase-averaged equations for bubbly flows”. In: *Physics of Fluids* 6.9, pp. 2956–2970.

Appendix A

NOTE ON THE DYNAMICS OF SPHERICAL BUBBLES UNDER MUTUAL INTERACTIONS

A.1 Overview

In this appendix, the dynamical equation for the oscillations of spherical gas bubbles under mutual interactions in a viscous potential flow is reviewed and analyzed. The Euler-Lagrange equation is used to derived a non-autonomous, implicit system of ODEs in terms of the radius and the radial velocity of each bubble, that corresponds to the Rayleigh-Plesset equation in the limit of single bubble. The complexity of the direct solution method is $O(N_b^3)$, where N_b is the total number of bubbles, that comes from matrix inversion. A preconditioning strategy is introduced to avoid the matrix inversion and reduce the complexity to $O(N_b^2)$. The relation of the preconditioning and the canonical transformation of the dynamical equation proposed by Ilinskii et al. (2007) is discussed. For a spherical bubble cloud, the preconditioning is successful if $B_0 < 1$, but otherwise non-trivial, thus may not be applied to a dense and or large bubble cloud with $B_0 > 1$.

A.2 Rayleigh-Plesset equation extended for multiple bubbles

We briefly review the derivation of the Rayleigh-Plesset equation formulated for a system of multiple bubbles. For rigorous approaches, see for instance Takahira et al. (1994), Doinikov (2004), and Ilinskii et al. (2007). We consider N_b spherical bubbles with a radius of $R_{i0}, i \in \mathbb{Z} : i \in [1, N_b]$, positioned at coordinate $\boldsymbol{x}_{i0}$, in an unbounded, incompressible, viscous liquid initially quiescent. Bubbles are subjected to weak, far-field pressure excitation with a fixed amplitude and a frequency. We solve for the temporal evolutions of radius $R_i(t)$. For simplicity, here we assume that the bubbles do not translate, thus $\dot{\boldsymbol{x}}_{i0} = \boldsymbol{0}$. We also neglect heat and mass transfer across the bubble interface as well as liquid compressibility, though the model can be extended to include those effects. We denote the ratio of the characteristic radius of bubbles, R to the normalized, characteristic inter-bubble distance D as $S = R/D$. We derive the dynamical equation for $R_i(t)$ using the Euler-Lagrange equation. We express the velocity potential at the surface of bubble i using a multi-pole expansion through $O(S^3)$. By doing so, the kinetic energy of liquid induced by bubble oscillations up to $O(S^3)$ can be expressed as

$$\mathcal{K} = 2\pi\rho\left[\sum_{i}^{N_b} R_i^3\dot{R}_i^2 + \sum_{i}^{N_b}\sum_{k\neq i}^{N_b}\frac{R_i^2R_k^2}{r_{ik}}\dot{R}_i\dot{R}_k + R^3\dot{R}^2O(S^4)\right] \tag{A.1}$$

The far-field pressure excitation can be considered as an additional kinetic energy of the system:

$$\mathcal{K}_e = -\sum_{i}^{N_b}\frac{4\pi}{3}R_i^3p_e, \tag{A.2}$$

where p_e is the amplitude of the excitation.

The potential energy of the system is given as

$$\mathcal{V} \;=\; \sum_{i}^{N_b}\int_{V_0}^{V_i}(p_{0i} - p_i)dV_i. \tag{A.3}$$

Therefore we obtain the Lagrangian of the system as a function of R_i, $\dot{R}_i$ as

$$\mathcal{L} = \mathcal{K} + \mathcal{K}_e - \mathcal{V}. \tag{A.4}$$

Substituting expressions (A.1-A.3) into the Euler-Lagrange equation,

$$\frac{d}{dt}\left(\frac{\partial\mathcal{L}}{\partial\dot{R}_i}\right) - \frac{\partial\mathcal{L}}{\partial R} = 0, \tag{A.5}$$

we obtain

$$R_i\ddot{R}_i + \frac{3}{2}\dot{R}_i^2 = \frac{P_i - P_e}{\rho} - \sum_{k\neq i}^{N_b}\frac{R_k}{r_{ik}}(R_k\ddot{R}_k + 2\dot{R}_k^2), \tag{A.6}$$

where

$$P_e = P_0 + p_e \tag{A.7}$$

and

$$P_i = \left(p_{i0} + \frac{2\sigma}{R_{i0}}\right)\left(\frac{R_{i0}}{R_i}\right) - \frac{2\sigma}{R_i}. \tag{A.8}$$

Clearly we recover the Rayleigh-Plesset equation for single bubble with $N = 1$. In this study we denote this equation as the extended Rayleigh-Plesset equation (hereafter denoted as the eRP equation). The eRP equation is a system of second order nonlinear ordinary differential equation in terms of R_i and can be expressed as a non-autonomous, implicit ODE about $\boldsymbol{q} = [\dot{R}_1, \dot{R}_2, ..., \dot{R}_{N_b}]^{\mathrm{T}}$ as

$$\boldsymbol{A}\dot{\boldsymbol{q}} = \boldsymbol{B}\boldsymbol{r} + \boldsymbol{p}, \tag{A.9}$$

where

$$\boldsymbol{A} = \begin{bmatrix} R_1 & \frac{R_2^2}{r_{12}} & \frac{R_3^2}{r_{13}} & \dots & \frac{R_n^2}{r_{1n}} \\ \frac{R_1^2}{r_{21}} & R_2 & \frac{R_3^2}{r_{23}} & \dots & \frac{R_n^2}{r_{2n}} \\ \frac{R_1^2}{r_{31}} & \frac{R_2^2}{r_{32}} & R_3 & \dots & \frac{R_n^2}{r_{3n}} \\ \vdots & \vdots & \vdots & \ddots & \vdots \\ \frac{R_1^2}{r_{n1}} & \frac{R_2^2}{r_{n2}} & \frac{R_3^2}{r_{n3}} & \dots & R_n \end{bmatrix}, \boldsymbol{B} = - \begin{bmatrix} \frac{3}{2} & \frac{2R_1}{r_{12}} & \frac{2R_1}{r_{13}} & \dots & \frac{2R_1}{r_{1n}} \\ \frac{2R_2}{r_{21}} & \frac{3}{2} & \frac{2R_2}{r_{23}} & \dots & \frac{2R_2}{r_{2n}} \\ \frac{2R_3}{r_{31}} & \frac{2R_3}{r_{32}} & \frac{3}{2} & \dots & \frac{2R_3}{r_{3n}} \\ \vdots & \vdots & \vdots & \ddots & \vdots \\ \frac{2R_n}{r_{n1}} & \frac{2R_n}{r_{n2}} & \frac{2R_n}{r_{n3}} & \dots & \frac{3}{2} \end{bmatrix}, \tag{A.10}$$

$$\boldsymbol{r} = \begin{bmatrix} \dot{R}_1^2 \\ \dot{R}_2^2 \\ \dot{R}_3^2 \\ \vdots \\ \dot{R}_N^2 \end{bmatrix}, \boldsymbol{p} = \begin{bmatrix} \frac{P_1 - P_e}{\rho} \\ \frac{P_2 - P_e}{\rho} \\ \frac{P_3 - P_e}{\rho} \\ \vdots \\ \frac{P_n - P_e}{\rho} \end{bmatrix}. \tag{A.11}$$

$\boldsymbol{A}$ is a full-rank matrix, thus we can directly compute $\boldsymbol{A}^{-1}$ to obtain the explicit form:

$$\dot{\boldsymbol{q}} = \boldsymbol{A}^{-1}[\boldsymbol{B}\boldsymbol{r} + \boldsymbol{p}]. \tag{A.12}$$

The matrix inversion is required at every step of numerical integration. As a result the overall complexity of the solution method scales like $O(N_b^3)$, and the problem is challenging with a large N_b. This motivates us to seek for solution methods with a lower complexity to solve for the ODE without computing $\boldsymbol{A}^{-1}$.

Matrix preconditioning

To this end, we aim to solve for the ODE using matrix preconditioning. We first split $\boldsymbol{A}$ into its diagonal component $\boldsymbol{A}_d$ and the remainder$\boldsymbol{A}_{ad}$:

$$\boldsymbol{A} = \boldsymbol{A}_d + \boldsymbol{A}_{ad}. \tag{A.13}$$

Then the eRP equation equation the becomes

$$\boldsymbol{A}_d \dot{\boldsymbol{q}} = \boldsymbol{B}\boldsymbol{r} + \boldsymbol{p} - \boldsymbol{A}_{ad} \dot{\boldsymbol{q}} \tag{A.14}$$

Thus

$$\begin{aligned} \dot{\boldsymbol{q}} &= \boldsymbol{A}_d^{-1}[\boldsymbol{B}\boldsymbol{r} + \boldsymbol{p} - \boldsymbol{A}_{ad} \dot{\boldsymbol{q}}] && \text{(A.15)} \\ &= \boldsymbol{s} - \boldsymbol{T}\dot{\boldsymbol{q}}, && \text{(A.16)} \end{aligned}$$

where we denote $\boldsymbol{s} = \boldsymbol{A}_d^{-1}[\boldsymbol{B}\boldsymbol{r} + \boldsymbol{p}]$ and $\boldsymbol{T} = \boldsymbol{A}_d^{-1}\boldsymbol{A}_{ad}$. We can perform successive substitution to this equation:

$$\begin{aligned}
\dot{\boldsymbol{q}} &= \boldsymbol{s} - \boldsymbol{T}\dot{\boldsymbol{q}} && \text{(A.17)}\\
&= \boldsymbol{s} - \boldsymbol{T}[\boldsymbol{s} - \boldsymbol{T}\dot{\boldsymbol{q}}] && \text{(A.18)}\\
&= \boldsymbol{s} - \boldsymbol{T}\boldsymbol{s} + \boldsymbol{T}^2\dot{\boldsymbol{q}} && \text{(A.19)}\\
&= \boldsymbol{s} - \boldsymbol{T}\boldsymbol{s} + \boldsymbol{T}^2[\boldsymbol{s} - \boldsymbol{T}\dot{\boldsymbol{q}}] && \text{(A.20)}\\
&= \boldsymbol{s} - \boldsymbol{T}\boldsymbol{s} + \boldsymbol{T}^2\boldsymbol{s} - \boldsymbol{T}^3\dot{\boldsymbol{q}} && \text{(A.21)}\\
&= \cdots && \text{(A.22)}\\
&= \left[\sum_{n=0}^{N_b}(-\boldsymbol{T})^n\right]\boldsymbol{s} + (-\boldsymbol{T})^{N+1}\dot{\boldsymbol{q}}. && \text{(A.23)}
\end{aligned}$$

For this iterative substitution to be convergent, we clearly need $\boldsymbol{T}$ to be a convergent matrix. Notice that this operation is nothing but the Jacobi method for a linear system. The condition for the method to converge is that $\boldsymbol{A}$ is diagonally dominant (sufficient but not necessary). At this point the meaning of the iterative method, nor diagonally dominance of $\boldsymbol{A}$, from the perspective of bubble dynamics, is not clear. In the following sections we seek for a physical interpretation of the condition of $\boldsymbol{A}$.

A.3 Canonical formulation

The Hamiltonian

To gain a physical insight into the dynamical equation, we transform the equation into a Hamiltonian system. Hamiltonian represents the total energy of dynamical system as a function of coordinate and conjugate momenta. In what follows we analyze the contribution of inter-bubble interactions on system's Hamiltonian, in order to understand how the interactions affect the resulting bubble cloud dynamics. The Hamiltonian can be described as

$$\mathcal{H} = \mathcal{K} + \mathcal{K}_e + \mathcal{V}. \tag{A.24}$$

The kinetic energy of the system is expressed as

$$\mathcal{K} = \frac{1}{2}\sum_{i}^{N_b} G_i \dot{R}_i, \tag{A.25}$$

where G_i is the conjugate momenta, corresponding to R_i.

We can employ the same expressions of $\mathcal{K}_e$ and $\mathcal{V}$ used for the Lagrangian, since they are functions of R_i. Since Hamiltonian is a function of R_i and G_i, but not $\dot{R}_i$, we need to obtain $\dot{R}_i$ as a function of R_i and G_i, to be used to express $\mathcal{K}$. To do so, we derive G_i as a function of R_i and $\dot{R}_i$ using the following formula:

$$\begin{aligned} G_i &= \frac{\partial \mathcal{H}}{\partial \dot{R}_i} && \text{(A.26)} \\ &= 4\pi\rho \left[R_i^3 \dot{R}_i + \sum_{k\neq i}^{N_b} \frac{R_i^2 R_k^2}{r_{ik}} \dot{R}_k \right], && \text{(A.27)} \end{aligned}$$

This is a linear system in terms of $\dot{R}_i$, and can be written in a compact form as

$$\boldsymbol{g} = 4\pi\rho \boldsymbol{D}\boldsymbol{q}, \tag{A.28}$$

where $\boldsymbol{g} = [G_1, G_2, ...G_N]^{\mathrm{T}}$, and $\boldsymbol{D} = \boldsymbol{A}_d^2 \boldsymbol{A}$.
The kinetic energy is thus expressed as

$$\mathcal{K} = \frac{1}{2}\boldsymbol{q}^{\mathrm{T}}\boldsymbol{g} = \frac{1}{2}\boldsymbol{q}^{\mathrm{T}}\boldsymbol{D}\boldsymbol{q} = \frac{1}{2}\boldsymbol{g}^{\mathrm{T}}\boldsymbol{D}^{-1}\boldsymbol{g} = \frac{1}{2}\boldsymbol{g}^{\mathrm{T}}\boldsymbol{q}. \tag{A.29}$$

To solve for $\boldsymbol{q} = \boldsymbol{D}^{-1}\boldsymbol{g}/4\pi\rho = \boldsymbol{A}^{-1}\boldsymbol{A}_d^{-2}\boldsymbol{g}/4\pi\rho$, it requires computations of $\boldsymbol{A}^{-1}$. Following the previous section, we substitute $\boldsymbol{A} = \boldsymbol{A}_d + \boldsymbol{A}_{ad}$ into this equation to obtain

$$\begin{aligned} 4\pi\rho\boldsymbol{q} &= \boldsymbol{A}_d^{-1}(\boldsymbol{A}_d^{-2}\boldsymbol{g} - \boldsymbol{A}_{ad}\boldsymbol{q}) && \text{(A.30)} \\ &= \boldsymbol{A}_d^{-3}\boldsymbol{g} + \left[\sum_{n=1}^{N_b}(-\boldsymbol{T})^n\right]\boldsymbol{A}_d^{-3}\boldsymbol{g} + (-\boldsymbol{T})^{N+1}\dot{\boldsymbol{q}}. && \text{(A.31)} \end{aligned}$$

When $\boldsymbol{A}$ is diagonally dominant, the expression is convergent and we obtain

$$4\pi\rho\boldsymbol{q} = \boldsymbol{A}_d^{-3}\boldsymbol{g} + \left[\sum_{n=1}^{\infty}(-\boldsymbol{T})^n\right]\boldsymbol{A}_d^{-3}\boldsymbol{g}, \tag{A.32}$$

and the kinetic energy becomes

$$\begin{aligned} 4\pi\rho\mathcal{K} &= \frac{1}{2}\boldsymbol{g}^{\mathrm{T}}\boldsymbol{A}_d^{-3}\boldsymbol{g} + \frac{1}{2}\boldsymbol{g}^{\mathrm{T}}\left[\sum_{n=1}^{N_b}(-\boldsymbol{T})^n\right]\boldsymbol{A}_d^{-3}\boldsymbol{g} + \frac{1}{2}\boldsymbol{g}^{\mathrm{T}}(-\boldsymbol{T})^{N_b+1}\dot{\boldsymbol{q}} && \text{(A.33)} \\ &= \frac{1}{2}\boldsymbol{g}^{\mathrm{T}}\boldsymbol{A}_d^{-3}\boldsymbol{g} + \frac{1}{2}\boldsymbol{g}^{\mathrm{T}}\left[\sum_{n=1}^{\infty}(-\boldsymbol{T})^n\right]\boldsymbol{A}_d^{-3}\boldsymbol{g}. && \text{(A.34)} \end{aligned}$$

Then the Hamiltonian is expressed as a function of R_i and G_i:

$$\mathcal{H} = \frac{1}{8\pi\rho}\boldsymbol{g}^{\mathrm{T}}\left[\sum_{n=0}^{\infty}(-\boldsymbol{T})^n\right]\boldsymbol{A}_d^{-3}\boldsymbol{g} + \mathcal{K}_e + \mathcal{V}. \tag{A.35}$$

Dynamical equation (Hamilton's equation) can be readily derived as

$$\boldsymbol{q} = \frac{\partial \mathcal{H}}{\partial \boldsymbol{g}}, \quad \dot{\boldsymbol{g}} = -\frac{\partial \mathcal{H}}{\partial \boldsymbol{u}}, \tag{A.36}$$

where $\boldsymbol{u} = [R_1, R_2, ...R_{N_b}]^{\mathrm{T}}$.

Explicitly,

$$4\pi\rho \boldsymbol{q} = \boldsymbol{A}_d^{-1}\boldsymbol{g} + \left[\sum_{n=1}^{N}(-\boldsymbol{T})^n\right]\boldsymbol{A}_d^{-1}\boldsymbol{g} + (-\boldsymbol{T})^{N+1}\dot{\boldsymbol{q}}. \tag{A.37}$$

$$\dot{\boldsymbol{g}} = \frac{\partial}{\partial \boldsymbol{g}}\frac{1}{2}\boldsymbol{g}^{\mathrm{T}}\left[\sum_{n=1}^{N_b}(-\boldsymbol{T})^n\right]\boldsymbol{A}_d^{-1}\boldsymbol{g} + \frac{1}{2}\boldsymbol{g}^{\mathrm{T}}(-\boldsymbol{T})^{N+1}\dot{\boldsymbol{q}}. \tag{A.38}$$

This is a system of first order differential equations and can be numerically integrated without matrix inversion. Note that the reduction of complexity by solving this form of Hamilton's equation was proposed by Ilinskii et al. (2007). However, as opposed to the claim of Ilinskii et al. (2007), the following should be emphasized: the complexities to solve for the eRP equation equation and the Hamilton's equation are essentially the same, since direct methods for both equations require matrix inversion of $\boldsymbol{A}$; the preconditioning of $\boldsymbol{A}$ is not guaranteed to be valid when $\boldsymbol{A}$ is non-diagonally dominant.

Condition of *A*

We showed that for both the eRP equation and Hamilton's equations, the Jacobi method can be used for preconditioning $\boldsymbol{A}$. A sufficient condition for the Jacobi method to be valid is that A is diagonally dominant, that says

$$\sum_{i}^{N_b} R_i \geq \sum_{i}^{N_b}\sum_{k\neq i}^{N_b}\frac{R_i^2}{r_{ik}}. \tag{A.39}$$

To understand the physical meaning of the condition, we consider the summation $S_i = \sum_i^{N_b} R_i/r_{ik}$ for bubble i located at the center of a spherical bubble cloud. We assume that bubbles are homogeneously distributed in the cloud. Then the number of bubbles occupying a thin spherical shell, at a radial coordinate of r, scales like r^2, while the contribution of each bubble to S_i scales like $1/r$. Thus the total contribution of the bubbles in the shell scales like $r^2/r = r$. This scaling clearly results from the long-range $(1/r)$ nature of inter-bubble interactions. This suggests that the bubbles at the periphery (out-most shell) of the cloud contribute to S_i the most, and thus the characteristic length scale of the inter-bubble distance r_{ik} is the cloud radius R_c.

In the limit of weak (linear) oscillation, the characteristic bubble size is $R_i \sim R_0$. Therefore, using $r_{ik} \sim R_c$, the condition for diagonally dominance becomes

$$\frac{N_b R_0}{R_c} < 1. \tag{A.40}$$

Following chapter 4, this is nothing but

$$B_0 < 1. \tag{A.41}$$

In practical applications, clouds can become dense and/or large, and can have $B_0 > 1$. The condition for diagonal dominance is not satisfied for such clouds and the iterative method can fail. Other preconditioning methods than Jocobi method could be used to solve for the linear system, such as Krylov subspace method and conjugate gradient method (Benzi, 2002), while preconditioning of non-diagonally dominant matrix may be in general not trivial.

Scaling of $\mathcal{K}$

Now we consider the physical meaning of the condition for diagonal dominance of $\boldsymbol{A}$, through the expression of $\mathcal{K}$:

$$4\pi\rho\mathcal{K} = \frac{1}{2}\boldsymbol{g}^{\mathrm{T}}\boldsymbol{A}_d^{-3}\boldsymbol{g} + \frac{1}{2}\boldsymbol{g}^{\mathrm{T}}\left[\sum_{n=1}^{N_b}(-\boldsymbol{T})^n\right]\boldsymbol{A}_d^{-3}\boldsymbol{g} + \frac{1}{2}\boldsymbol{g}^{\mathrm{T}}(-\boldsymbol{T})^{N+1}\dot{\boldsymbol{q}}. \tag{A.42}$$

When $\boldsymbol{A}_{ad} = \boldsymbol{0}$,

$$\mathcal{K} = \frac{1}{8\pi\rho}\boldsymbol{g}^{\mathrm{T}}\boldsymbol{A}_d^{-3}\boldsymbol{g}. \tag{A.43}$$

This is the kinetic energy due to self-action of bubbles. It is clear that the operator $\boldsymbol{A}_d^{-3}$ and $\sum_{n=1}^{N_b}(-\boldsymbol{T})^n\boldsymbol{A}_d^{-3}$ correspond to the kinetic energy due to self-action and that of inter-bubble interactions, respectively.[1]

Following the previous section, we scale the two terms using R_c, as a characteristic length scale:

$$\boldsymbol{g}^{\mathrm{T}}\boldsymbol{A}_d^{-3}\boldsymbol{g} \sim \frac{N_b}{R_0^3}\boldsymbol{g}^{\mathrm{T}}\boldsymbol{g} \tag{A.44}$$

---

[1] $\boldsymbol{A}$ can be interpreted as a matrix operator that represents the effective (virtual) mass of the fluid that contributes to the energy induced by the interacting bubbles. The virtual mass matrix for a system of bubbles under translational motions (without volumetric oscillations) is discussed by Yurkovetsky and Brady (1996).

$$\boldsymbol{g}^{\mathrm{T}}\left[\sum_{n=1}^{N_b}(-\boldsymbol{T})^n\right]\boldsymbol{A}_d^{-3}\boldsymbol{g} \sim \frac{N_b}{R_0^3}\left[\sum_{n=1}^{N_b}\left(-\frac{N_bR_0}{R_c}\right)^n\right]\boldsymbol{g}^{\mathrm{T}}\boldsymbol{g} = \frac{N_b}{R_0^3}\left[\sum_{n=1}^{N_b}(-B)^n\right]\boldsymbol{g}^{\mathrm{T}}\boldsymbol{g}. \quad (A.45)$$

This scaling is also clear with index notation:

$$\begin{aligned}\mathcal{K} =& \frac{1}{2}\sum_{i}^{N_b}\left[\frac{G_i^2}{4\pi\rho R_i^3} - \frac{1}{4\pi\rho}\sum_{k\neq i}^{N_b}\frac{G_iG_k}{R_iR_kr_{ik}} + \frac{1}{4\pi\rho}\sum_{k\neq i}^{N_b}\sum_{j\neq k}^{N_b}\frac{R_kG_iG_k}{R_iR_jr_{ik}r_{kj}} + \cdots\right] & (A.46)\\ \sim& \frac{N_bG^2}{8\pi\rho R^3}\left[1 - \left(\frac{N_bR_0}{R_c}\right) + \left(\frac{N_bR_0}{R_c}\right)^2 + \cdots\right] & (A.47)\\ =& \frac{N_bG^2}{8\pi\rho R^3}\left[1 + \sum_{n=1}^{N_b}(-B)^n\right]. & (A.48)\end{aligned}$$

The scaling shows that the kinetic energy due to inter-bubble interactions, and thus the Hamiltonian, are parametrized by a polynomial about B, and that the expression is convergent if and only if $B < O(1)$. This explains the physical meaning of diagonal dominance of $\boldsymbol{A}$. When $B < O(1)$, $\sum_{n=1}(-B)^n < O(1)$ and the contribution of inter-bubble interactions to the total kinetic energy is smaller than that of self-action, and when $B > 1$ the relation is opposite. Thus the expressions for $\mathcal{K}$ and the Hamiltonian are valid for a cloud with relatively small contributions of inter-bubble interactions.

A.4 Summary

We reviewed and analyzed the dynamical equation for the volumetric oscillations of spherical bubbles under mutual interactions. The equation is a non-autonomous, implicit system of ODEs. The complexity of the direct solution method is $O(N_b^3)$ due to matrix inversion required to transform the system into an explicit form. If the matrix to be inverted is diagonally dominant, the Jacobi method can be used to reduce the complexity to $O(N_b^2)$. The transformation of the equation into the Hamiltonian system in the form proposed by Ilinskii et al. (2007) is equivalent to the preconditioning, while the transformation itself is not necessary for reduction of the complexity.

For a spherical bubble cluster, the condition for the diagonally dominance of the matrix is $B_0 < 1$. Therefore, the preconditioning is limited to a bubble cloud with a small size and/or with a relatively small number of bubbles. If a cloud is dense and/or large o satisfy $B_0 > 1$, the matrix can become non-diagonally dominant and preconditioning may fail. A family of algebraic multi-grid methods has presented good performances for preconditioning certain linear systems with a dense, non-diagonally dominant matrix (Chang et al., 1996), and could be applied to cases with $B_0 > 1$.